Laser assisted development of Graphene and Transition Metal Dichalcogenide nanomaterials

Kyriaki Savva

Supervisors: Dr. Emmanuel Stratakis

Prof. Costas Fotakis

Department of Physics

University of Crete

July 2018

This work was supported by the State Scholarship Foundation (IKY) within the framework of action “Doctoral research support” (5003404), ESPA 2014-2020 Program 2017-050-0504-10150

“Try not to become a man of success,

but rather try to become a man of value”

Albert Einstein

…dedicated to my lovely family…

Table of Contents

The present dissertation has been written under the direction of **Dr. Emmanuel Stratakis and Prof. Costas Fotakis** and has been approved by:

1. Emmanuel Stratakis, Principal Researcher, IESL/FORTH
2. Alexandros Georgakilas, Professor, Physics Department, University of Crete
3. Dimitrios Charalampidis, Professor, Physics Department, University of Crete
4. Zacharias Hatzopoulos, Associate Professor, Physics Department, University of Crete
5. Nikos Pelekanos, Professor, Materials Science and Technology Department, University of Crete
6. Georgios Kioseoglou, Associate Professor, Materials Science and Technology Department, University of Crete
7. Emmanuel Kymakis, Associate Professor, Electrical engineering Department, T.E.I. of Crete

Acknowledgements

I would like to express my sincere gratitude and deep devotion to my advisor Dr. Emmanuel Stratakis for the continuous support, his patience and constant encouragement of my PhD research. I appreciate all of his guidance and valuable assistance making my PhD program motivated and productive. I strongly believe that the most defining parameter to achieve a successful PhD is the relationship with the advisor and therefore I feel myself very lucky to cooperate with him. I appreciate not only his scientific knowledge but him as a person since he was very supportive and helpful through all these years in hard times.

My most sincere regards goes to my advisor Prof. Costas Fotakis for giving me access to the laboratory and research facilities. His support was very helpful for concluding this research.

Besides my advisors I would like to thank the members of the committee of my thesis, Prof. Alexandros Georgakilas, Prof. Dimitris Charalampidis, Prof. Emmanuel Kymakis, Prof. George Kioseoglou, Prof. Nikos Pelekanos and Prof. Zacharias Hatzopoulos, for doing me the honor of evaluating my PhD thesis.

I would also like to thank the members of NANO group in TEI of Crete for the excellent cooperation we had these years. Special thanks to Asst. Prof. Costas Petridis for all the help and guidance in conducting part of the experiments of this work.

I would also like to express my appreciation and thanks to our collaborators Prof. Reshef Tenne and Dr. Bojana Višić in Weizmann Institute and Prof. Thomas Anthopoulos in Imperial College.

I thank my fellow mates, all the members of the ULMNP group and my colleagues in the office for all the support, the fun we have had during the last years and for creating a pleasant environment to work in. Special thanks to my very good friend Maria Sygletou for all the help, guidance and useful comments along the writing of this thesis and Antonia Loufardaki providing help every time I needed it.

Much of this work would not have been possible without the help of numerous people. At this point, I would like to make a special mention of Aleka Manousaki, Athanasia Kostopoulou, George Kenanakis, Maria Fouskaki, Lamprini Sugelou, Yiannis Labrakis and Apostolis Eglezis.

Last but sure not least, I owe my deepest gratitude to my lovely family for their emotional and financial support. Words cannot express how grateful I am to my parents for all the sacrifices they made on my behalf and for being supportive through hard times and encouraging me to never give up and always face the difficulties with a smile.

Abstract

Two-dimensional materials with an atomic scale thickness, including graphene and other related materials, have attracted considerable research interest due to their excellent physical properties. In this thesis we introduce new laser-based methods for the synthesis of 1D and 2D nanomaterials based on graphene and transition metal dichalcogenides (TMDs).

In particular we demonstrate the laser induced photochemical modification of graphene oxide (GO) for organic photovoltaic (OPV) devices and electronic applications. We report on a rapid and facile method, for the laser-based reduction, doping and patterning of GO. The photochemical method we developed for the simultaneous reduction and doping of GO layers is based on ultraviolet laser irradiation in the presence of a dopant precursor gases, including Cl_2 and NH_3. It is shown that a few seconds of irradiation is sufficient to dope the GO lattice, while the doping and reduction levels can be readily controlled upon variation of the irradiation time. This method was successfully employed for the in situ laser induced modification of prefabricated GO field effect transistors. Furthermore, this fast, non-destructive and roll-to-roll compatible photochemical method can be use for the reduction and doping of GO nanosheets as well. By tuning the laser exposure time, it is possible to control the doping and reduction levels and therefore to tailor the work function (WF) of the GO-Cl nanosheets to a maximum value of 5.23 eV, which is a value that matches the HOMO level of most polymer donors employed in OPV devices. Furthermore, a laser-based patterning technique—compatible with flexible, temperature sensitive substrates—for the production of large area reduced graphene oxide micromesh (rGOMM) electrodes is presented. The mesh patterning can be accurately controlled in order to significantly enhance the electrode transparency, with a subsequent slight increase in the sheet resistance, and therefore improve the tradeoff between transparency and conductivity of reduced graphene oxide (rGO) layers. As a proof-of-concept application, rGOMMs are used as the transparent electrodes in flexible organic photovoltaic (OPV) devices, achieving power conversion efficiency of 3.05%, the highest ever reported for flexible OPV devices incorporating solution-processed graphene based electrodes.

The study of inorganic nanometer-scale materials with hollow closed-cage structures, such as inorganic fullerene-like nanostructures (IF) and nanotubes (INT), is a rapidly growing field. To date, numerous kinds of IF and INTs TMDs were synthesized for various applications, particularly for lubrication. In this thesis we demonstrate new simple, room temperature and environmentally friendly approaches for the synthesis of IF and INTs via a) ultrashort pulse laser ablation of TMDs in bulk form in ambient air as well as b) via pulsed laser deposition (PLD) of bulk TMD targets. These techniques can be further developed for the formation of nanostructures at any preselected location, such as microsized asperities, which are destined to

numerous applications, including for electron emission cathodes and scanning probe microscopy field emitters.

Περίληψη

Τα δισδιάστατα υλικά με πάχος ατομικής κλίμακας συμπεριλαμβανομένου του γραφενίου, έχουν προσελκύσει σημαντικό ερευνητικό ενδιαφέρον λόγω των εξαίρετων φυσικών τους ιδιοτήτων. Σε αυτή τη διατριβή εισάγουμε νέες μεθόδους με βάση το λέιζερ για τη σύνθεση 1D και 2D νανοϋλικών βασισμένων σε γραφένιο και διχαλκογενή μέταλλα μετάπτωσης.

Πιο συγκεκριμένα, παρουσιάζουμε τη φωτοχημική τροποποίηση του οξειδίου του γραφενίου με χρήση λέιζερ για οργανικές φωτοβολταϊκές διατάξεις και ηλεκτρονικές εφαρμογές. Γίνεται αναφορά σε μια απλή και γρήγορη μέθοδο με χρήση λέιζερ για την αναγωγή, τον εμπλουτισμό και την τροποποίηση του οξειδίου του γραφενίου. Η φωτοχημική μέθοδος που αναπτύξαμε για την ταυτόχρονη αναγωγή και τον εμπλουτισμό του οξειδίου του γραφενίου βασίζεται στην υπεριώδη ακτινοβολία λέιζερ παρουσία πρόδρομων αερίων όπως το χλώριο (Cl_2) και την αμμωνία (NH_3).

Αποδεικνύεται ότι μερικά δευτερόλεπτα ακτινοβολίας είναι αρκετά για τον εμπλουτισμό του πλέγματος του οξειδίου του γραφενίου, καθώς τα επίπεδα εμπλουτισμού και αναγωγής μπορούν εύκολα να ελεγχθούν με τη μεταβολή του χρόνου έκθεσης ακτινοβολίας. Η μέθοδος αυτή χρησιμοποιήθηκε με επιτυχία για την τοπική τροποποίηση τρανζίστορ οξειδίου του γραφενίου με χρήση λέιζερ. Επιπλέον η γρήγορη αυτή μέθοδος μπορεί να χρησιμοποιηθεί για την αναγωγή και τον εμπλουτισμό νανοφύλλων οξειδίου του γραφενίου. Ρυθμίζοντας το χρόνο έκθεσης στην ακτινοβολία λέιζερ, μπορούμε να ελέγξουμε τα επίπεδα εμπλουτισμού και αναγωγής και επομένως να προσαρμόσουμε το έργο εξόδου (WF) των νανοφύλλων GO-Cl σε μέγιστη τιμή 5,23 eV, η οποία ταιριάζει με το επίπεδο HOMO των περισσότερων δοτών πολυμερών που χρησιμοποιούνται σε οργανικές φωτοβολταϊκές διατάξεις. Επιπλέον παρουσιάζεται μια τεχνική σχεδίασης με λέιζερ συμβατή με εύκαμπτα και ευαίσθητα στη θερμοκρασία υποστρώματα για την παραγωγή μεγάλης επιφάνειας ανηγμένου οξειδίου του γραφενίου μικροπλέγματος ηλεκτροδίων. Το σχέδιο του πλέγματος ελέγχεται με ακρίβεια προκειμένου να ενισχυθεί σημαντικά η διαπερατότητα του ηλεκτροδίου με μικρή αύξηση της αντίστασης και επομένως να βελτιωθεί η συχσέτιση διαπερατότητας και αγωγιμότητας των στρωμάτων ανηγμένου οξειδίου γραφενίου. Το ανηγμένο οξείδου του γραφενίου μικροπλέγμα χρησιμοποιείται ως διαπερατό αγώγιμο ηλεκτρόδιο σε εύκαμπτες φωτοβολταϊκές διατάξεις επιτυγχάνοντας απόδοση 3,05%, την υψηλότερη τιμή που αναφέρθηκε για οργανικά φωτοβολταϊκά ενσωματωμένα με ηλεκτρόδια με βάση το γραφένιο.

Η μελέτη των ανόργανων νανοδομών φουλερενίων (IF) και ανόργανων νανοσωλήνων (INTs) έχει γνωρίσει ιδιαίτερη προσοχή στην παγκόσμια επιστημονική έρευνα. Πραγματοποιήθηκε σύνθεση πολυάριθμων IF και INTs για ποικίλες εφαρμογές ιδιαίτερα ως λιπαντικά. Στόχος της παρούσας διατριβής η διερεύνηση και

η ανάπτυξη νέων οδών φιλικών προς το περιβάλλον για τη σύνθεση δομών IF και INTs. Για το σκοπό αυτό παρουσιάζουμε απλές τεχνικές με χρήση λέιζερ. Συγκεκριμένα, η έκθεση μίγματος διχαλκογενών μετάλλων μετάπτωσης (TMDs) και Pb σε έντονη ακτινοβολία λέιζερ καθώς και η αποδόμηση υλικού από στόχους MX2 με την τεχνική εναπόθεσης παλμικού λέιζερ (PLD). Θεωρείται μια φωτοθερμική και φωτοχημική μέθοδος όπου οι υψηλές θερμοκρασίες και η αλληλεπίδραση του λέιζερ με το στόχο οδηγούν στη σύνθεση διαφορετικών νανοδομών. Βάση των δυνατοτήτων της τεχνολογίας των λέιζερ οι τεχνικές αυτές μπορούν να αναπτυχθούν περαιτέρω για την ανάπτυξη και διαμόρφωση νανοδομών σε επιλεγμένες επιφάνειες όπως για παράδειγμα οι «λοφώδεις» μικροδομές πυριτίου (spikes) για ποικιλία εφαρμογών.

Introduction

The "dimensionality" is one of the most crucial material parameters: the same chemical element can exhibit different properties depending on whether it exhibits a 0D, 1D, 2D or 3D crystal structure[1]. For example, carbon, forms allotropes of any possible dimensionality ranging from 3D diamond, where carbon atoms are bonded in a tetrahedral lattice arrangement, and graphite, where carbon atoms are bonded in hexagonal lattice sheets, to 2D graphene, 1D nanotube (single-walled carbon nanotubes - SWCNT, multi-walled carbon nanotubes - MWCNT) and 0D fullerenes where carbon atoms are bonded in spherical, tubular, or ellipsoidal formations[2] (Figure 1).

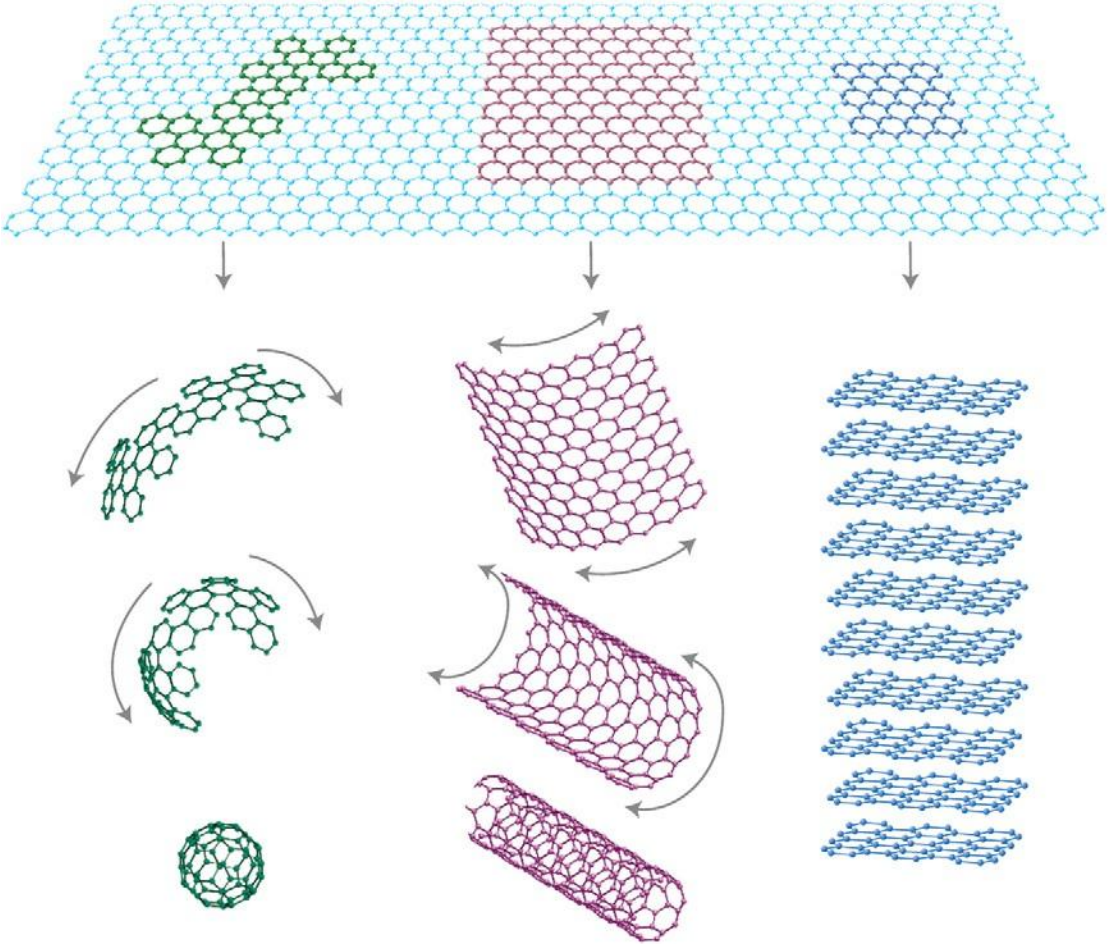

Figure 1. Mother of all graphitic forms. Graphene is a 2D building block for carbon materials of all other dimensionalities. It can be wrapped up into 0D buckyballs, rolled into 1D nanotubes or stacked into 3D graphite[3]

Layered compounds, like graphite or MoS_2, are characterized by their anisotropic bonding properties. In particular, the atoms within the layer (ab plane) are covalently bonded like, for instance, the sp^2-bonded carbon atoms in the honeycomb lattice of graphite. These molecular slabs are stacked together by weak van der Waals forces along the c axis (Figure 2). While the carbon atoms within each sheet (graphene layer) are fully coordinated and hence are unreactive, the atoms at the periphery of the layer are only di-coordinated, and are consequently very reactive. Therefore, the surface energy of graphene layers, no larger than a few nanometers in diameter is exceedingly high, which makes the sheet unstable with respect to folding and forces it to close onto itself. For that to happen along two axes in the ab plane, 12 pentagons are disposed in the hexagonal network and carbon fullerenes are obtained. If the folding of the graphene layer occurs along one axis only, nanotubes are formed. The folding process induces elastic strain, which requires the surmounting of an activation energy barrier. Therefore heating the reactor, or using other energy sources, such as various kinds of irradiation, is necessary to initialize the folding process. Once the fullerene-like nanoparticle is realized and the dangling bonds are healed, the seamless structure becomes (meta)stable[4].

The driving force for the formation of carbon fullerenes and nanotubes stems from the abundant reactive atoms on the periphery of the quasi two-dimensional planar nanostructures. The planar topology of graphene nanoparticles of a few nanometers in size is unstable with respect to the hollow and seamless fullerenes and nanotubes. These facts suggested that the formation of hollow closed structures is a general property of nanoparticles of two-dimensional (layered) compounds.

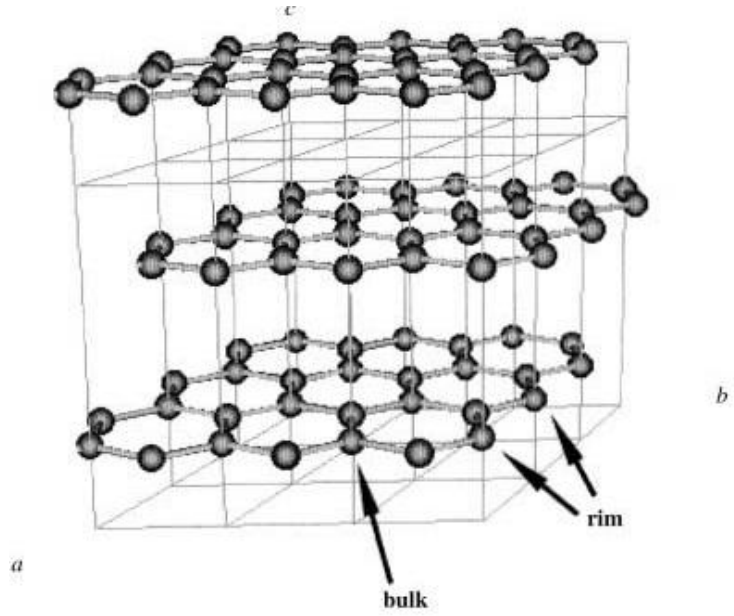

Figure 2: A schematic drawing of graphite. The surface energy, which destabilizes the planar topology of the nanocluster, is concentrated in the di-coordinated carbon atoms on the rim of the lamella[4].

The two-dimensional materials with an atomic scale thickness, such as for example graphene, have attracted considerable research interest due to their excellent physical properties. Graphene is a single two-dimensional layer of carbon atoms (Figure 3) that are bounded in a hexagonal lattice structure. Although it was isolated for the first time in 2004[3] at Manchester University, several studies have been performed, with Andre Geim and Konstantin Novoselov winning the 2010 Nobel Prize in Physics for their excellent work on graphene. Graphene quickly gained great interest because of the extraordinary properties it seems to possess as a zero-gap semiconductor material[5], and it could have particularly interesting applications in electronic devices[6,7,8,9]. In order to harness these properties for applications, one possible route would be to incorporate graphene sheets in a composite material[10]. The research has tended to focus on chemically modified graphene due to its excellent electrical, mechanical and thermal properties, thus it has been studied in the context of many applications such as polymer composites, energy-related materials, sensors, field-effect transistors (FET) and biomedical devices. A promising route to achieve mass production of chemically modified graphene platelets is the chemical modification of graphene oxide (which is generated from graphite oxide). Graphene oxide is a good candidate for use in the applications mentioned above through chemical functionalizations because it contains a range of reactive oxygen functional

groups[11] . Furthermore, graphite oxide is said to be a precursor that offers the potential of cost-effective and large-scale production of graphene-based materials[12]. These studies have emphasized in graphene oxide-based thin-film electronics and optoelectronics, a route offered by the solubility of graphene oxide in a variety of solvents[13]. The efforts to obtain graphene-based derivatives through the reduction of graphene oxide in solution have become a favorite topic of analysis from many researchers in order to create transistors and electrodes for organic photovoltaics[14,15].

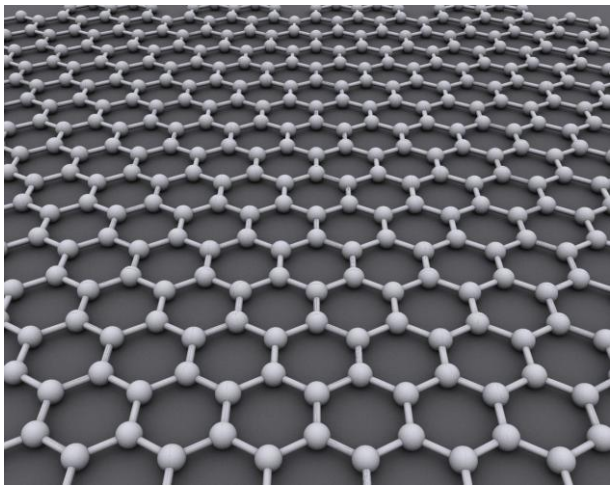

Figure 3: A schematic drawing of graphene

With the discovery of graphene, the interest in other two-dimensional layered materials became renewed. Transition metal dichalchogenides have been one of the most studied families of materials, since they can range from being metallic to semiconducting or insulating in nature. They are perfect candidates for thinning into monolayer flakes due to their weak interlayer bonding. Besides this, their ability to form structures of different dimensionalities opens up a broad range of potential applications and research possibilities. Their band-gap transformation from indirect to direct, as their thickness decreases to single layer, opening up dramatic enhancement of photoluminescence quantum yield. This offers opportunities for fundamental and technological research in a variety of fields including catalysis, energy storage, sensing and electronic devices such as field-effect transistors and logic circuits[16]. Furthermore, it has been shown that they are unstable against folding, forming nanotubes and fullerene-like nanoparticles. While nanotubes and nanoparticles of these materials have already been implemented in industry, mainly as lubricants, the

various potential applications of their 2D counterparts are still under investigation.

Transition metal dichalcogenides (TMDs) with the form MX_2 (M=Mo, W, Ti, etc., and X=S, Se, Te) exhibit a structure very similar to that of graphite[17]. In analogy to graphite, nanoparticles of inorganic compounds with lamellar two-dimensional structure, such as MoS_2, are not stable against folding, and can adopt nanotubular and fullerene-like structures, nicknamed inorganic nanotubes INTs and inorganic fullerenes, IFs, respectively. Various applications for such nanomaterials were proposed, for instance, IF-MoS_2 nanoparticles (Figure 4) and WS_2 INTs (Figure 5) were shown to have beneficial effects as solid lubricants and as part of tribological surfaces. Further applications for high-tensile- strength fibers, hydrogen storage, rechargeable batteries, catalysis and in nanotechnology are being contemplated[4].

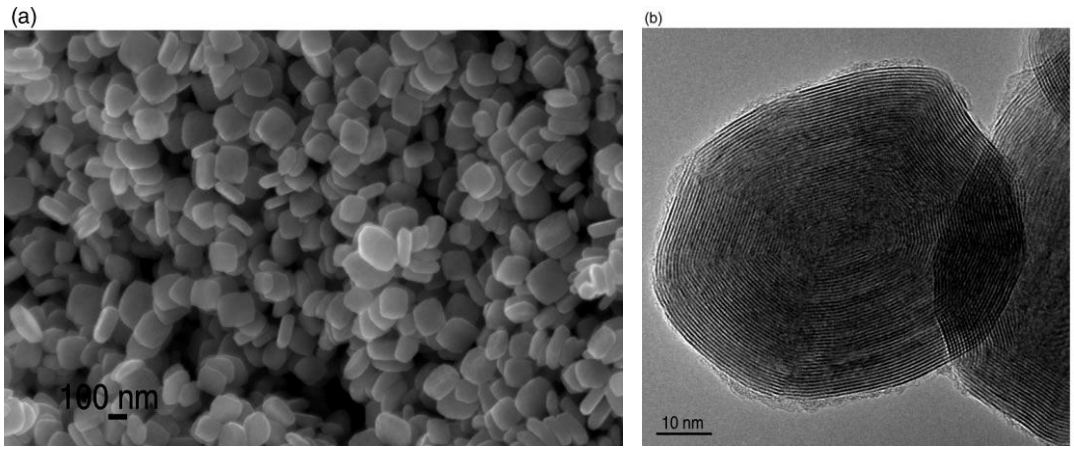

Figure 4: (a) SEM and (b) TEM images of IF-MoS_2 nanoparticle[18]

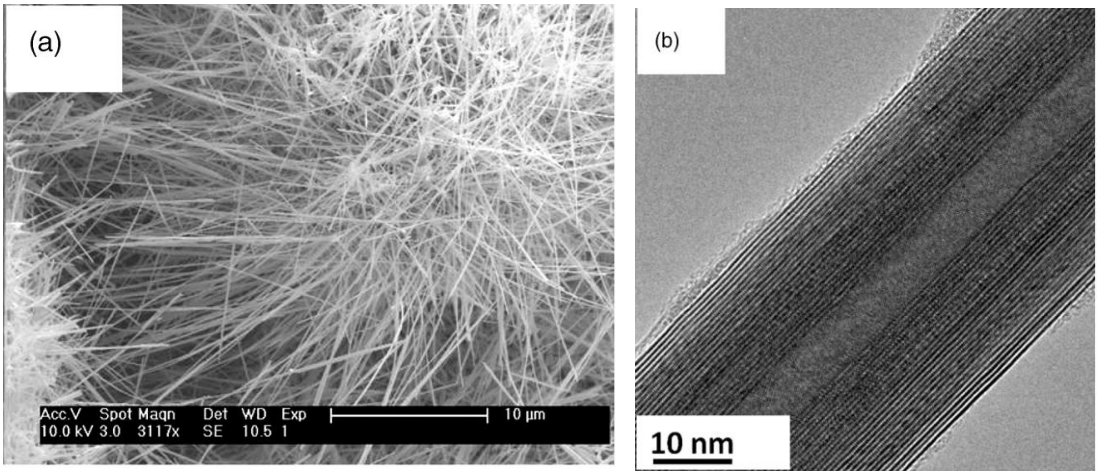

Figure 5: (a) SEM and (b) TEM images of WS_2 nanotubes[19].

Chapter I: Synthesis and properties of two-dimensional nanomaterials and related structures

1.1. Graphene-based 2D nanomaterials

Since graphene was isolated in 2004 by Geim and Novoselov using the most commonly known method of scotch tape, several processes were developed to produce one or few graphene layers. One of the main concerns in graphene composition is the production of samples with high carrier mobility and low defect density.

1.1.1. Graphene's properties

The remarkable properties of graphene are among others:

- large theoretical specific surface area (2630 m^2g^{-1})
- high intrinsic mobility (200 000 $cm^2 v^{-1} s^{-1}$)
- high Young's modulus (~ 1.0 TPa)
- thermal conductivity (~ 5000 $Wm^{-1} K^{-1}$)
- optical transmittance (~ 97.7%) and
- good electrical conductivity, which merits attention for applications such as for transparent conductive electrodes[12].

Optical properties: It has been theoretically calculated and experimentally verified that graphene can absorb ~2.3% of white light and reflects <0.1% of the incident. In addition, the optical absorption of graphene layers is linearly proportional to the number of layers. The absorption of monolayer graphene exhibits a flat behavior over a long range, presenting a peak in the UV region (~250 nm), owing to π-π* transition[20].

Mechanical properties: Carbon allotropes have their own record in terms of mechanical strength, hardness, or Young's modulus. Graphene is no exception, considered as one of the strongest materials ever tested, owing to the 0.142 nm-long carbon bonds strength. It exhibits a tensile strength of 130 GPa, which it is

approximately 100 times stronger than steel, while a Young's modulus of 0.5 TPa has been verified by Atomic Force Microscopy (AFM)[21]. Finally, despite of its strength, graphene is very light, since 0.77 mg per square meter is 1000 times lighter than a square meter of paper, with one gram of graphene being large enough to cover a football field[22].

Thermal properties: Apart from its excellent optoelectronic and mechanical properties, graphene is a unique thermal conductor. Its thermal conductivity exceeds 5000 $Wm^{-1}K^{-1}$, significantly higher compared to other carbon structures and even graphite (1000 $Wm^{-1}K^{-1}$)[23].

Electronic properties: The electronic structure of graphene evolves very quickly with the number of layers. We can distinguish single, double and few (3 to <10) layer graphene as three different types of 2D crystals. Only graphene and its bilayer have simple electronic spectra, since they both are zero gap semiconductors with one type of electrons and one type of holes. In the case of 3 and more layers there is the appearance of several charge carriers while the conductive and valence bands start overlapping[3]. Graphene's crystal structure is the reason for its remarkable band structure and the interest it gained from scientists. According to Wallace who calculated the band structure for a single graphite layer in 1947[24], the hexagonal lattice of graphene can be regarded as two interleaving triangular lattices, with two carbon atoms per unit cell. The s, p_x, and p_y atomic orbitals on each carbon hybridize to form strong covalent sp^2 bonds, giving rise to 120 ° C-C-C bond angles. The remaining p_z orbital on each carbon overlaps with its three neighboring carbons to form a band of filled π orbitals (valence band) and a band of empty π^* orbitals (conduction band). Each carbon atom is about a=1,42 A^o from its three neighbors with each of which it shares one σ bond. The fourth bond is a π bond which is oriented in the z direction[5,25]. The conduction and the valence band touch at six points, the Dirac points. These points can reduce to a pair of K and K′ due to symmetry but each set is not equivalent with the other set of three. In low energies, the bands have a linear dispersion and the bandstucture can be viewed as two cones touching at $E_{DIRAC.}$ Their crossing is allowed because π and π^* states do not interact. Graphene has zero band gap, due to the fact that these bands touch at E_{DIRAC} [26].

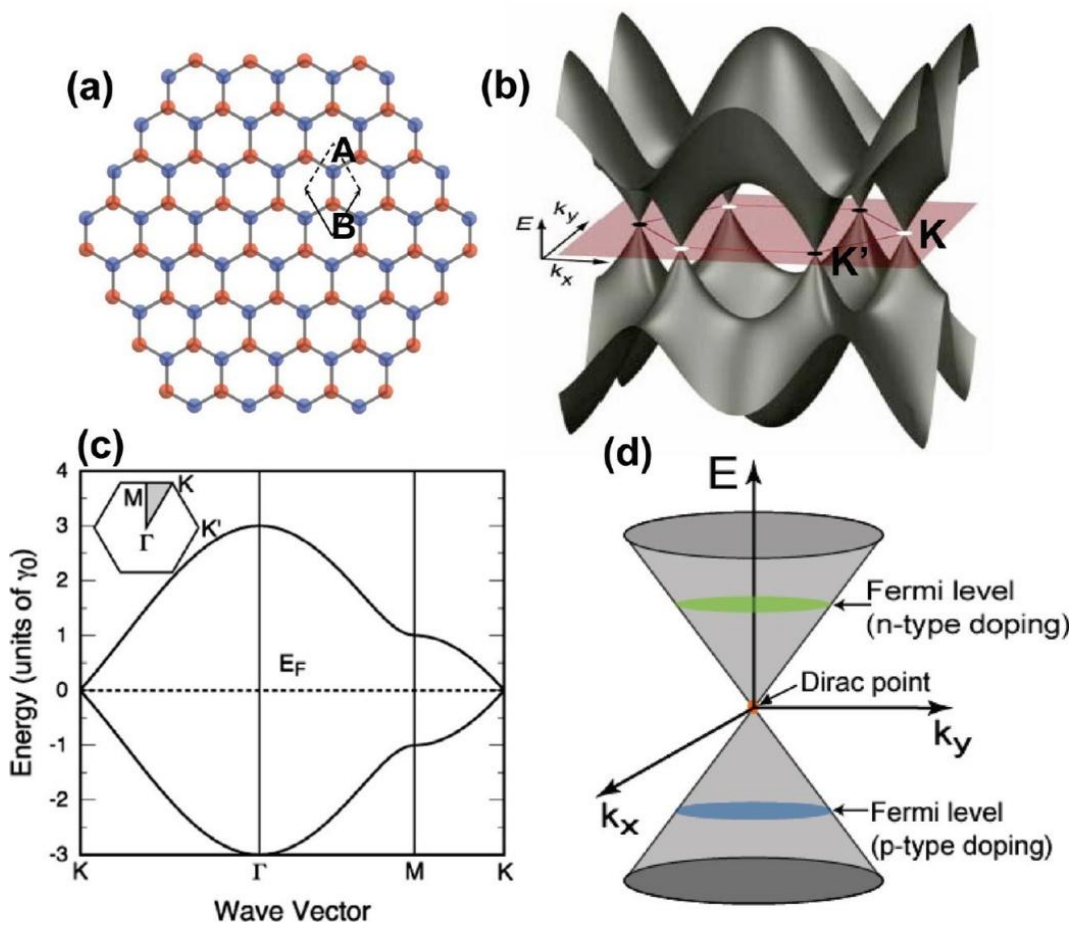

Figure 1.1: (a) Hexagonal honenycomb lattice of graphene with two atoms (A and B) per unit cell. (b) The 3D bandstructure of graphene. (c) Dispersion of the states of graphene. (d) Approximation of the low energy band-structure as two cones touching at the Dirac point. The position of the Fermi level determines the nature of the doping and the transport carrier[26].

1.1.2. Synthetic methods of graphene

The main graphene synthesis methods are mechanical exfoliation, thermal decomposition of SiC, chemical vapor deposition (CVD), exfoliation of graphite in solvents, as well as, laser ablation and photoexfoliation.

Mechanical exfoliation process uses highly oriented pyrolitic graphite as a precursor and is developed by Geim and Novoselov[3]. Using this technique Geim and Novoselov were able to generate few- and single-layer graphene flakes with dimensions of up to 10 μm. This method can be used to generate 'high quality' graphene that is

electrically isolated for fundamental studies of transport physics and other properties. However it does not yet appear to be scalable to large area.

Thermal decomposition of SiC is a technique consisting of heating SiC in ultra high-vacuum at temperatures between 1000-1500 ° C. This causes Silicon to sublimate from the material leaving behind a carbon-rich surface. Low-energy electron microscopy studies (LEEM) indicate that this carbon layer is graphitic in nature and suggest that this technique could be used to form graphene[27].

In contrast to the thermal decomposition of SiC, where carbon is already present in the substrate, in ***chemical vapor deposition (CVD)***, carbon is supplied in a gas phase in the form of a chemical compound (e.g., methane) and a metal is used as both catalyst and substrate to grow the graphene layer. The metals commonly used are nickel (Ni) and copper (Cu)[5].

Exfoliation of graphite in solvents is considered as one of the most feasible approaches for industrial production of graphene owing to its scalability and low cost. This technique inspired by obtaining dispersions of graphite oxide to yield individual layers of graphene oxide (i.e., colloidal dispersions), is to make dispersions of graphite in various solvents. This is typically done by exposure of graphite or graphite oxide powders in organic solvents such as DMF or NMP to high intensity ultrasound and includes three steps: graphite dispersion in a solvent, exfoliation and purification[28].

These last years, ***laser ablation and photoexfoliation*** is a field that rises rapidly with promising results. Ultrashort laser pulses are used to detach intact graphene monolayers from a graphite surface indicating that photoexfoliation should be capable of producing graphene monolayers free of contaminants and defects at a high rate[29]. Laser-induced surface decomposition of the Si-rich face of a SiC single-crystal, confirms the formation of epitaxial graphene on SiC as a result of excimer laser irradiation. Laser pulses can be used to ablate graphite flakes where the ablation of a defined number of layers can be obtained exploiting the laser energy density window required for ablating a single layer graphene or few layer graphene[30,31].

1.1.3. An overview of graphene oxide

Graphite oxide was discovered years before graphene. Prof. B.C. Brodie was the first that explored the structure of graphite by investigating the reactivity of flake graphite. The preparation method was based on heating a mixture of graphite and fuming HNO_3 in the presence of $KClO_3$ at 60 ^oC for 3-4 days. After washing the product, the oxidation process was repeated four times, to finally produce a light yellow solid after drying at 100 ^oC. The product C:H:O was calculated to be 61.04:1.85:37.11 and since it was dispersed in pure or alkaline water, and not in acidic media, Brodie named the material ‘‘graphitic acid”[32]. Nearly forty years after Brodie's discovery of the oxidation of graphite, L. Staudenmaier improved the composition of Brodie by adding sulfuric acid H_2SO_4 to increase the acidity of the mixture. This slight change in process resulted to a total oxidation extension similar to Brodie's multiple oxidation approach (C: O ~ 2: 1), but performed more practically in a single reaction vessel. Nearly sixty years after Staudenmaier, Hummers and Offerman developed an alternative method of oxidation by reacting graphite with a mixture of $KMnO_4$ instead of $KClO_3$ and sulfuric acid H_2SO_4[33]. This combination resulted in a more oxidized form of graphite oxide and that is why Hummers method has been used widely from many researchers. An improved synthesis of graphene oxide was presented in 2010 by Marcano et al[34], where they exclude the $NaNO_3$, increased the amount of $KMnO_4$ and performed the reaction in a 9:1 mixture of H_2SO_4/H_3PO_4. These conditions improved the efficiency of the oxidation process and the avoidance of large toxic gases production makes it suitable for large scale production of graphite oxide.

Graphene oxide contains typically carboxyl, hydroxyl or epoxy groups bonded on graphene and other atomic-scale lattice defects, which offers rich opportunities for chemical modification. Although there have been proposed a number of graphene oxide synthesis methods the last decades, its exact chemical structure is still under investigation. The earliest model by Hofmann and Holst in 1939[35] proposed the dominance of epoxides on the basal plane, while Ruess[36] subsequently included hydroxyl groups. Later, Scholz and Boehm[37] showed the presence of ketones and hydroxyls but excluded epoxides. In 1994, the Nakajima-Matsuo model[38] suggested a lattice structure interspersed with hydroxyl groups. The most well-known and

accepted model is the one of Lerf-Klinowski[39] and with the use of solid state nuclear magnetic resonance (NMR) spectroscopy they identify two distinct basal plane regions consisting of pristine aromatic regions separated by aliphatic 6-membered rings containing hydroxyls, epoxyls (1,2-ethers) and C=C double bonds with carboxylic groups in low quantities at the edge sites. Following this, Dekany[40] depicted a graphite oxide structure with the presence of quinone groups in addition to tertiary alcohols, 1,3-ethers, ketones, and phenols. The summary of these models is presented in Figure 1.2. In 2009, Ajayan et al.[41] detected the presence of lactols at peripheral edges, specifically 2-hydroxynaphthalic anhydrides or 1,3-dihydroxyxanthones (Figure 1.3).

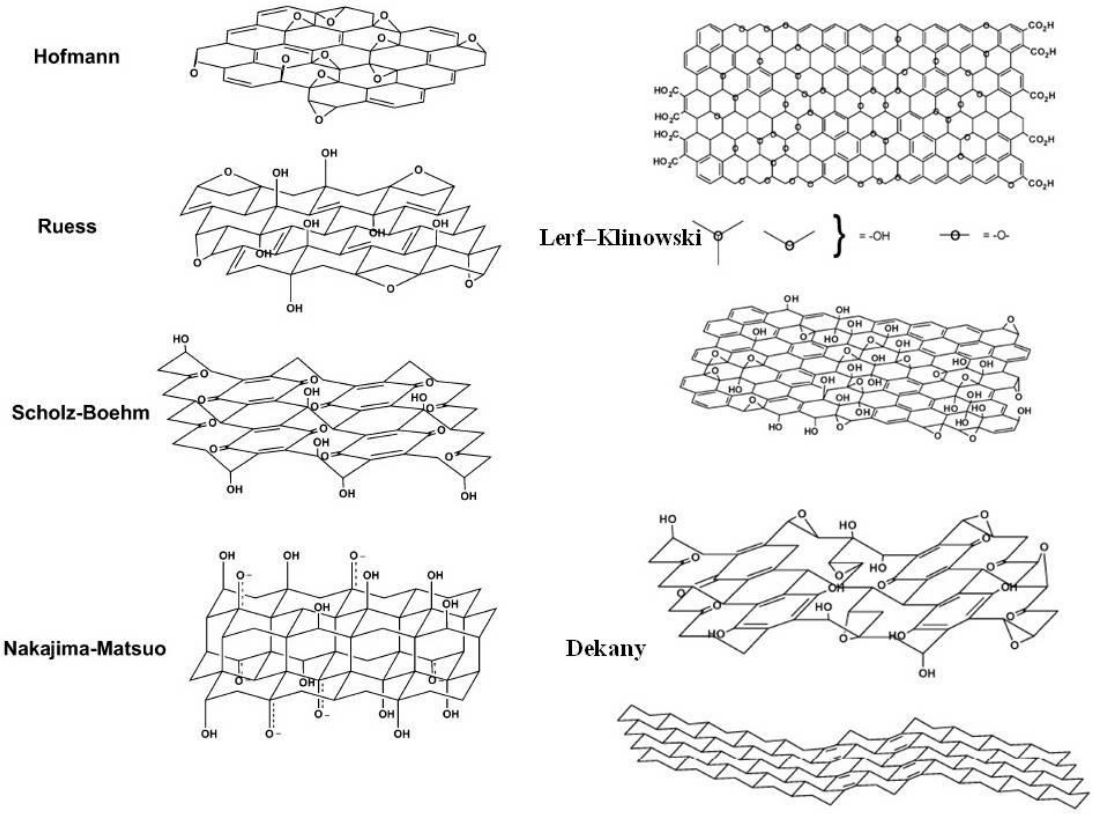

Figure 1.2: Summary of several older structural models of GO[11].

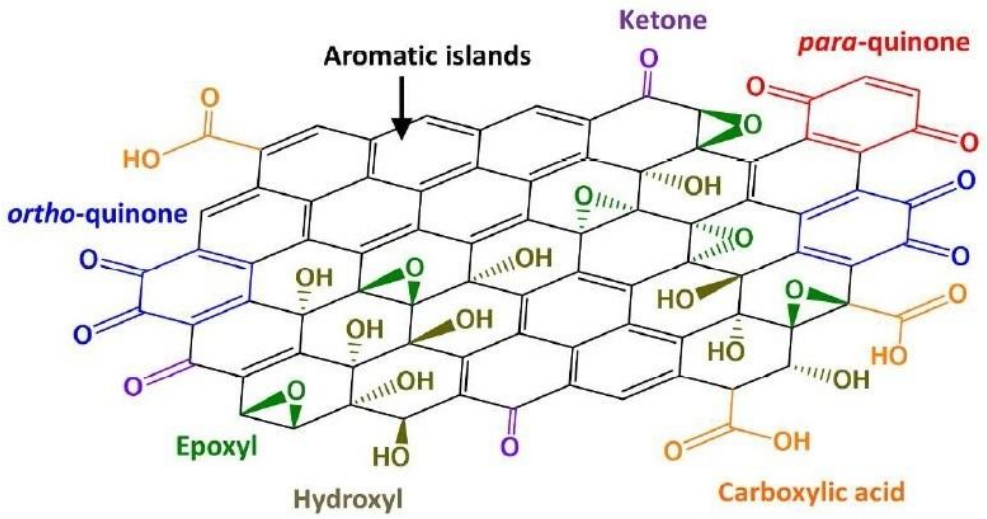

Figure 1.3: General model of graphite oxide demonstrating various oxygen functional group types distributed across aromatic regions[42]

Graphite oxide and graphene oxide are electrically insulating materials due to their disrupted sp^2 bonding networks. One of the most important graphene oxide reactions is its reduction where electrical conductivity can be recovered by restoring the π-network. The product of this reaction is reduced graphene oxide[11]. The polar O and OH groups formed during the oxidation process make the graphene oxide hydrophilic and it can be chemically exfoliated in several solvents, including water. The oxygen groups can then be removed in a reduction process involving one of several reducing agents[5].

1.1.4. Reduction of Graphene Oxide

As we mentioned above, the reduction process is one of the most important reactions of graphene oxide due to the similarities between rGO and the pristine graphene. In order to use graphene in large-scale applications such as energy storage, chemical conversion of graphene oxide is the most obvious and desirable route in large quantities of graphene-like materials. Different methods have been proposed for the reduction of graphene oxide to reduced graphene oxide (Figure 1.4) through

chemical, thermal and photochemical pathways. All of these approaches lead to products that resemble pristine graphene to many aspects, especially in electrical, thermal and mechanical properties[11].

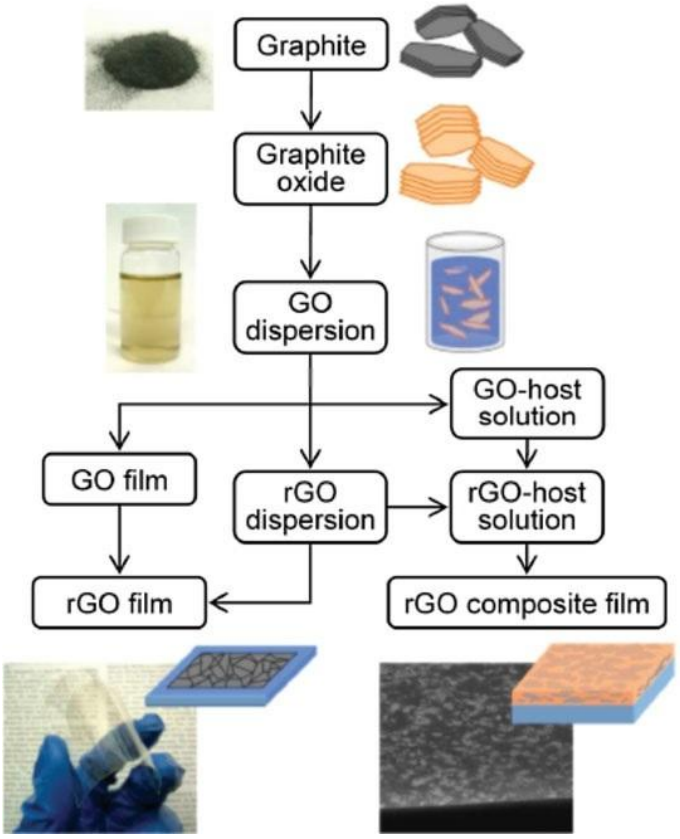

Figure 1.4: Process scheme for fabricating rGO-based thin films. The schematic illustrations show the structure of the material at each stage of the process. The gray and the orange sheets represent not oxidized and oxidized graphene sheets, respectively[13].

Chemical reduction: In recent years, numerous methods are proposed for the chemical reduction of graphene oxide. However, the more common and one of the first to be reported by Brauer in 1963[43], was that using hydrazine monohydrate as the reduction agent. Hydrazine monohydrate does not show reactivity with water like most of reductants, which makes it an attractive option for reducing aqueous dispersions of graphene oxide. The main concerns of the graphene community are a) to achieve the highest degree of reduction, b) to heal the defective graphene oxide, c) to selective remove a single type of oxygen moiety, d) to improve the dispersion stability of the resulting graphene and e) to apply environmental friendly and low-cost

reducing agents[44]. One of the disadvantages of using chemical reduction methods is the introduction of heteroatomic impurities.

Thermal reduction: In this case instead of using a chemical reductant to strip the oxide functionality from the surface, it is possible to create thermodynamically stable carbon oxide species through direct heating of graphene oxide in a furnace. The rapid heating up to 1050 ^{o}C, was used to exfoliate graphite oxide to graphene. Exfoliation takes place when the decomposition rate of the epoxy and hydroxyl sites of graphite oxide exceeds the diffusion rate of the evolved gases, thus yielding pressures that exceed the Van der Waals forces bonding the graphene sheets together[45]. A notable effect of this process is the structural damage caused to the platelets by the release of carbon dioxide.

Photochemical reduction: Recently there has been growing interest in the reduction of graphene oxide by photochemical methods such as pulsed laser, induced ultraviolet radiation[46] and flash from a xenon lamp[47]. In the case of the pulsed laser, there have been demonstrated reduction of graphene oxide in solution either with Nd/YAG laser (λ=532 nm, 7 ns)[48] or KrF excimer laser (λ=248 nm, 20 ns)[49] and reduction of graphene oxide films either with femtosecond laser (λ=790nm, 120 fs)[50] or KrF excimer laser (λ=248 nm, 10ns)[51]. The main advantage of the pulsed laser technique is that it is fast (only last a few minutes) and does not require the use of hazardous precursor materials and high temperatures. This can be verified by the dramatic color change of the graphene oxide solution during pulsed laser irradiation only in seconds. Graphene oxide has a yellow-brown color and instantaneously turned black, a major feature of graphene solutions, indicating that graphene oxide could be rapidly reduced by pulsed laser irradiation[49]. In the case of graphene oxide films, a focused laser beam can reach higher power densities than a xenon flash lamp, as well provide highly-localized heated film area. As a result, the electric resistivity and conductivity of as-reduced graphene films have strong dependences on output power of laser. Compared to chemical and thermal reduction techniques, laser reduction can produce rGO films with higher conductivity thus the micro-nanoprocessing of graphene with laser technologies has paved the way for applications of graphene-based materials in electronic devices[50].

1.1.5. Doping of graphene

Although graphene has unique electrical properties, it's a zero-gap semiconductor and therefore tuning of its electronic properties via doping is a very interesting field. Tailoring the energy gap on the electronic structure of graphene in a controlled pathway is vital for many applications, including the performance of graphene-based transistors (Figure 1.5). Many recent studies have focused on the doping of graphene with chemical methods using fluorine, chlorine, bromine, ammonia[52] with an energy gap ranging from 0.64 to 0.3 eV[53]. The findings of these studies have shown that Cl is the weakest and most controllable for graphene doping. This is due to the Cl atoms that generate various states when they exposed on single-sided graphene. In the initial reaction stage, it forms Cl-graphene charge-transfer complex, the C orbitals keep sp^2 hybridization and the graphene is p-type doped. Upon further chlorination, the formation of a second adsorption configuration takes place: it is covalent bonding of Cl pairs, where the structure of the C atom is close to sp^3 hybridization[54]. Doping of graphene oxide can be achieved with thermal annealing[55], chemical methods[56] and irradiation with UV light in a liquid medium[57].

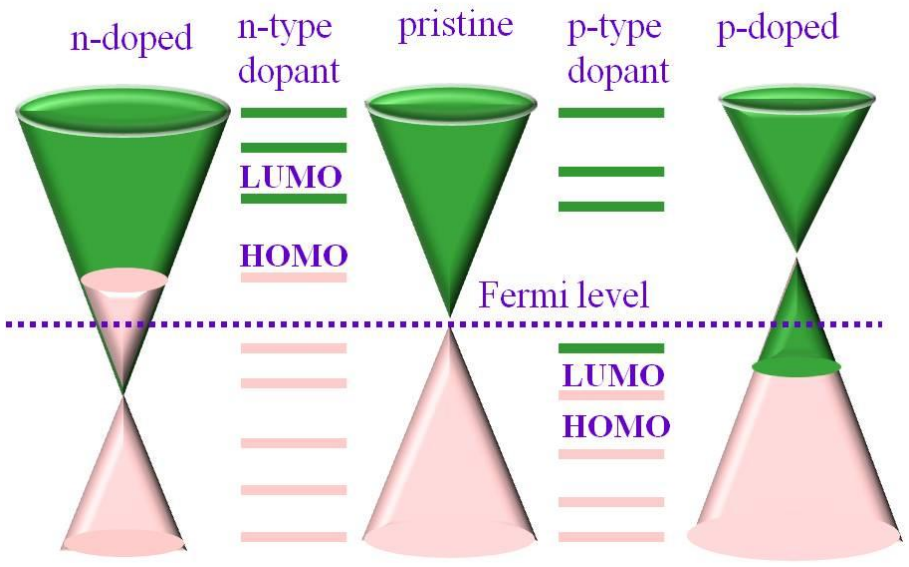

Figure 1.5: A schematic showing the relationship between positions of the HOMO–LUMO levels of dopants with respect to the Fermi level of graphene relevant for n- and p-type doping of graphene

1.1.6. Applications of reduced Graphene Oxide

The main goal for various applications is the high quality graphene production on a large scale that combines low cost and high performance. Reduced graphene oxide electronically is a semi-metal with finite density of states at the Fermi level, similar to disordered single and multilayered graphene, showing weak changes in electrical conductance with gate voltage in a field-effect device. Furthermore it is highly transparent in the visible spectrum because it is atomically thin[58]. That is the reason why reduced graphene oxide has been studied for transparent conductor applications such as in organic solar cells and organic light-emitting diodes. More specific, flexible, chemically derived reduced graphene oxide film has successfully transferred onto PET and used as a transparent, conductive electrode for organic photovoltaic devices[59]. Yin et al who presented this work, conclude that when the optical transmittance of reduced graphene oxide film was above 65%, there was a high dependence of device performance on the sheet resistance of reduced graphene oxide layer, which determines the charge transport efficiency.

Another promising application of functionalized graphene is the fabrication of sensors to diagnose diseases. Robinson et al reported the fabrication and characterization of molecular sensors based on reduced graphene oxide thin film networks. They found out that not only the reduced graphene oxide devices can achieve sensitivities for chemical warfare agents and explosives, but by adjusting the reduction process it can tailor the response and recovery characteristics of the conductance response. Also, they report that low-frequency noise of graphene oxide device is orders of magnitude lower than SWNT-based sensors and is sensitive to film thickness[60]. A very interesting work was presented by Guo et al[61] where with two-beam-laser interference they perform reduction, patterning and nanostructuring of graphene oxide for the production of a flexible humidity sensing device on flexible substrate of PET. The sensing performance is significantly improved by the presence of nanostructures that increases the surface area. The modulation of oxygen-group content controls the adsorption/desorption behavior of water molecules and contributes the tunable response/recovery time.

Furthermore, incorporation of reduced graphene oxide sheets into polymer or ceramic matrices has been demonstrated to exhibit remarkable improvements in the physical properties of the host material. Fabrication of reduced graphene oxide-polymer composite generally requires graphene oxide sheets to be functionalized, such that they are soluble in solvents that are compatible with host polymers. Composite thin films can be obtained via spin-coating such solution, followed by mild annealing to drive off residual solvents and reducing chemicals. Introduction of percolating reduced graphene network within an insulating material can render it semiconducting. For example, let's see the case for the transfer characteristics of a bottom-gated field-effect device consisting of polystyrene (PS) as the host and 10-vol % reduced graphene oxide as the filler material. The ambipolar characteristics are comparable to those of reduced graphene films suggesting that the influence of PS in charge conduction and gate capacitance is minor. The conductivity of these films at Vg=0V range from 1 to 24 Sm^{-1}, in agreement with the values reported for bulk composites. In contrast to reduced graphene oxide films, the field-effect mobility was found to be generally higher for holes than for electrons by a factor of 2–5 in vacuum, exhibiting values between 0.1 and 1 $cm^2V^{-1}s^{-1}$. Unlike reduced graphene films, the composite devices are only weakly sensitive to unintentional ambient doping, suggesting that the majority of reduced graphene responsible for the carrier transport are embedded within the PS. Thus, the insulating PS matrix provides structural integrity and air stability, while minimally interfering with the electrical properties of the rGO network[13]. Eda et al reported a solution-based method that allows uniform and controllable deposition of reduced graphene oxide thin films with thicknesses ranging from a single monolayer to several layers over large areas to create transistors and proof-of concept electrodes for organic photovoltaics. The thinnest films exhibit graphene-like ambipolar transistor characteristics, whereas thicker films behave as graphite-like semi-metals[14]. The fabrication of reduced graphene oxide FETs has become a favorite topic of analysis. Vasu et al, demonstrated top-gated field effect transistor made of reduced graphene oxide monolayer by dielectrophoresis, where the field effect transistor action was obtained by electrochemical top-gating using solid polymer electrolyte (PEO + $LiClO_4$) and Pt wire. Ambipolar nature of graphene flakes was observed upto a doping level of ~ $6x10^{12}/cm^2$ and carrier mobility of ~ 50 $cm^2V^{-1}sec^{-1}$ [62]. Joung et al presented high yield fabrication of field effect transistors using chemically reduced graphene oxide sheets suspended in water assembled via

dielectrophoresis. The two terminal resistances of the devices were improved by an order of magnitude upon mild annealing at 200 ^{0}C in Ar/H_2 environment for 1 hour. With the application of a back-gate voltage, all of the devices showed FET behavior with maximum hole and electron mobilities of 4.0 and 1.5 cm^2/Vs respectively[63]. Moreover, an interesting work was reported by Guo et al, a femtosecond laser mediated band-gap tailoring of graphene oxides for direct fabrication of graphene-based microdevices. When femtosecond laser pulses were used to reduce and pattern graphene oxide, oxygen contents in the reduced region could be modulated by varying the laser power. In this way, the bandgap of reduced graphene oxide was precisely modulated from 2.4 to 0.9 eV by tuning the femtosecond laser power from 0 to 23 mW. The essence of GO bandgap tailoring is proved to be femtosecond laser reduction induced oxygen-content modulation. As representative illustrations, bottom-gate graphene FETs were fabricated in situ by using femtosecond laser reduced GO as the channel material, and an optimized room temperature on−off ratio of 56 was obtained[64].

1.2. Transition metal dichalcogenide materials

Layered compounds involving transition metal dichalcogenides (TMDs) are promising candidates for exploring atomically thin structures. TMDs are the most studied layered compounds that have been isolated in monolayer (1L) form by mechanical exfoliation. The most interesting feature about these materials is the remarkable change in optoelectronic properties compared with their bulk counterparts. In view of this, single layers of transition metal dichalcogenides have attracted notable attention. Despite the similarity in the chemical formula MX_2, where typically M is a transition metal and X is a chalcogen, different types of single layer TMDs act as insulators to semiconductors and semimetals to metals. There are many layered materials with strong in-plane chemical bonds and weak coupling between layers. The family of layered Van der Waals materials with weak Van der Waals forces between layers, make them suitable for exfoliation[1]. Materials like MoS_2, $MoSe_2$, WSe_2, have been widely studied for applications. The band gaps of these materials can be tuned by stacking confinement and under the impact of strong electric fields.

In TMDs, the transition metal atoms are sandwiched between two layers of chalcogen atoms. Specifically, one transition metal atom is bonded to six chalcogen atoms to form either octahedral or trigonal prismatic polyhedrons. Accordingly, the bulk layered TMD is constituted of strong intralayer covalent M-X bonds and weak interlayer Van der Waals forces. There is a variety of stacking polytypes of bulk Mo and W. The most common three are the 1T, 2H and 3R phases[65] (T: Trigonal, H: Hexagonal, R: Rhombohedral). As we can see in figure 1.6, the 1T phase has tetragonal symmetry with octahedral coordination, the 2H phase has hexagonal symmetry with trigonal prismatic coordination and 3R phase has rhombohedral symmetry with trigonal prismatic coordination. The 2H phase is the most stable phase of WS_2. As the number of layers decreased to one, there is no variety of stacking different layers, just 1H and 1T. The coordination of metal atoms is trigonal prismatic in the 1H phase and octahedral in the 1T phase, as we can see in figure 1.7 (a) and (b). The 1H phase is the most common phase for WS_2 monolayer. The number one (1) indicates the number of layers in a unit cell (ex. 1H has one unit cell). The structure of

2 WS consist of an atomic plane of W, which is sandwiched between the two atomic planes of S in a trigonal prismatic arrangement S-W-S[66]. The layer thickness is 0.6 − 0.7 nm[67].

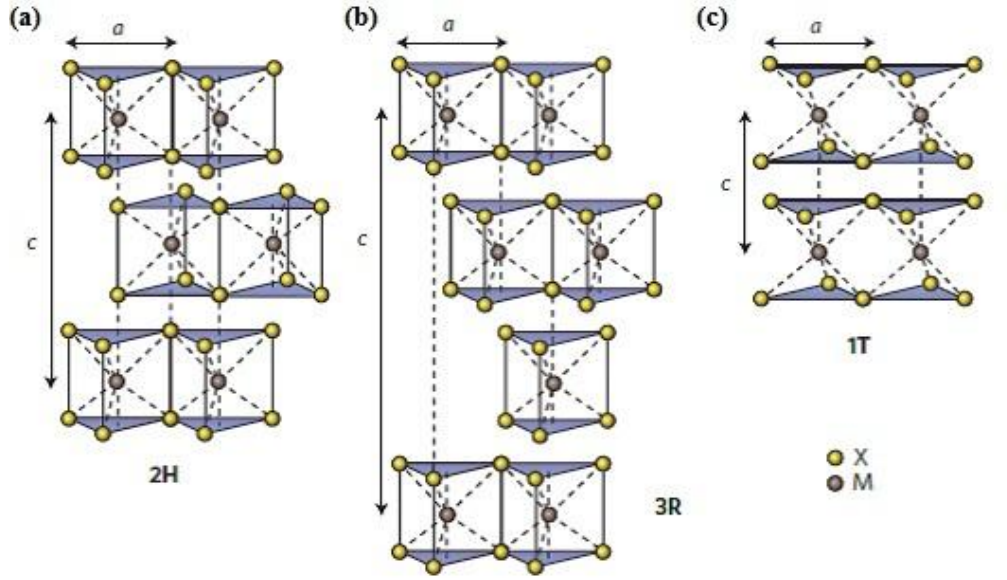

Figure 1.6: The structure of the (a) 2H , (b) 3R and (c) 1T phases of tungsten disulfide. The metal atoms (M) are grey and the chalcogen atoms (X) are yellow[65].

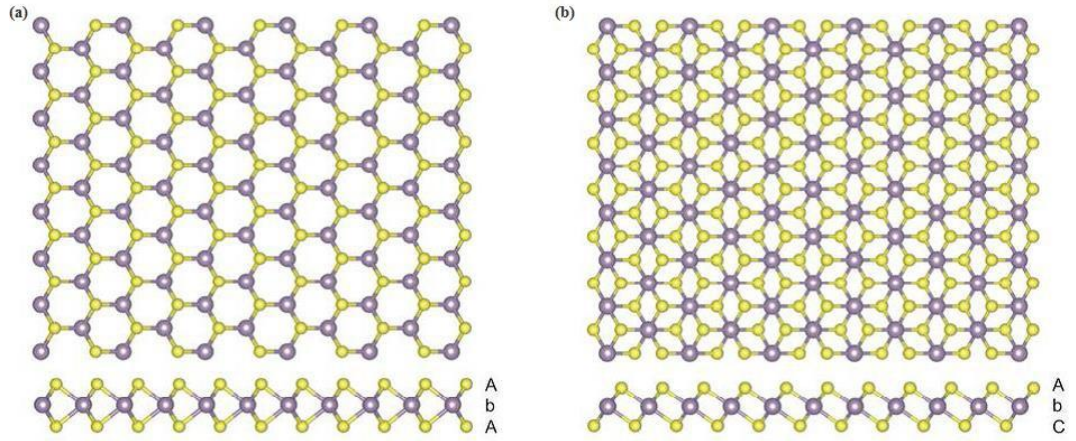

Figure 1.7: C-axis view of single-layer TMD with (a) trigonal prismatic (1H) and (b)octahedral coordination (1T). Purple spheres are the metal atoms and yellow spheres are the chalcogen. The labels AbA and AbC represent the stacking sequence where the upper- and lower- case letters chalcogen and metal elements, respectively[67].

TMDs have the advantage over other semiconducting materials by showing a good photoanode stability under liquid electrolyte, which makes them promising materials for electrochemical solar cells[68,69]. Moreover, quite high conversion efficiencies could be achieved, provided that the surfaces of the photoanodes had a smooth morphology because the cracks, ruptured films reduce the photocurrents and fill factors, which was explained by dangling bonds on the (100) or (010) surfaces at the steps, leading to an enhanced recombination of photogenerated electron–hole pairs. By improving these factors Prof. Tenne and co-workers were able to achieve efficiencies up to 13–14%[70]. In the recent years, Kis and co-workers[71] reported the first field-effect transistor consisting of a 2D single layer of the semiconductor MoS_2 as a conductive channel and HfO_2 as a gate insulator. The device exhibited a current on/off ratio at room temperature with mobility close to that achieved in thin silicon films or graphene nanoribbons. Therefore, metal chalcogenides monolayers gated by metal oxides epitaxially connected to conductive metals might exhibit interesting properties that require thin transparent semiconductors such as energy harvesting and optoelectronics.

1.2.1. Inorganic Fullerene-like Nanoparticles and Inorganic Nanotubes

Following the discovery of carbon nanotubes, nanostructured materials and their syntheses have attracted tremendous attention due to their superior mechanical and electronic properties and therefore, their high potential in making advanced nanodevices. Along with carbon nanotubes, many non-carbon nanostructures have been synthesized during the past few years. The TMDs manifest appreciable multiplicity in their physical properties, from the fields of metals, to semiconductors, insulator and superconductors. A significant characteristic of these materials is that they crystallize in a quasi two-dimensional type of layered structure that gives considerable anisotropy to many of their properties. In addition, the layered structure of MoS_2 is very similar to graphite structure. This particular aspect allows synthesize fullerene-like structures and nanotubes from inorganic compounds with a crystal

structure akin to graphite. Nanoparticles of compounds with a layered structure go under the large surface energy correlated with the external atoms and fold into hollow cage-like structures. To get over the large elastic energy associated with the folding process, considerable activation energy must be supported for the process to take place, otherwise the reaction is very slow[72].

Due to their remarkable geometry and promising physical properties, the study of inorganic layered chalcogenide nanostructures has become one of the key topics in nanoscale research. This is since the first report on WS_2 nanotubes and nested MoS_2 fullerene-like nanoparticles by Tenne and his co-workers in 1992[73] and 1993 respectivley[74], syntrhsized upon heating thin metal films of W and Mo in the presence of gaseous H_2S. Various approaches to other inorganic fullerenes and nanotubes, such as BN[75], $NiCl_2$[76], Hf_2S[77], Cs_2O[78] and Tl_2O[79] have also been reported, which implies that many layer compounds may form fullerenes or nanotubes under favorable conditions. Similar to their carbon congeners chalcogenide nanoparticles are not equilibrium but high temperature and low-pressure phases that are obtained by quenching ‘‘hot’’ gas phase species. However, the synthesis of inorganic nanotubes and fullerenes is, in contrast to carbon, difficult, owing to their wall thickness of three atom layers. As a results, considerable strain energy is required to achieve surface curvature[80].

1.2.2. Synthesis of Inorganic Nanotubes and Fullerene-like Nanoparticles

There is a whole range of synthetic strategies that have been developed for the preparation of inorganic nanotubes (INTs) and fullerene-like nanoparticles (Ifs). While the structure and shape control of IFs and INTs is not nearly as effective as in the case of carbon fullerenes and nanotubes, some of the successful methods demonstrated partial controllability. A characteristic feature of all closed-shell structures is that high reaction temperatures (>800ºC) or large activation energies are needed to overcome the activation barrier associated with the bending of the otherwise flat 2D layers[81]. Figure 1.8 shows the W-S phase-diagram. The existence-zone for the IF phase is situated on the phase boundary between the a-WS_3 phase and

the crystalline 2H-WS_2 phase. Controlled heating of the a-WS_3 sample at temperatures close to 850 ^oC leads to a loss of one sulfur atom and crystallization of the IF nanophase.

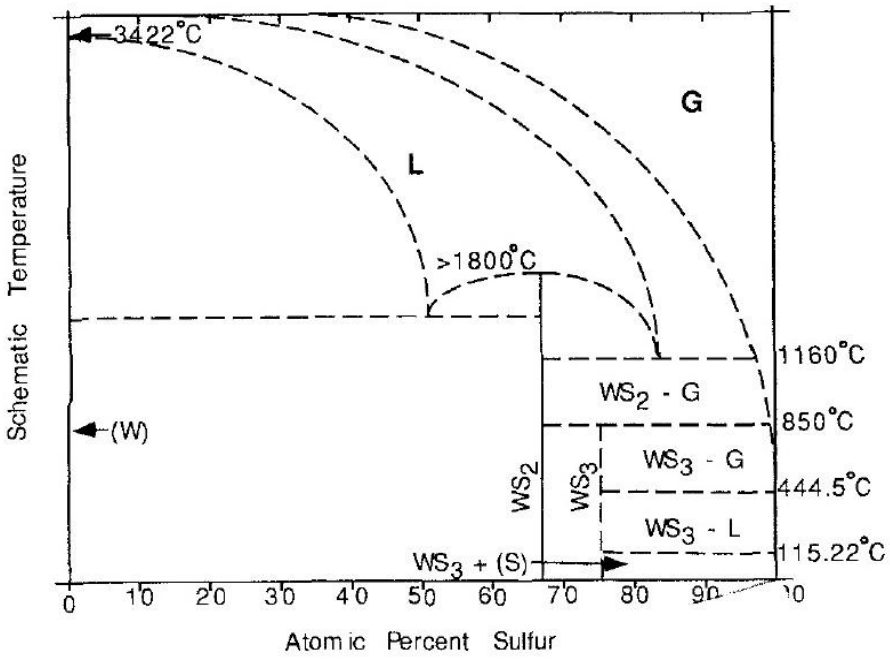

Figure 1.8: Phase diagram of the W-S system. The existence zone of is at the phase boundary between the amorphous a-WS_3 and the 2H-WS_2 phases[81]

In the following decade a variety of methods were utilized for the synthesis of IF or NT structures of MX_2 materials. The most common synthesized method is the sulfidization of metal oxides[82,83,84,85,86,87,88,89] in the presence of H_2S. Other techniques include arc discharge [90,91], chemical vapor transport[92], microwave plasma[93,94], atmospheric pressure chemical vapor deposition (APCVD)[95], solar ablation in the presence of a metallic catalyst[96] and laser ablation[97,98,99,100].

For the formation of hollow closed structures from layered compounds, it's possible to divide into two kinds of procedures: (a) synthetic procedures that arise far from equilibrium, and (b) synthetic procedures that are near to equilibrium conditions. The growth mechanism of IF-MS_2 (M =Mo, W) materials by the sulfidization of the respective oxide nanoparticles has been well described by Feldman et al[101]. The initial step in this reaction is the sulfidization of the surface of the oxide nanoparticles at

temperatures between 750 and 900 ^{o}C in an almost instantaneous reaction. This first sulfide layer passivates the nanoparticle surface and prevents coarsening of the nanoparticles into larger platelets. In the next slow step, the partially reduced oxide core is converted into metalsulfide in a quasi-epitaxial layer by layer process, leading to a nested multilayer core[102]. A schematic representation of the growth mode of an IF particle is depicted in Figure 1.9.

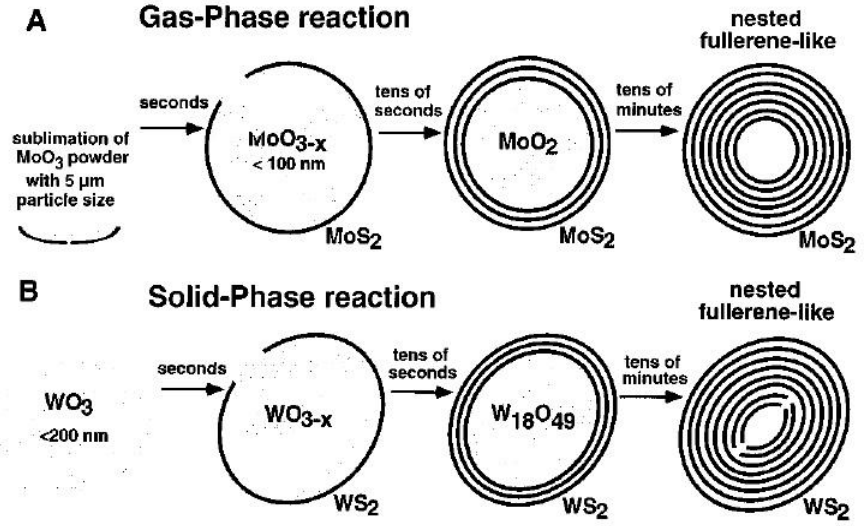

Figure 1.9: Schematic representation of the growth model of the inorganic fullerene-like phase of (a) MoS_2 and (b) WS_2 nested polyhedra from oxide nanoparticles[101]

In the case of INTs, we can distinguish between two growth modes of such nanotubes from the respective WO_{3-x} powder. In the first mode (type I, Figure 1.10a), a spontaneous growth of rather slender nanotubes with diameter between 15 and 30 nm was described[103,104]. This process is dictated entirely by fast kinetics and is therefore difficult to control. Not surprisingly therefore, harnessing this process to produce a pure INT-WS_2 phase proved to be beyond reach. Contrarily, in the type II growth mode (Figure 1.10b), the oxide powder is partially reduced and is rapidly converted into $W_{18}O_{47}$ nanowhiskers, in a kinetically controlled process. Subsequently, the oxide nanowhiskers are converted into a pure INT-WS_2 phase through a slow diffusion controlled process[105,106]. In this case, the synthesized nanotubes are 30–150 nm in diameter and 2–20 mm and above in length[107]. This

process is able to provide currently half a kg/batch of multiwall WS_2 nanotubes, and further scale-up is foreseen[108].

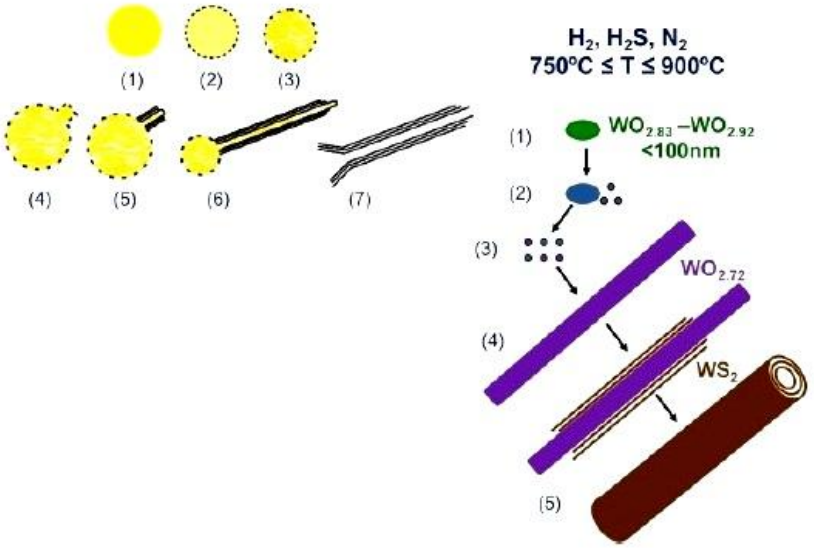

Figure 1.10: The two growth modes of INT-WS2. (a) (left) Type I spontaneous growth. (b) (right) Type II growth mode involving first growth of $W_{18}O_{47}$ nanowhiskers and their subsequent sulfidization[108]

As demonstrated in Figure 1.11, the phase behavior of Mo and S in nano regime, which stated the origin of bulk MoS_2 from the elements, once clarified the phase behavior of small Mo–S clusters. It was clearly determined that below a few hundred atoms, the trigonal prismatic Mo–S bond is unstable. Rather clusters of the type Mo_4S_6 and Mo_6S_8 made of inner Mo polyhedra and surrounded by sulfur polyhedra are stable below calculated 100 atoms. Multiwall MoS_2 nanooctahedra, made of six symmetrically disposed rhombi (and two missing sulfur atoms) in the corners become stable between 103–105 atoms (3–7 nm in size) and are indeed the smallest hollow closed structures or th as called the true MoS_2 fullerenes. Further than this size and probably up to about 10^7 atoms (calculated 20–200 nm), the INTs and IFs MoS_2 become stable. Bulk 2H-MoS_2 platelets become the most stable species at still larger sizes (>0.3 micron)[109].

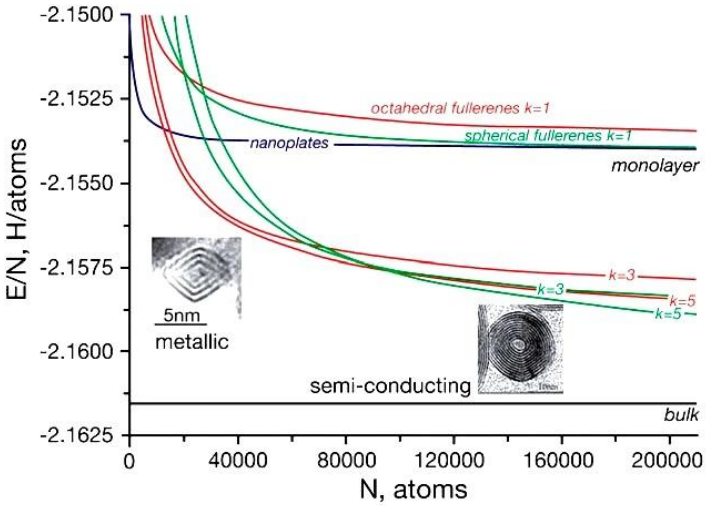

Figure 1.11: The dependence of the energy per atom E_t/N on the total number of atoms N for various MoS_2 nanostructures: triangular nanoplatelets (blue); octahedral fullerenes with k shells (red), and spherical fullerene-like nanoparticles (green) with k shells[110]

The strain energy/atom varies usually as $1 / R^2$, where R is the radius of the nanotube. For a given diameter, the strain in MoS_2 nanotubes is about one order of magnitude larger than that for carbon nanotubes (Figure 1.11). Normally, the strain effects promote the formation of MoS_2 nanotubes in larger diameter (>15 nm) as compared with carbon nanotubes (typically 1.5 nm). Moreover, it has been shown that the van der Waals interaction between the molecular sheets enhances the stability of multiwall (5–10 layers) nanotubes. However, given the fact that the van der Waals interaction is appreciably weaker than the Mo–S bond energy, it was hypothesized that high-temperature synthesis followed by rapid quench will favor single (or double) wall nanotubes and fullerene-like nanoparticles[109].

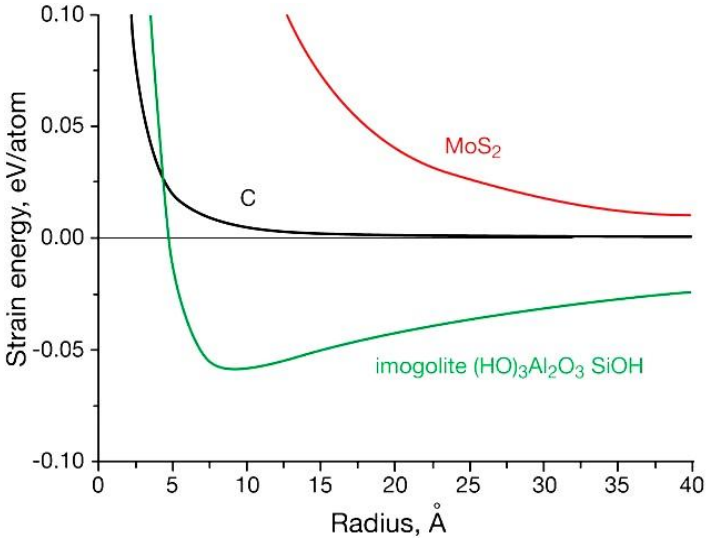

Figure 1.12: Graph showing the calculated elastic energy/atom as a function of (zig-zag) nanotube diameter for carbon, MoS_2 and imogolite nanotubes[109]

The combination from that theoretical–experimental study concluded that the nanooctahedra are stable over a limited range of about 5000–100000 atoms (3–6 nm). Below this size, MoS_2 nanoplatelets are more stable, whereas quasi-spherical closed cage IF nanoparticles become the most stable species above the higher limit. At even larger sizes (approximately 107 atoms) macroscopic MoS_2 platelets become the most stable structure. Furthermore, whereas MoS_2 platelets and the quasi-spherical nested structures are semiconductors, the nanooctahedra are metallic. This seems to be related to the enhanced density of states at the rim of the facets[111].

Synthesizing IFs/INTs with small number of walls and with smaller diameters is much challenging due to high elastic energy of folding. In Figure 1.13 is demonstrated the energy per atom of MoS_2 nanotubes with respect to the number of atoms in the unit length for different number of layers, which are calculated by density functional tight-binding theory. Also is compared the energy of nanoribbons of MoS_2 with the same number of layers. The energy per atom increases as the number of atoms decreases in both nanotubes and nanoribbons. Dangling bonds in the rim of the nanoribbons are responsible for increased energy per atom, where as increased elastic energy of folding makes the nanotubes less stable at smaller diameters. Below a certain point, the energy of folding increases more steeply for nanotubes than the energy of the nanoribbons, which leads to a lesser stability of

smaller diameter nanotubes compared to straight nanoribbons[94]. Thus, synthesizing smaller diameter INTs/IFs demands exotic reaction conditions.

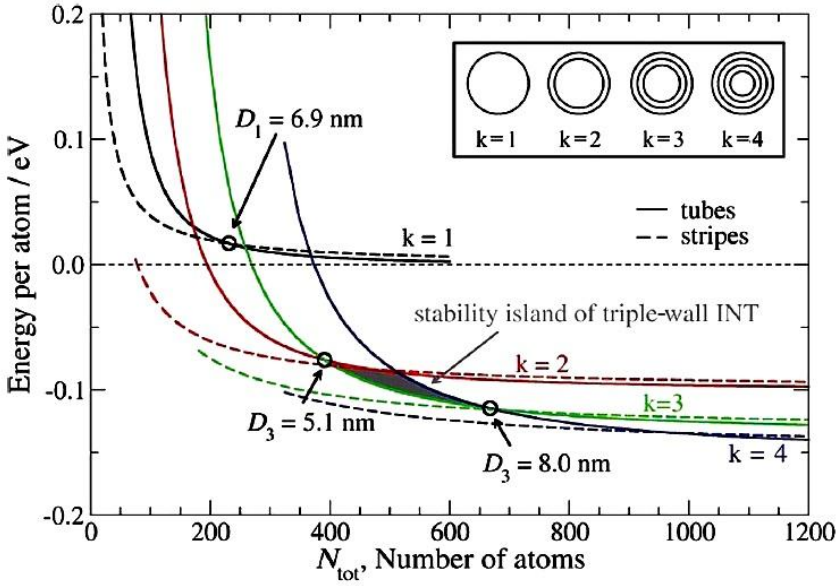

Figure 1.13: The calculated energy-per-atom for MoS_2 nanotubes and nanostripes with 1–4 walls as a function of the number of atoms in the tube unit cell, N_{tot}[94]

On the other hand, WS_2 nanotubes with smaller diameters (3–7nm) with less number of walls (1–3) were realized by inductively coupled radio frequency plasma irradiation of multi-wall WS_2 nanotubes. Under these conditions, the electron temperature reaches 10^4 K. Interaction of the plasma with either point or line defect on the surface results in exfoliation of a few nanoslabs on top of the multi-walled nanotubes, subsequently leading to unzipping of nanosheets from the outer surface. The elastic strain energy of rolled sheet on top of the nanotube is released when it gets exfoliated through an inverted umbrella effect, as a result small daughter nanotubes on top of the multi-wall WS_2 nanotubes. The nanotube yield was found to increase up to a certain degree both with reaction time and with the plasma power.

1.2.3. Properties of Inorganic Nanotubes and Fullerene-like Nanoparticles

Mechanical properties: Inorganic nanotubes show extensive potential for becoming part of ultrahigh strength nanocomposites technology. Several studies were carried out to investigate the mechanical properties of WS_2 nanotubes[112,113]. The ultimate strength and the maximal elongation of the WS_2 nanotubes were determined as well and were found to be 3.7-16.3 GPa (±11%) and 5- 14% (±0.1%), respectively with 50% of the tested nanotubes exhibiting strength above 13 GPa. The high tensile strength of these nanotubes seems to be very promising compared to other known high strength materials[114]. The combination of high tensile strength and calculated 12% elongation is a unique property for all the nanotubes, which were measured so far[115]. Furthermore, the strength of the strongest nanotubes is about 11% of its Young's modulus, corresponding approximately to the theoretical value of the material's strength. Figure 1.14 shows a snapshot taken during a tensile test of an individual WS_2 nanotube along with the stress–strain curve of this nanotube. The nanotube showed elastic (linear) behavior almost to failure. The Young's modulus calculated from the slope of the curve; strength and strain at yielding are 160 GPa, 17 and 10%, respectively. Nearly the half of the measured nanotubes showed strength in excess of 13 GPa showing that they are basically free of critical defects[116].

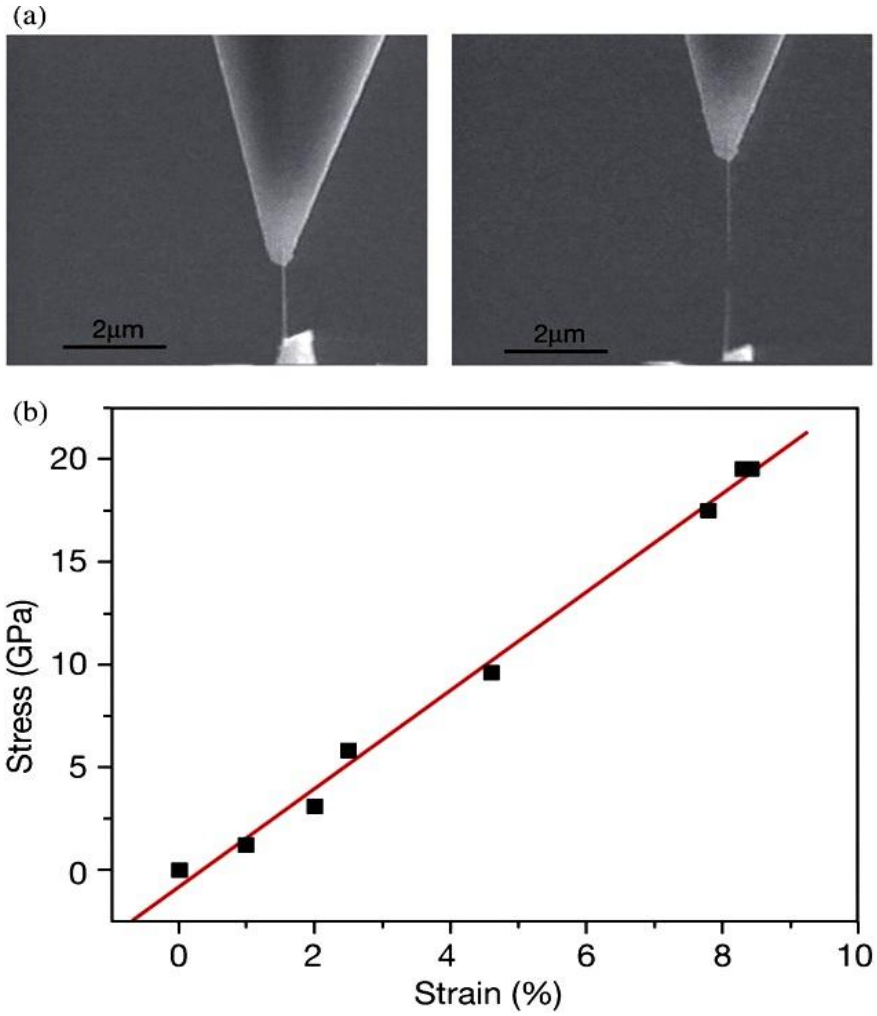

Figure 1.14: (a) SEM images of a WS_2 nanotube during a tensile test: before (left) and after (right) failure, (b) Strain–stress curve of such a nanotube[116]

Electronic properties: The extensive theoretical work that has been done on the electronic structure of MoS_2 and WS_2 nanotubes, demonstrate that the semiconductivity of MoS_2 and WS_2 is preserved in the nanotubes, regardless of their chirality[117,118]. The strain induced by the bending of the molecular sheet leads to distortion of the chemical bonds and hence shrinkage of the forbidden gap with decreasing diameter of the nanotubes. On the other hand the electron wave function is believed to be confined in the closed layer itself, producing a very small quantum size effect. Therefore, the band gap seems to decrease with shrinking diameter of the nanotube, which is an opposite effect to the generic quantum size effect in

semiconductor nanoparticles[119]. Some of the theoretical findings were confirmed by scanning tunneling microscopy (STM) experiments of WS_2 nanotubes[120].

Tribological properties: MoS_2 and WS_2 have been shown to be excelent solid lubricants[121]. Molybdenum disulphide is the most commonly used and studied transition metal dichalcogen lubricant. It provides an ultra-low friction surface ($0.008 < \mu < 0.05$) and long wear life in dry environments, vacuum and high temperatures. The presence of moisture severely curtails its wear life by several orders of magnitude and causes a rise in the friction coefficient to 0.1-0.2. Furthermore, WS_2 is more resistant to oxidation at elevated temperatures providing about a 100 ^oC increase in maximum operating temperature up to 650 ^oC[122].

1.2.4. Applications of Inorganic Nanotubes and Fullerene-like Nanoparticles

Numerous applications have been demonstrated for inorganic nanotubes and fullerene like nanoparticles the most prominent one being, as we already referred, their use as solid lubricants, heterogeneous catalysts, super shock absorbers, or battery materials.

Following intense research and development efforts, a large number of products based on (industrial grade) IFs as additives in different oils and greases and for machine working fluids were commercialized. The production of IF nanoparticle-formulated lubricants (oils and greases) has reached sales over 1000 metric tons per year[123]. Furthermore, being minerals that are mined for many decades, it is accepted that WS_2 and MoS_2 are environment friendly, nontoxic materials as well as biocompatible[19]. The combination of their excellent tribological performance and their mechanical robustness, offer these IF/INT several intriguing medical applications. Metallic coatings impregnated with IF nanoparticles were shown to be self-lubricating and could find medical applications for exapmle as coatings of orthodontic archwires[124].

In recent years, various groups started studying the reinforcing effect of IFs/INTs in polymer nanocomposites, with the first study dated back to 2003[125] and

2004[126]. The good mechanical properties of IFs/INTs as mentioned above, give opportunities to use it as a minority phase in composite materials for improving their mechanical behavior and thermal stability. These materials find application in various fields including high-strength construction materials, shielding, surface transportation etc[19].

Moreover, IFs/INTs are discussed as battery material in nanocircuits. Zak et al.[127] studied the intercalation of alkali metals into MoS_2 and WS_2-IFs and found a reversible intercalation behavior. Intercalated material exhibited a significantly higher electrical conductivity and was paramagnetic opposed to the diamagnetism of the pristine sample. Another important field in which INTs can be useful is as tips in scanning-probe microscopy. Various inorganic nanotubes exhibit strong absorption of light in the visible part of the spectrum, and their electrical conductivity can be varied over many orders of magnitude by doping and intercalation. This suggests numerous possible applications in areas such as nanolithography, photocatalysis, sensors, and others. The technology of fabrication of such tips has been largely improved, bringing this technology one step closer to a genuine application[128].

1.3. Objectives and motivations

The main objective of the current Thesis is to develop laser-based methods for the synthesis of 1D and 2D nanomaterials based on Graphene and TMDs. In particular we demonstrate: a) simple techniques for the controllable reduction and doping of the graphene oxide lattice as well as b) the development of environmentally friendly synthetic methods for low-dimensional transition metal dichalcogenide nanomaterials.

In particular, the development of novel methods for realizing graphene electrodes without the need of high-temperature annealing, is highly desirable. In this thesis we demonstrate that laser reduced graphene oxide electrodes as a low-cost, high-throughput and facile approach for the development of transparent conductive electrodes (TCE) in organic photovoltaic devices (OPVs) to replace traditional indium tin oxide (ITO) electrodes. Furthermore we show that laser-induced doping of graphene oxide as a new method to develop graphene-based field effect transistors.

Among the advantages of laser-based processes is that they do not rely on the use of chemicals or high temperatures, while the photoreaction time is shortened from several hours to a few minutes.

Besides this, we demonstrate that laser ablation of solid TMDs targets is a simple, environmental friendly and reproducible way to generate a large number of intriguing nanometric TMD structures with variety of properties. MoS_2 and WS_2 nanostructures are usually synthesized through gas phase reactions with appropriate reactors. The main problem of these procedures is the difficulty to work with dangerous gases, like H_2S and the need to work at high temperature, above 950 °C. We show that the laser-based approach is a single step and could address all the above challenges. Furthermore, the non-equilibrium conditions that typically observed during the laser ablation process open up the way to new synthetic routes.

Chapter II: Experimental and characterization methods

2.1. Synthetic processes

2.1.1. Photochemical reduction and doping

In recent years, photo-reduction has emerged as an appealing alternative because photo-reduction does not rely on either high temperature or toxic chemicals. Photo-reduction of GO has unique properties such as mask-free patterning, room-temperature processing, chemical-free and non-contact treatment, controllable reduction, as well as the formation of micro-nanostructures. Laser sources have been employed for deoxygenation of graphene, dehydrogenation and dehalogenation of graphene surface. Such laser induced bond dissociation paves the way for achieving desired band gap in graphene by adequately controlling the extent of such surface bonds. In spite of a certain amount of carboxyl groups remaining, most of the hydroxyl groups of the GO could be selectively removed through this simple irradiation. In our previous work, performed during my MSc thesis[129], we have shown that laser-in situ photothermal reduction of GO on flexible substrate is an one-step and highly efficient reduction technique, compared to the conventional ones. The photoreduction process is one-step, facile, and is rapidly carried out at room temperature in air without affecting the integrity of the graphene lattice or the flexibility of the underlying substrate. In Figure 2.1 a schematic of the GO reduction upon laser irradiation, is demonstrated. Due to the ultrashort pulse duration, selective removal of the oxygen groups on GO sheets takes place in air without any ablation occurring. By carefully tuning key laser parameters, the reduction degree of GO could be controlled in the irradiated region.

According to Smirnov's results, the threshold for GO reduction is 3.2 eV (λ<390 nm). In principle, reduction of GO could be achieved either by UV or visible laser source. If the laser source has wavelength smaller than 390 nm, for instance an

excimer laser (248 nm), GO would mainly undergo a photochemical process, whereas for laser sources with wavelength larger than 390 nm, GO undergoes photothermal process. Since the energy is provided by a light source, precise control over the wavelength range, intensity and exposure duration lead to the controllable reduction of GO. Photochemical reduction technique proved to be a useful tool for the doping of GO, as it is presented in chapter 3.

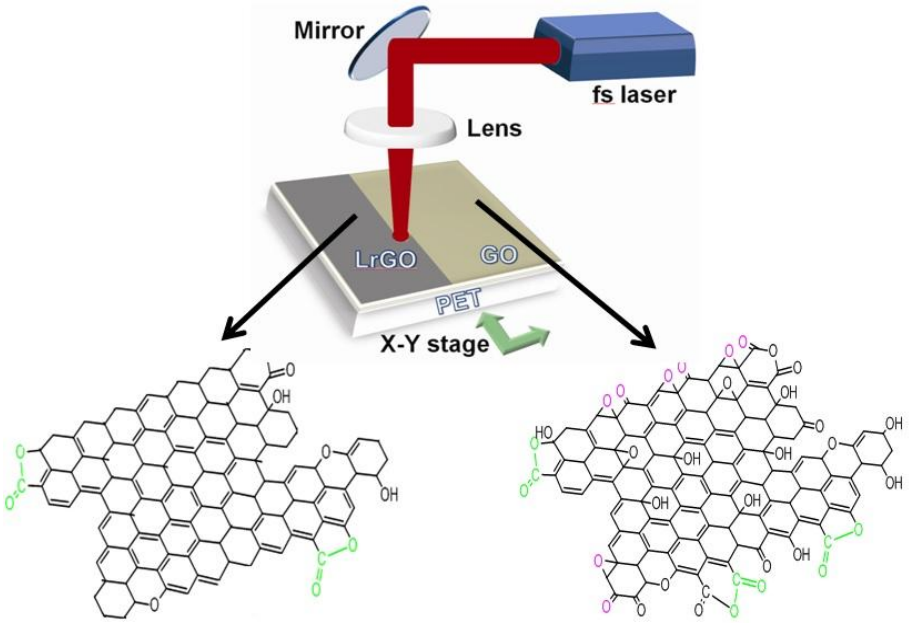

Figure 2.1: Schematic representation of the laser-in situ photothermal reduction of GO

2.1.2. Ultra-short pulsed laser ablation in ambient air

During the interaction of low intensity short laser pulses with solid targets, the laser energy is absorbed by free electrons, due to the inverse Bremsstrahlung process. Then the evolution of the absorbed laser energy involves thermalization within the electron subsystem, energy transfer to the lattice, and energy losses due to the electron heat transport into the target[130]. As a result, when the fluence of irradiating laser pulse

exceeds a certain threshold, a plasma plume is generated. Subsequent condensation of this plasma gives rise to the products of pulse laser ablation. It is widely known that, the ablation mechanisms are strongly dependent on the laser pulse duration. In case of nanosecond pulses, both photo-thermal and photochemical phenomena take place, while in case of femtosecond pulses photochemical phenomena are mainly observed; in general the shorter the pulse the less pronounce photo-thermal phenomena are taking place.

Using excimer laser ablation of pressed MoS_2 targets Parilla et al[131] produced nano-octahedra of MoS_2 of discrete sizes. These nano-octahedra were much larger than C_{60} structures, having edge lengths of about 4-5 nm. They were so-called the first 'inorganic fullerenes'. Following this work, numerous of studies and experiments were performed using the pulse laser ablation method to obtain inorganic fullerene nanostructures and inorganic nanotubes. Sen et al[98] used a combination of laser ablation and high temperatures to obtain hollow closed-cage onion structures of WS_2 and MoS_2 by solid targets. Similar techniques were also used for other layered materials like $NiCl_2$[132], TaS_2[133], Cs_2O[134], V_2O_5[135]. It was also reported by Wu et al[136] that laser ablation in liquids can provide MoS_2 nanoparticles with a good solubility and biocompatibility. However these methods use high temperatures during the laser ablation process and require the presence of a gas carrier. Therefore, methods to synthesize IFs/INTs in ambient air are desirable. In 2012, a new procedure of the synthesis of MoS_2 was reported with solar ablation in the presence of a metallic catalyst. Highly concentrated sunlight that creates strong temperature gradients and extended hot annealing regions, in the presence of a metallic (Pb) catalyst, were employed for the formation of various inorganic nanotubes[96]. In chapter 4 we present ultra-short pulsed laser ablation in ambient air, in the presence of a catalyst, as an efficient approach to synthesize both IFs and INTs nanostructures.

2.1.3. Pulsed Laser Deposition (PLD) of thin films

The technique of PLD has been used to deposit high quality films of materials for more than a decade. The technique uses high power laser pulses to melt, evaporate and ionize material from the surface of a target. This "ablation" event produces a

transient, highly luminous plasma plume that expands rapidly away from the target surface. The ablated material is collected on an appropriately placed substrate upon which it condenses and the thin film grows[137]. Laser beam is focused onto a target material maintained in a vacuum, typically better than 10^{-6} Torr or in a low pressure of background gas as is demonstrated in Figure 2.2. The target is usually rotated in order to avoid repeated ablation from the same spot on the target.

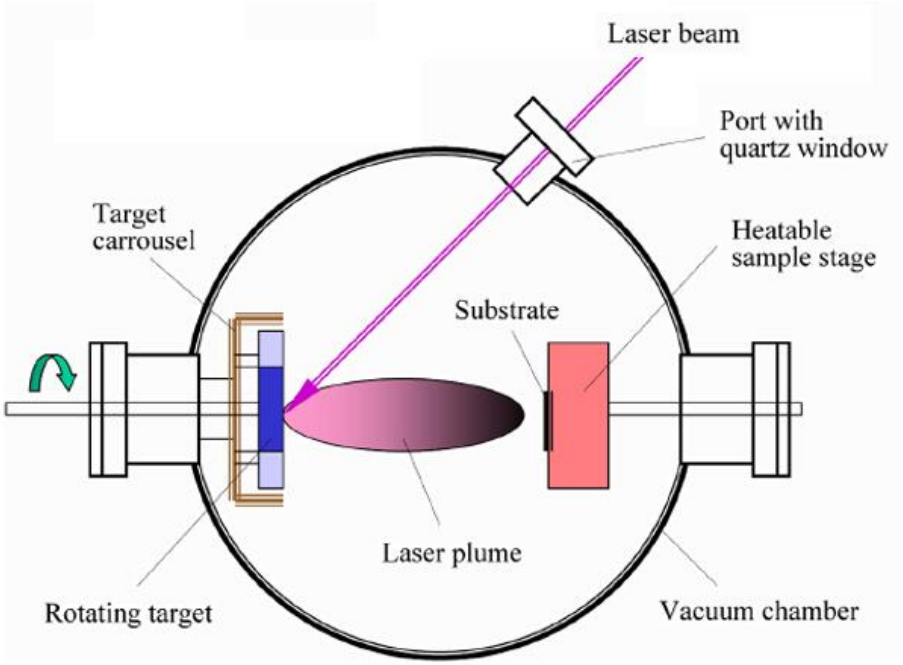

Figure 2.2: Schematic representation of an apparatus for pulse laser ablation of a solid target and subsequent deposition on a substrate[137].

During PLD, many experimental parameters can be changed, which then have a strong influence on film properties. The laser parameters such as laser fluence, wavelength, pulse duration and repetition rate can be altered. Moreover, the preparation conditions, including target-to-substrate distance, substrate temperature, background gas and pressure, may be varied, which all influence the film growth[138]. The benefits of the PLD technique over other film deposition methods are among others the use of a laser as an external energy source which results in an extremely clean process without filaments and that is why deposition can occur in both inert and reactive background gases. Furthermore, is the capability for stoichiometric transfer

of material from the target to substrate. This arises from the nonequilibrium nature of the ablation process itself due to absorption of high laser energy density by a small volume of material. For low laser fluence and/or low absorption at the laser wavelength, the laser pulse would simply heat the target, with ejected flux due to thermal evaporation of target species. An ablation threshold is reached as the laser fluence is increased, where laser energy absorption is higher than that needed for evaporation. The ablation threshold is dependent on the absorption coefficient of the material and is thus wavelength dependent.

The formation of multication thin-film materials often requires a reactive species (e.g., molecular oxygen for oxides) as a component of the flux. The amount of reactant gas required for phase formation will depend on the thermodynamic stability of the desired phase. Interaction of ablated species with the background gas often produces molecular species in the ablation plume where they facilitate multication phase formation. That is why a background gas indtroduced in PLD. Furthermore the background gas can also be used to reduce the kinetic energies of the ablated species[139].

The target-to-substrate distance can have significant impact on film growth properties, including particulate density, epitaxy, phase formation, and deposition rate. Ablation requires a target material possessing a high optical absorption coefficient at the selected laser wavelength. In general, only the cation stoichiometry needs to be identical to that of the films, assuming stoichiometric transfer and negligible evaporation from the film surface while the phase of the target does not need to be the same as that of the desired film. Efficient ablation of the target material requires the nonequilibrium excitation of the ablated volume to temperatures well above that required for evaporation. This generally requires the laser pulse to be short in duration, high in energy density and highly absorbed by the target material[139].

Pulsed laser evaporation depends on the type of interaction of the laser beam with the target and it can be classified into three separate regimes: (a) interaction of the laser beam with the target material resulting in evaporation of the surface layers, (b) interaction of the evaporated material with the incident laser beam resulting in an isothermal plasma formation and expansion and (c) anisotropic adiabatic expansion of the plasma that leads to the characteristic nature of the laser deposition process. The

first two regimes start with the laser pulse and continue until the laser pulse duration. The last regime starts after the laser pulse terminates (Figure 2.3).

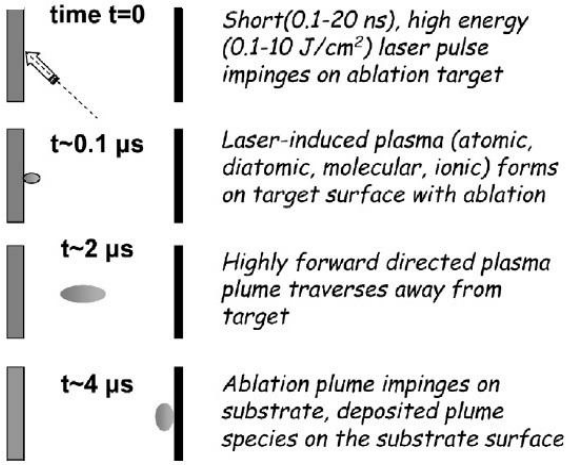

Figure 2.3: Schematic of the timescales involved in the PLD process[139]

The removal or sputtering of the material from the target by laser irradiation depends on the coupling of the beam with the solid. Intense heating of the surface layers by high-powered nanosecond laser pulses occurs, resulting in melting and/or evaporation of the surface layers, depending on its energy density. Using simple energy balance considerations, the amount of material evaporated per pulse is calculated. The energy deposited by the laser beam on the target is equal to the energy needed to vaporize the surface layers plus the conduction losses by the substrate and the absorption losses by the plasma. This is the energy threshold E_{th}, which represents the minimum energy above which appreciable evaporation is observed. As the plasma and other losses may vary with pulse energy density, E_{th} may vary with energy density[140].

The material evaporated from the hot target is further heated by the absorption of the laser radiation. Although the laser evaporation for the deposition of thin films occurs at much lower power densities, where plasma temperatures are of the order of 10^4 K, the heating mechanisms and other physical phenomena are similar to the laser-generated high-temperature plasma. The dominant mechanism may be the absorption of photons by free-free transitions involving neutral atoms, as a result of high neutral atom concentrations. A small proportion of free electrons results in a marked increase

in the absorption coefficient, and electron-ion collisions become the dominant heating process. The primary absorption mechanism for plasma is the electron-ion collisions, i.e., resistance to induced currents. The absorption primarily occurs via an inverse bremsstrahlung process, which involves the absorption of a photon by a free electron[140]. Because of the high expansion velocities of the leading plasma edge, the electron and ion densities decrease very rapidly with time, which makes the plasma transparent to the laser beam for larger distances away from the target surface. As the plasma is constantly augmented with evaporated particles at its inner edge adjacent to the target surface, a thin region near the surface is constantly absorbing the laser radiation during the time interval of the laser pulse[140].

There are no particles evaporated or injected into the inner edge of the plasma after the termination of the laser pulse, while an adiabatic expansion of the plasma occurs with a relation between the temperature and the dimensions of the plasma. It has been found for spherical plasmas that as the plasma expands, the temperature drops off rapidly. Due to the fact that energy is regained in the recombination of the ions, the drop is smaller at lower temperatures. In the adiabatic expansion regime, the velocity of the plasma increases due to a decrease in thermal energy of the plasma. Most of the thermal energy is converted into kinetic energy with the expansion of the plasma and there is no more energy left for the expansion process. That is why the plasma becomes elongated in the shorter dimensions and retains its profile during the deposition process. The shape of the expanding plasma controls the density distribution of particles in it. Thus, elliptical iso-thickness contours similar to the plasma shape after expansion should be observed in the film[140].

Several works have been demonstrated in the synthesis of MoS_2 and WS_2 films with the PLD technique[141]. One interesting study was the field electron emission investigations on pulsed laser-deposited MoS_2 thin films on W-tip and Si substrates, where a nanostructured morphology of MoS_2 that was synthesized with PLD, was important for local electric field enhancement in field emission application[142]. Also a direct fabrication of highly crystalline few-layer WS_2 on silver substrates by pulse laser deposition at the relatively low temperature of 450 ^{o}C was reported[143]. Based on the above results and research, the idea to grow hierarchical TMD structures, i.e the formation of WS_2 nanostructures onto a microstructured substrate comprising

microspikes for field emission application[144] was generated. In chapter 4 we present in more detail the PLD growth of such hierarchical TMD structures.

2.2. Characterization techniques

2.2.1. Raman spectroscopy

Raman spectroscopy is one of the most important spectroscopic techniques used to observe vibrational, rotational, and other low-frequency modes in a system. Raman spectroscopy is commonly used in chemistry to provide a structural fingerprint by which molecules can be identified.

The main features in the Raman spectra of graphitic carbon-based materials are the G and D peaks and their overtones. The first-order G and D peaks, both arising from vibrations of sp^2 carbon, appear at around 1580 and 1350 cm^{-1} respectively. The G peak corresponds to optical E_{2g} phonons at the Brillouin zone center and is due to bond stretching of sp^2 carbon pairs in both rings and chains. The D peak is due to the breathing mode of aromatic rings and requires a defect for its activation. The D-peak intensity is therefore often used as a measure for the degree of disorder. The overtone of the D peak, called 2D peak, appears around 2680 cm^{-1}, and its shift and shape has been correlated with the number of graphene layers. The 2D peak is attributed to double resonance transitions resulting in production of two phonons with opposite momentum. Furthermore, unlike the D peak, which is only Raman active in the presence of defects, the 2D peak is active even in the absence of any defects[13] (Figure 2.4). However, the Raman spectrum of the GO features D (~1350 cm^{-1}) and G (~1600cm^{-1}) bands. In GO, the G band broadens significantly and displays a shift to higher frequencies (blue-shift), and the D band grows in intensity. The increase of the intensity of D band indicates the reduction in size of the in-plane sp^2 domains, which is because of the introduction of abundant oxygen-containing groups. Following laser reduction, the D band is still very strong as presented in the Raman spectrum (Figure 2.5).

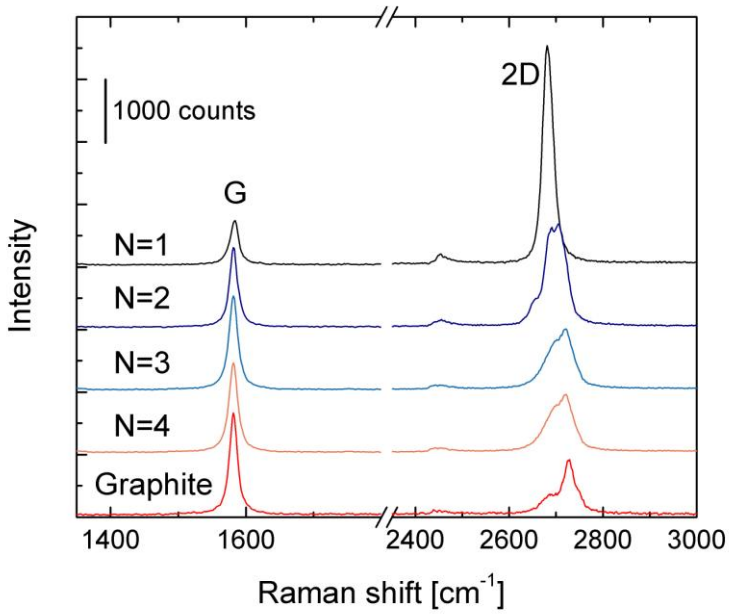

Figure 2.4: Layer dependence of graphene Raman spectrum. Raman spectra of N = 1-4 layers of graphene on Si/SiO_2 and of bulk graphite[5].

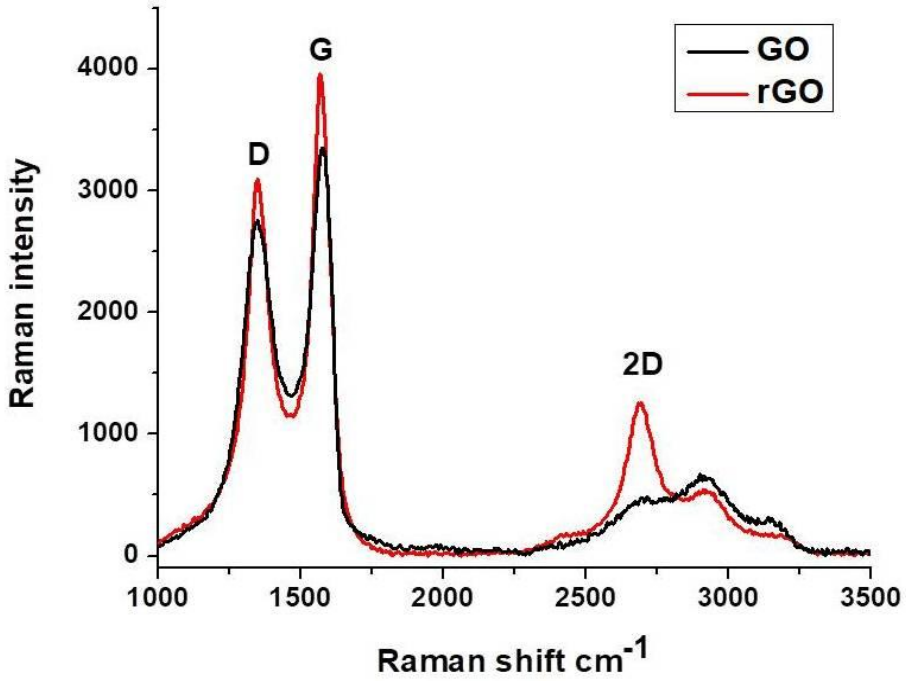

Figure 2.5: Raman spectra of GO (black line) and reduced GO (red line)

The intensity ratio of D band to G band of reduced GO increases compared to that in GO, which indicates the decrease of the average size of the sp^2 domains upon reduction. In a previous study on the laser in-situ photothermal reduction of GO, performed during my MSc thesis, to account for the crystalline quality of the reduced GO, the intensity ratio D/G, which is a measure of the lattice disorder, was monitored upon increasing the number of irradiation pulses at constant incident power. As shown in Figure 2.6, though the D/G intensity ratio of reduced GO becomes slightly lower for low N, it significantly increases after prolonged irradiation with higher number of pulses. Therefore, for low N, a non-thermal ultrafast excitation and subsequent removal of oxygen groups takes place, while the lattice order is preserved. With the progression of laser irradiation, thermal effects become more and more pronounced giving rise to photohermal breakage of carbon bonds, which increases the number of defects in the lattice and in turn leads to the formation of smaller and smaller crystalline graphene domains[129].

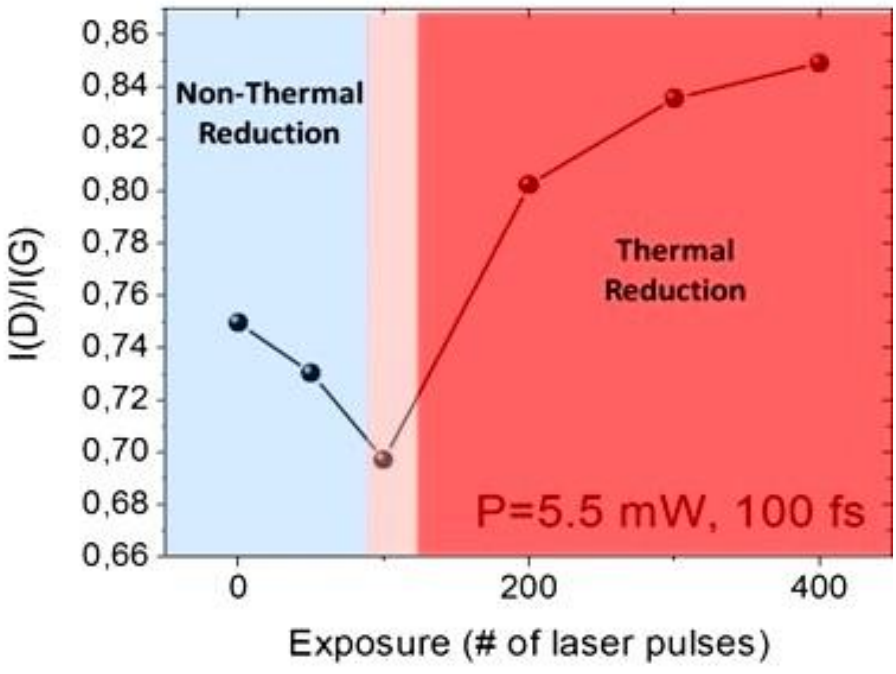

Figure 2.6: Dependence of the intensity ratio of D to G peak on the number of laser pulses per irradiating spot.[129]

Raman spectroscopy has become a very powerful tool for studying also one (Figure 2.7) and few layers (Figure 2.8) of tungsten disulfide WS_2. Raman spectroscopy can not only used to identify the number of layers, but also gives details about the electronic band structure, a determination of the structural distortion. Raman spectra for bulk WS_2 include first order modes at the Brillouin zone center E_{2g} (Γ), which is associated with the in-plane motion of the sulfur and tungsten atoms in opposite directions and A_{1g} (Γ) which is associated with out-of-plane motion of the sulfur atoms and LA(M) plus a zone-edge mode which has been identified as the longitudinal acoustic mode at the M point LA (M)[145].

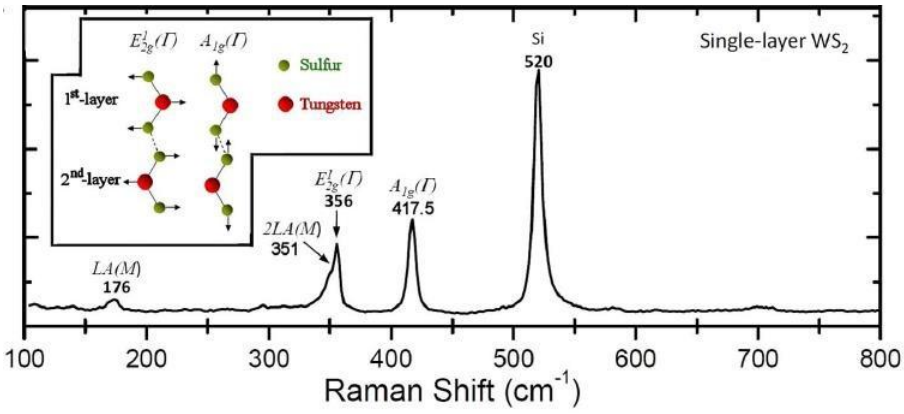

Figure 2.7: The atomic displacements for the in-plane phonon mode E_{2g} (Γ) and the out-of-plane phonon mode A_{1g} (Γ)[145].

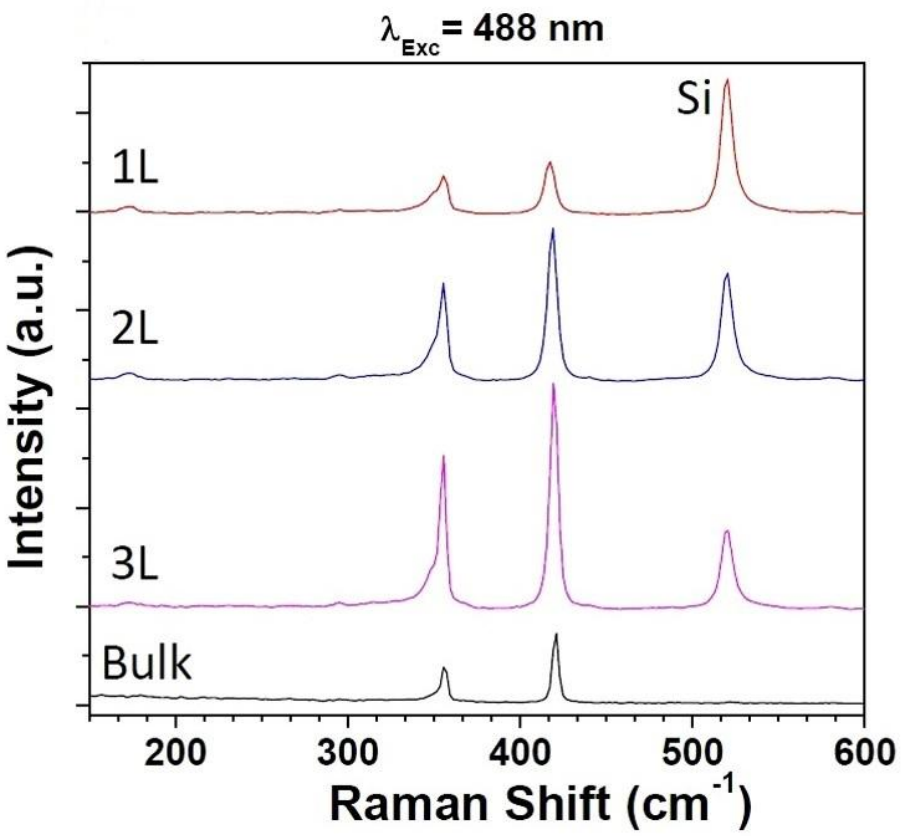

Figure 2.8: Raman spectra collected from regions with different WS_2 thicknesses (1L, 2L, 3L and bulk) using λ_{exc}=488nm[145].

Raman spectra of WS_2 nanotubes was also measured and compared to the bulk materials[146]. An up-shift of the peaks of the original A_{1g} (421 cm^{-1}) and E_{2g} (356 cm^{-1}) Raman modes was observed (Figure 2.9). This shift was attributed to the built-in strain in the nanotubes. Furthermore, electron diffraction analysis showed that locally the nanotubes crystallized in the high-pressure rhombohedral (3R) symmetry rather than the hexagonal symmetry, which is the stable polymorph in ambient conditions.

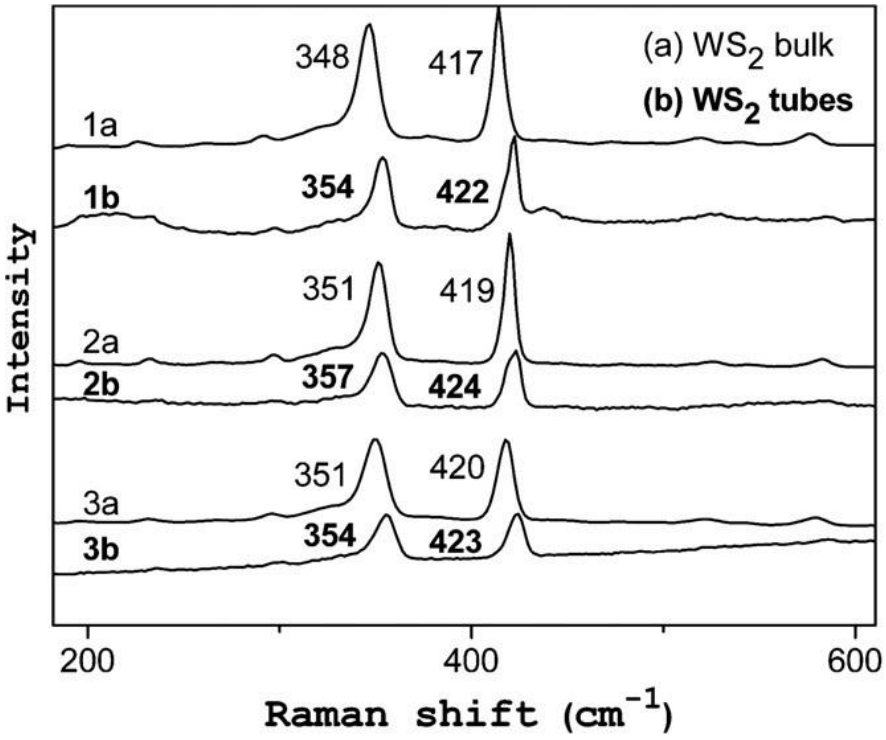

Figure 2.9: Raman spectra of WS_2 bulk (a curves) and WS_2 tubes (b curves). The two curves in each pair of bulk/tube spectra 1–3 are recorded in few seconds one by another, so that peak positions can be compared between the two curves in each pair[146].

Yu et al. studied the Raman lines of core (W)–shell IF-WS_2 nanoparticles as a function of the hydrostatic pressure in a diamond anvil cell[147]. The A_{1g} peak at 420 cm^{-1} was shown to contain a new low-energy shoulder at 416 cm^{-1} which is attributed to two-phonon coupling originating from longitudinal acoustic (LA) and transverse acoustic (TA) phonons at the K-point of the Brillouin zone. This low energy shoulder is enhanced by the curvature of the nanoparticles[18] (Figure 2.10).

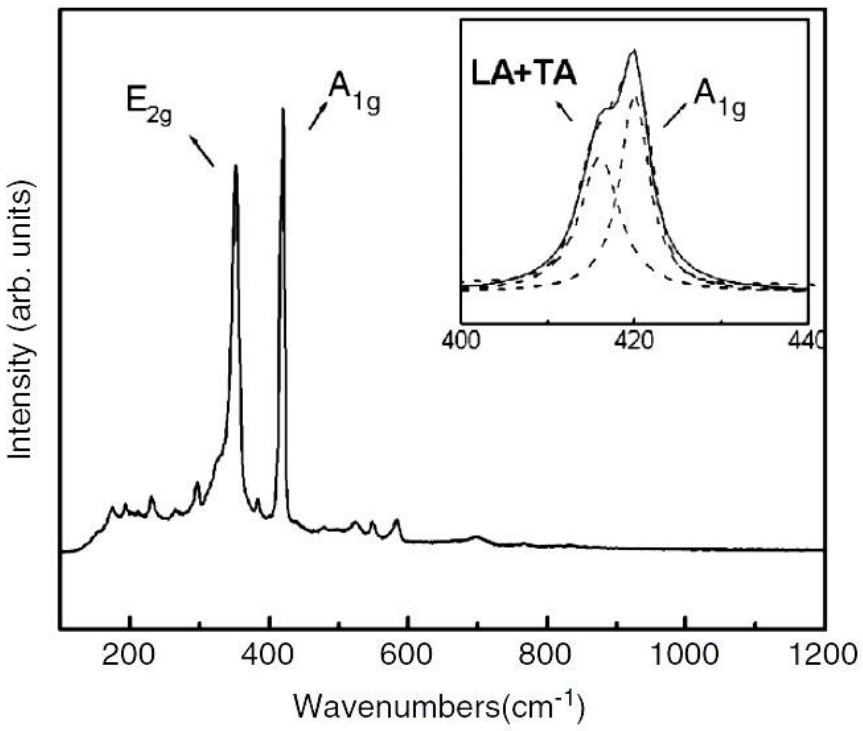

Figure 2.10: The Raman spectrum of an IF-W/WS_2 nanosphere with a core–shell structure at atmospheric pressure[147].

2.2.2. X-ray photoelectron spectroscopy (XPS)

X-ray photoelectron spectroscopy (XPS) is a surface-sensitive quantitative spectroscopic technique that measures the elemental composition at the parts per thousand range, empirical formula, chemical state and electronic state of the elements that exist within a material.

The XPS peaks of reduced GO are assigned to the nonoxygenated C–C and three small C–O components; the C-O (hydroxyl and epoxy), C=O (carbonyl), and C-(O)-O (carboxyl) functional groups. In our previous work on laser-reduction of GO[129], the carbon content bonded to oxygen is reduced from 61% in the initial GO to 16% in reduced GO, indicating that practically all oxygen-containing groups are effectively removed during laser reduction (Figure 2.11).

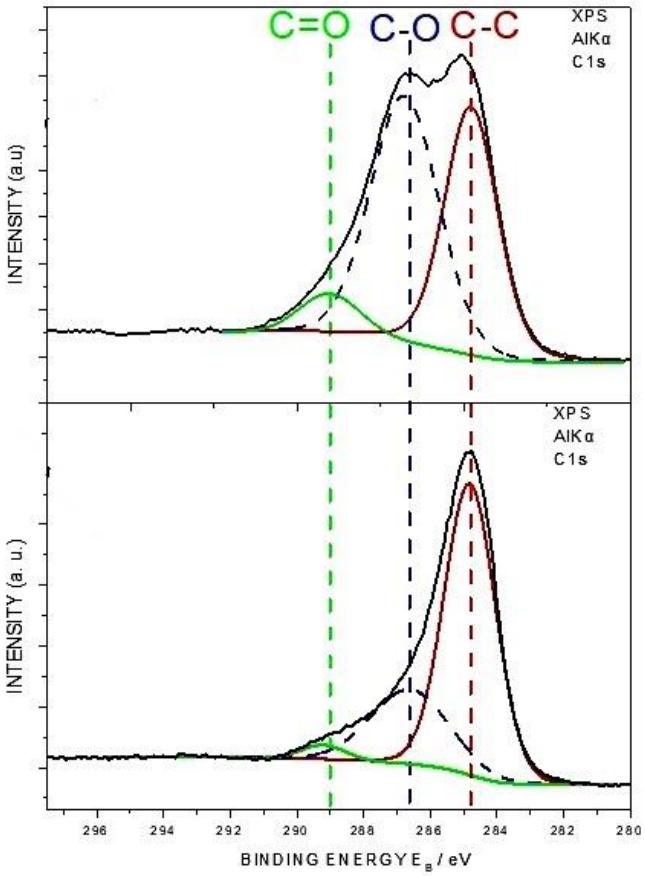

Figure 2.11: XPS spectra on the pristine and laser-reduced GO[129]

2.2.3. X-ray diffraction spectroscopy (XRD)

X-ray diffraction (XRD) is a rapid analytical technique primarily used for phase identification of a crystalline material and can provide information on unit cell dimensions. This technique can be used for measuring the average spacings between layers or rows of atoms, to determine the orientation of a single crystal or grain, to find the crystal structure of an unknown material and to measure the size, shape and internal stress of small crystalline regions.

XRD was used to determine the chemical composition and crystallinity of WS_2 fullerene-like nanoparticles. Li et al, demonstrated that all the reflections of these IFs nanoparticles have been indexed to the hexagonal phase of WS_2 with lattice

constants: a=3.153, c=12.32. The (002) peaks in the Figure 2.12 display a prominent signal indicating the presence of a well-stacked layered structure. A shift in the (002) peak position of IF-WS_2, which is usually regarded as a key mechanism for the strain relief of the folded structure, was also observed[148].

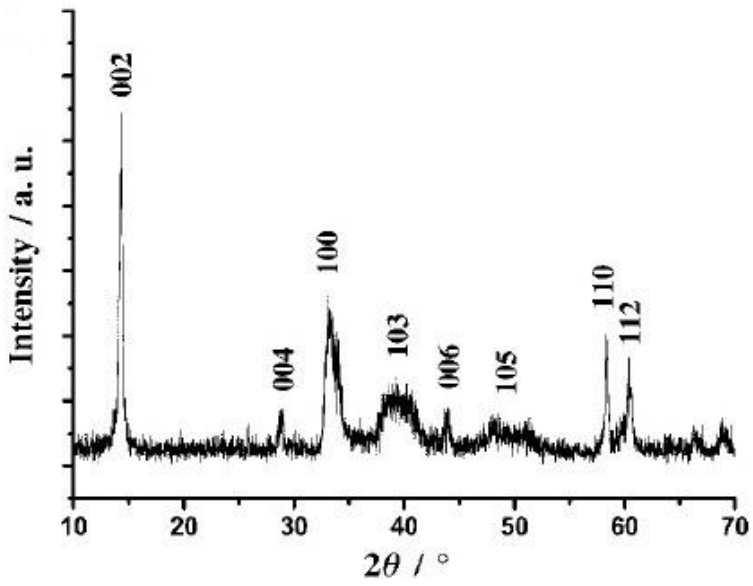

Figure 2.12: XRD pattern of WS_2 fullerene-like nanoparticles[148]

XRD analysis was also performed for WS_2 nanotubes. In particular, Zak et al. presented different reaction states measurements from the gradual conversion of the oxide to sulfide. The result was a pure WS_2 phase with the (002) peak at 14.13^o shifted to lower angles (higher spacing along the c-axis), as compared to the bulk material (14.32^o), due likely to the built-in strain in the nanotube lattice (Figure 2.13) [107].

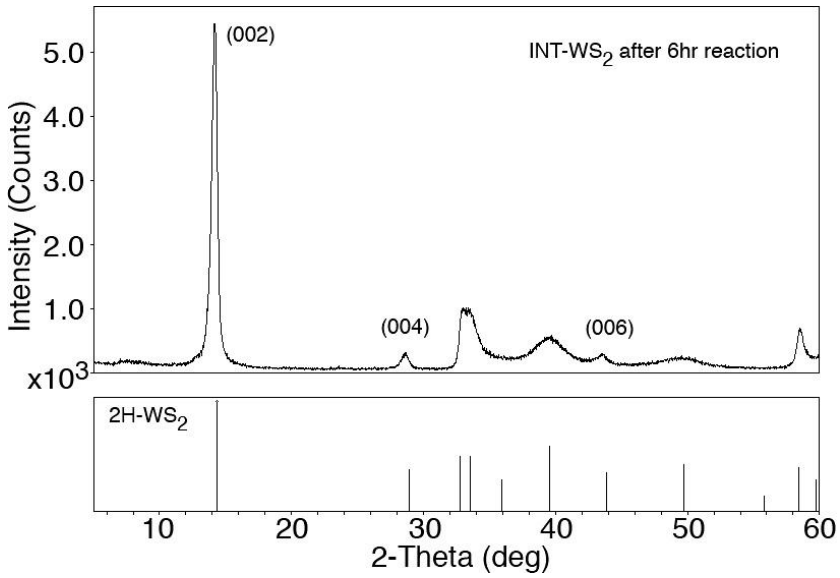

Figure 2.13: XRD pattern of WS_2 nanotubes[107]

Furthermore, Prabakaran et al investigated the different stages of nucleation of WS_2 nano-flowers.. As demonstrated in Figure 2.14 such intermediate phases could be due to the sulphur progressive reaction with the oxide nanoparticles, forming flake like structures on the surface[149].

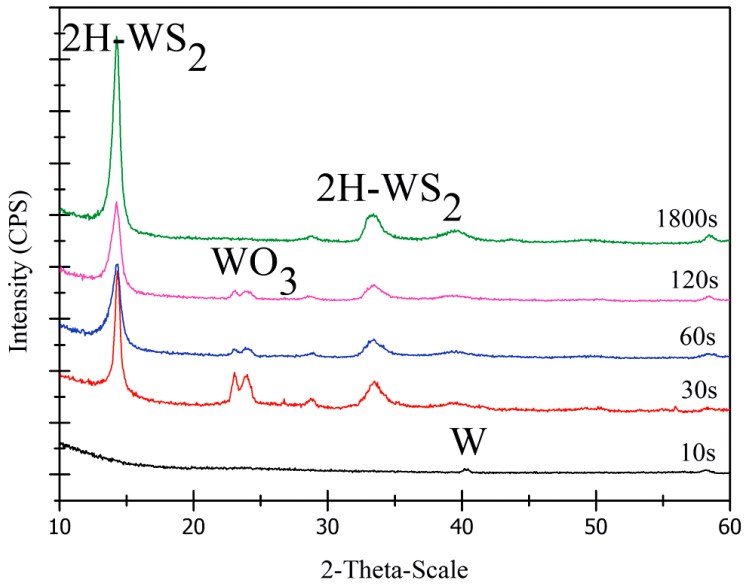

Figure 2.14: XRD pattern of WS_2 nanoflowers and deposits for various time periods from 10 s to 1800 s at 850 ^{0}C.[149]

Chapter III: Laser assisted fabrication of graphene based nanomaterials for opto-electronic devices

3.1. In situ photo-induced chemical doping of solution-processed graphene oxide for electronic applications

We developed a photochemical method for the simultaneous reduction and doping of graphene oxide (GO) layers through ultraviolet laser irradiation in the presence of a dopant precursor gas. It is shown that a few seconds of irradiation is sufficient to dope the GO lattice, while the doping and reduction levels can be readily controlled upon variation of the irradiation time. Using this method, the simultaneous reduction and doping of GO with chlorine or nitrogen atoms is achieved and confirmed by Raman, FTIR and X-ray photoelectron (XPS) spectroscopy measurements. To demonstrate the potential of the approach for practical applications, the photochemical method was successfully employed for the in situ laser induced modification of prefabricated GO field effect transistors. Real time monitoring of the evolution of charge transport as a function of irradiation time reveals significant changes, a result attributed to the chemical modification of the GO lattice. The facile, rapid and room temperature nature of the photoinduced method proposed here provides unique opportunities for the cost-effective synthesis of bulk amounts of chemically modified GO for a wide range of applications spanning from transistors and sensors to transparent electrodes for lighting and photovoltaic cells.

3.1.1. Introduction

Graphene is a 2-dimensional (2D), zero bandgap material with unique morphological, mechanical, optical, thermal and electrical properties[20, 150]. However, the majority of graphene's applications are hindered by the absence of a semiconducting band-gap. As a result, numerous methods have been developed to introduce dopants into the graphene's lattice and in this way to engineer its

bandgap[151,8,152,52,153,154,155,156,157,158]. One alternative method to dope graphene involves the chemical functionalization of the graphene oxide (GO) lattice[159,160,55,161,162,163,164] – a route that could potentially provide access to novel and previously unexplored graphene derivatives. Unfortunately, most of the methods reported to date fail to demonstrate precise control over doping levels and exhibit poor yield or scalability, posing limits for practical applications. In addition, the high temperature processes often required are time-consuming but, more importantly, are not compatible with emerging temperature-sensitive technologies such as large-area plastic/printed electronics. Therefore the development of a simple, low-temperature and high-throughput method for controllable doping of graphene is highly desirable.

Here we report a novel, facile and room temperature methodology that can be used for controllable photochemical doping of GO. GO contains large numbers of functional oxygen groups (e.g. epoxy, hydroxyl, carboxyl, and carbonyl) that could potentially be exploited in order to photo-chemically tune its electrical properties. A successful photochemical event is realized by the light-induced partial removal of such functional groups and the subsequent insertion of hetero-atoms into the GO lattice[165,166]. To date, various laser irradiation approaches have been adopted for GO treatment and are reviewed in ref.[47]37. Of great interest is the laser induced reduction of the GO lattice[50] demonstrated to be suitable for the realization of flexible graphene electrodes[129] and tailoring of the GO band-gap[50]. Moreover lasers had been used for the in situ treatment of GO devices[167]. Finally, a recently published study[168] showed that femtosecond laser irradiation can be used for N doping of GO. Our method relies on precise photochemical reactions initiated by pulsed laser irradiation in the presence of a dopant precursor gas. It is rapid and efficient since a few nanosecond pulses are sufficient to induce doping levels of a few percent. By simple tuning of the laser parameters the exact doping level can be controlled with good reproducibility. The technique negates the need for high temperature post deposition steps and can provide access to the synthesis of large quantities of doped graphene sheets with good control over the doping level, which is not readily realized by existing methods. Using this method, the simultaneous reduction and doping of GO with a few percent of chlorine or nitrogen atoms was realized following irradiation in the presence of Cl_2 or NH_3 gases, respectively. We show that upon photochemical doping chlorine and nitrogen atoms substitute GO defects located on the edges as well as in the plane of the GO lattice[153,157,169]. To demonstrate the applicability of the method for practical device

applications we study the electronic properties of pristine and photo-chemically doped GO layers using field-effect transistor (FET) measurements.

3.1.2. Experimental

GO layer fabrication

Graphite oxide was synthesized by the modified Hummers method and exfoliated to give a brown dispersion of GO under ultrasonication. The resulting GO was negatively charged over a wide pH condition, as the GO sheet had chemical functional groups of carboxylic acids. GO solution in ethanol (0.5 $mgmL^{-1}$) at pH 3.3 was dropped after oxygen plasma treatment for 2 min in order to make the ITO surface hydrophilic. The GO solution was maintained for a waiting period of 2 min and was then spun at 3000 rpm for 30 s, followed by 30 min baking at 100 ^{o}C inside a nitrogen-filled glove box. The thickness of the films was analogous to the number of spinning repetitions; a film thickness of 3.4 nm was obtained with two successive coatings.

Photochemical doping of GO films

The as-spun GO layers on Si or PET substrates were subjected to irradiation by a KrF excimer laser source emitting 20 ns pulses of 248 nm at 1 Hz repetition rate that was translated onto the film area. For uniform exposure of the whole sample to laser radiation, a top-flat beam profile of 20x10 mm^2 was obtained using a beam homogenizer. The whole process took place in a vacuum chamber at 50 Torr Cl_2 or NH_3 gas pressure maintained through a precision micro-valve system. Different combinations of laser powers (P) and the number of pulses (N_p) were tested in an effort to optimize the photochemical functionalization processes. In a typical experiment, the sample was irradiated at a constant P with N_p = 10, 20, 30, 40, 50, 60, 120, 600 and 1200, corresponding to different photochemical reaction times.

Field effect transistor (FET) fabrication

Bottom-gate, bottom-contact FETs were initially prepared using pristine GO sheets. The transistor structures were fabricated using heavily doped p-type Si wafers acting as a common backgate electrode and a 200 nm thermally grown SiO_2 layer as the gate dielectric. Using conventional photolithography, the gold source–drain (S–D)

electrodes were defined with channel lengths and widths in the range 1–40 mm and 1–20 mm, respectively.

Microscopic and spectroscopic characterization

The morphology of the film surfaces was examined by atomic force microscopy (AFM; Digital Instruments NanoScope IIIa). Fourier transform infrared (FTIR) spectra were recorded on a BRUKER FTIR spectrometer IFS 66v/F (MIR). Raman spectroscopy was performed using a Nicolet Almega XR Raman spectrometer (Thermo Scientific) with a 473 nm blue laser as an excitation source. X-ray photoelectron spectroscopy (XPS) measurements were carried out in a Specs LHS-10 Ultrahigh Vacuum (UHV) system. The XPS spectra were recorded at room temperature using unmonochromatized Al Ka radiation under conditions optimized for the maximum signal (constant DE mode with a pass energy of 36 eV giving a full width at half maximum (FWHM) of 0.9 eV for the Au 4f7/2 peak). The analyzed area was an ellipsoid with dimensions 2.5 x 4.5 mm^2. The XPS core level spectra were analyzed using a fittting routine, which allows the decomposition of each spectrum into individual mixed Gaussian–Lorentzian components after a Shirley background subtraction. The ultraviolet photoelectron spectroscopy (UPS) spectra were obtained using HeI irradiation with $h\nu =$ 21.23 eV produced by a UV source (model UVS 10/35). During UPS measurements the analyzer was working at the Constant Retarding Ratio (CRR) mode, with CRR=10. The work function was determined from the UPS spectra by subtracting their width (i.e. the energy difference between the analyzer Fermi level and the high binding energy cutoff), from the HeI excitation energy. For these measurements a bias of 12.30 V was applied to the sample in order to avoid interference of the spectrometer threshold in the UPS spectra. All the work function values obtained by UPS were calibrated using scanning Kelvin probe microscopy (SKPM) measurements. The relative error is 0.02 eV.

3.1.3. Results and discussion

The GO starting material used here was synthesized by a modified Hummers method[170]. The GO water dispersion was then spin coated directly onto silicon or PET[129] substrates.

Figure 3.1 presents the irradiation scheme used for the realization of the doping process. The as-spun GO layers were subjected to irradiation by a KrF excimer laser source emitting 20 ns pulses of 248 nm at 1 Hz repetition rate that was translated onto the film area. For uniform exposure of the whole sample to laser radiation, a top-flat beam profile of 20 x 10 mm^2 was obtained using a beam homogenizer. The whole process took place in a vacuum chamber at 50 Torr Cl_2 or NH_3 gas pressure maintained through a precision micro-valve system. Different combinations of laser powers (P) and the number of pulses (N_p) were tested in an effort to optimize the photochemical functionalization processes. In a typical experiment, the sample was irradiated at a constant P = 25 mW with N_p = 10, 20, 30, 40, 50, 60, 120, 600 and 1200, corresponding to different photochemical reaction times.

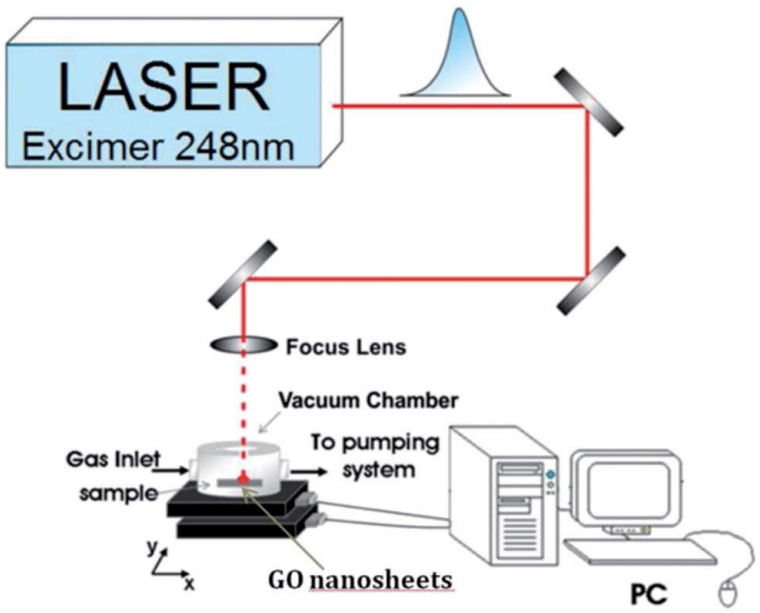

Figure 3.1: Schematic of the experimental set-up used for the laser induced doping of GO nanosheets.

It should be noted here that the results are similar to those obtained upon irradiation with different intensities. Following irradiation, X-ray photoelectron spectroscopy (XPS) was used to probe and quantify the level of dopants introduced into the GO lattice. The respective measurements were carried out using a Kratos Axis Ultra spectrometer with an Al Ka monochromated Xray beam at low pressures. Figure 3.2a compares typical spectra of the pristine and Cl-doped GO. From these data it can be seen that the intensity of the O 1s peak relative to that of C 1s is reduced while the

characteristic Cl2p appears after irradiation. These results indicate laser-induced simultaneous reduction and Cl doping of the GO sheets. The Na peaks visible in the XPS scans are contributions from the sample mounting procedure and can therefore be ignored.

Analysis of the core level characteristic peaks allowed insight to be gained into the nature of the chemical bonds in each case. Figure 3.2b and c present in high resolution the respective C1s and Cl2p peaks showing that, after irradiation, the C–O/C–C intensity ratio decreases from 1.09 to 0.60 while the Cl2p/C 1s intensity ratio becomes equal to 0.17. In particular, the C 1s spectrum of as-prepared GO sheets showed a second peak at higher binding energies, corresponding to large amounts of sp3 carbon with C–O bonds, carbonyls (C=O), and carboxylates (O–C=O)[171], resulted from harsh oxidation and destruction of the sp^2 atomic structure of graphene.

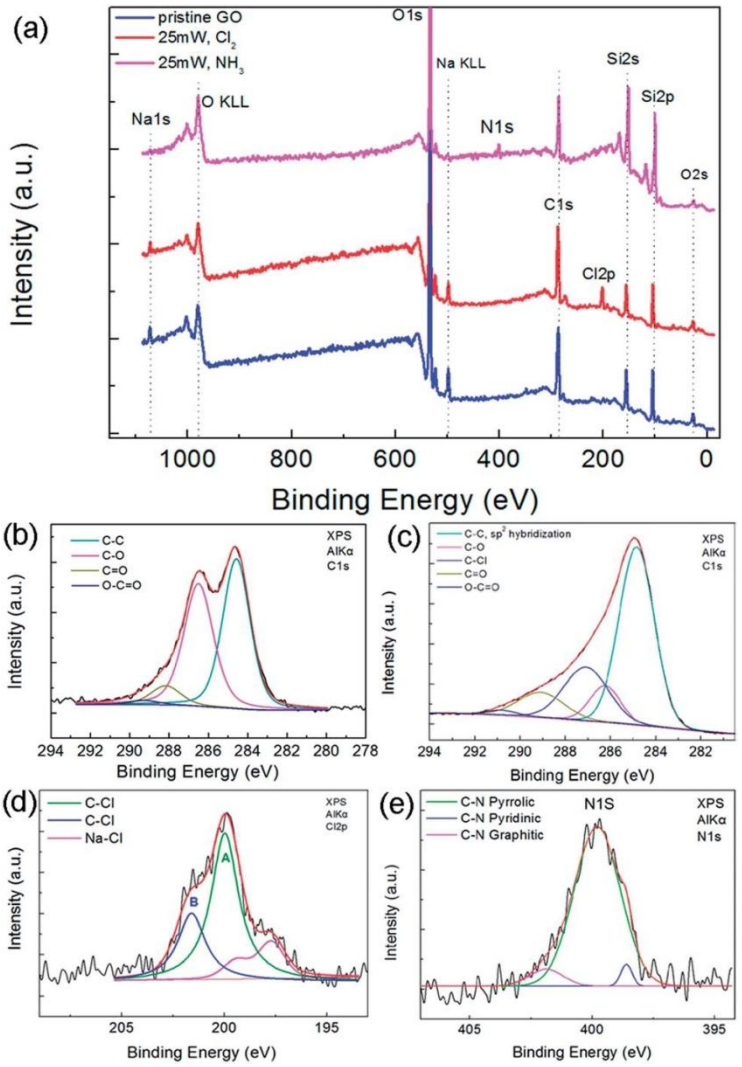

Figure 3.2 (a) XPS survey spectra of pristine and laser treated GO in Cl_2 and NH_3; high-resolution XPS C 1s spectra of GO in its pristine (b) and laser treated in the Cl_2 (c) state; (d) high resolution Cl 2p XPS spectra of GO–Cl layers; high resolution N 1s XPS spectra of GO–N layers.

In our technique, by carefully tuning key laser parameters, the Cl-doping level could be readily controlled. An increase of P in the range from 10 to 50 mW or an increase of N_p at a certain P, gives rise to a corresponding decrease of the doping level. As shown in Figure 3.3a, there is a rapid decrease of the Cl 2p/C ls ratio upon increasing Np while at the same time a sharp increase in the GO reduction degree is evident. The maximum introduction of Cl-groups attained was 11.3 atom% as can be estimated by the ratio of the Cl 2p to the C 1s peak areas after considering the atomic sensitivity factors for Cl 2p and C 1s. We investigated the bonding configurations of Cl atoms in laser treated GO sheets based on high-resolution Cl 2p XPS spectra; a typical example is presented in Figure 3.2d. In all cases, the Cl 2p peaks could be fitted into two peaks, one of lower energy, A ($2p_{3/2}$) and one of higher, B ($2p_{1/2}$). In all the samples, peak A was close to 200 eV and peak B near 201.7 eV corresponding to Cl–C at the edges and Cl–C=O groups, respectively[172]. The above findings indicate the enhancement of the doping efficiency upon increasing the number of the GO oxygen groups, suggesting that Cl-doping most likely occurs at the edges and defect sites[173174].

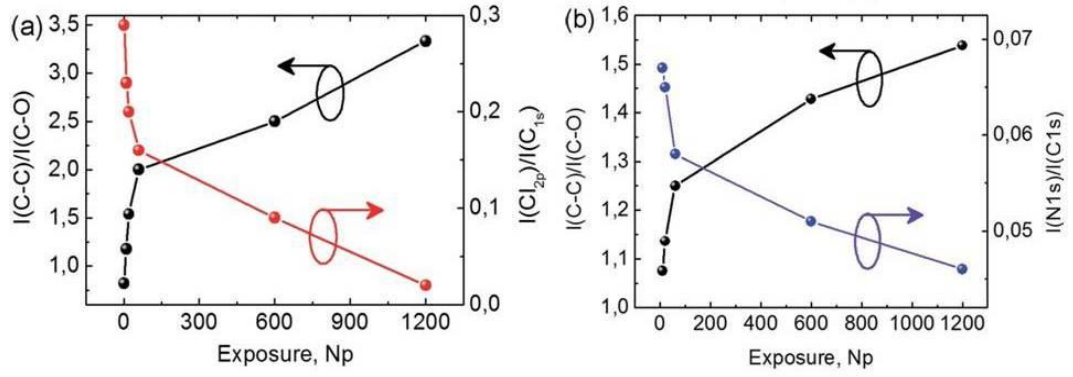

Figure 3.3: a) GO reduction and Cl doping levels as a function of the number of laser pulses, N_p; (b) GO reduction and Cl doping levels as a function of the number of laser pulses, N_p.

Similar results have been acquired using NH_3 gas as a precursor doping agent. The corresponding high resolution N 1S peak in Figure 3.2e depicts that the nitrogen

groups present in the N-doped graphene comprises a pyridinic (at 398.6 eV), a pyrrolic (at 399.8 eV) and a quaternary or graphitic nitrogen (at 401.8 eV) peak[161]. Previous work attributed these contributions to the regions of pyridinic or pyrrolic peaks to the presence of amine groups[55161]. The corresponding dependence of the N-doping level on N_p is presented in Figure 3.3b. As in the case of Cl-doping oxygen groups existing at the edges and defect sites in the plane of GO react with NH_3, giving rise to N-doping, readily detected by XPS spectroscopy. The simultaneous reduction and N-doping of the GO nanolayers treated in NH_3 had been also confirmed via FTIR measurements (Figure 3.4). Following irradiation, the C=O and C–OH vibrational peaks were significantly reduced, while two characteristic new bands appeared at 1030 cm^{-1} and 1650 cm^{-1} due to the C–N bond stretch vibrations[175] and the bending mode of amide bonds[176] respectively.

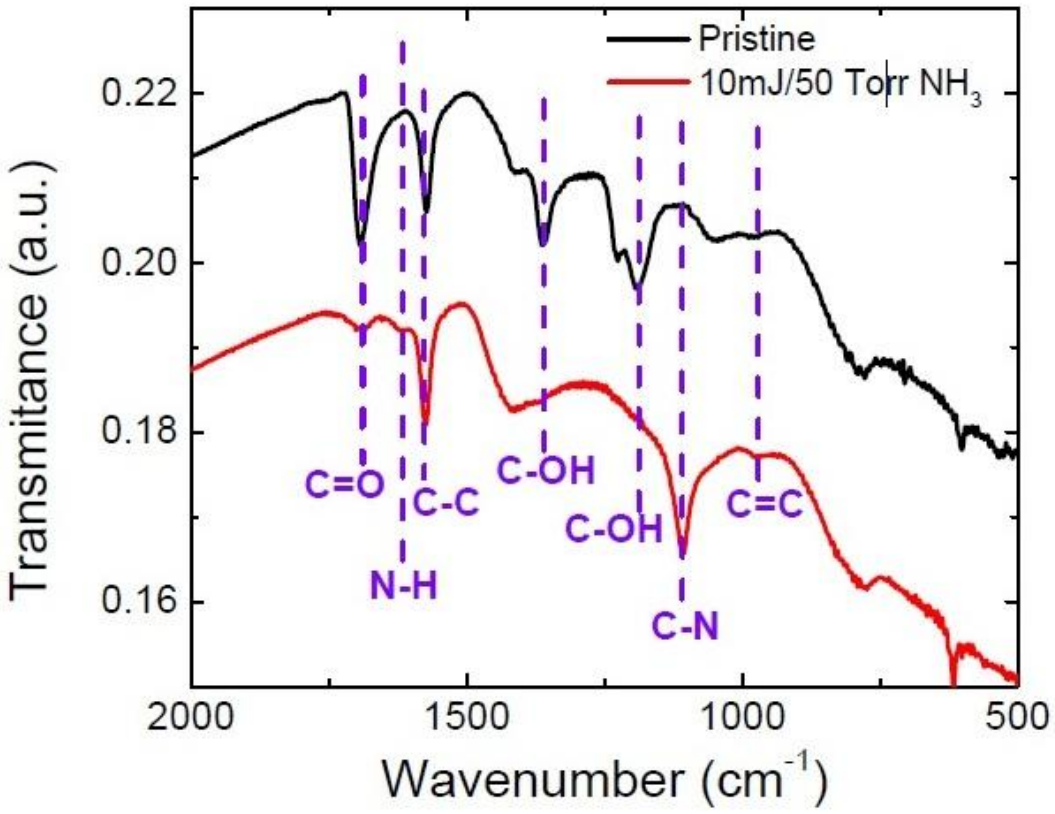

Figure 3.4: FTIR spectra of GO sheets before (pristine) and after irradiation with 10 laser pulses in 50 Torr NH_3

Raman spectroscopy, one of the most sensitive techniques for the investigation of carbon based materials[173], has been also used to investigate the effect of laser

irradiation on the reduction and doping of the GO nanosheets. Figure 3.5a depicts the respective spectra before and after laser irradiation in the presence of Cl_2. All spectra show the two prominent D (at 1330 cm^{-1}) and G (at 1590 cm^{-1}) bands, associated with carbon-based materials, corresponding to the degree of disorder and graphitization respectively[177178]. Also, the presence of a weak 2D band is typical for chemically derived graphene. Although this band was not altered appreciably with the exposure time, the D and G bands were observed to change upon increasing the number of laser pulses, as shown in the inset of Figure 3.5a. In particular, the intensity ratio of the D to G bands (I_D/I_G), which is commonly used as a measure of defect levels in graphene, is seen to progressively increase with exposure time (I_D/I_G ~ 0.88 before laser treatment and 0.95 after laser treatment (Fig. 3.5b)). It had been found that, an increase of the I_D/I_G ratio in GO indicates lattice disordering or ordering depending on the starting defect levels. Based on the measured decrease in channel conductance of the laser-doped GO transistors presented below the increase of the I_D/I_G ratio can be attributed to an increase in defects and disorder in laser treated samples, associated with the decrease in the sp^2-C content as well as the presence of the Cl–C=O form. Furthermore, both peaks gradually shift to higher wavenumbers upon increasing the number of pulses, with the G peak shifting by ~ 10 cm^{-1}, while the D by 4 cm^{-1} (Figure 3.6). The observed blue shift of the G-band position has been attributed to phonon stiffening with doping of GO[179,180]. Moreover, as shown in Figure 3.5c, the G band becomes narrower while at the same time the D band gets broader with increasing exposure time. The D line broadening complies with the I_D/I_G ratio increase and can be attributed to the enhancement of GO reactivity as more defect sites are created[166]. On the other hand, the G band narrowing may be attributed to the doping effect suggesting that covalent bonds, C–Cl bonds, were formed and thus a transformation of the sp^2 type C–C bonds to sp^3 had been induced. The saturation effect observed for I_D/I_G, G and D peak positions and FWHM after illumination with 60 pulses complies with the trend of saturation in the doping efficiency observed in the respective XPS spectra (i.e. compare Figure 3.2 and 3.5). Based on the above XPS and Raman analyses, it can be concluded that the reduction and doping levels can be readily controlled upon increasing the laser exposure time. Most important, XPS measurements reveal that the laser induced dopants are stable for months upon sample storage under ambient conditions.

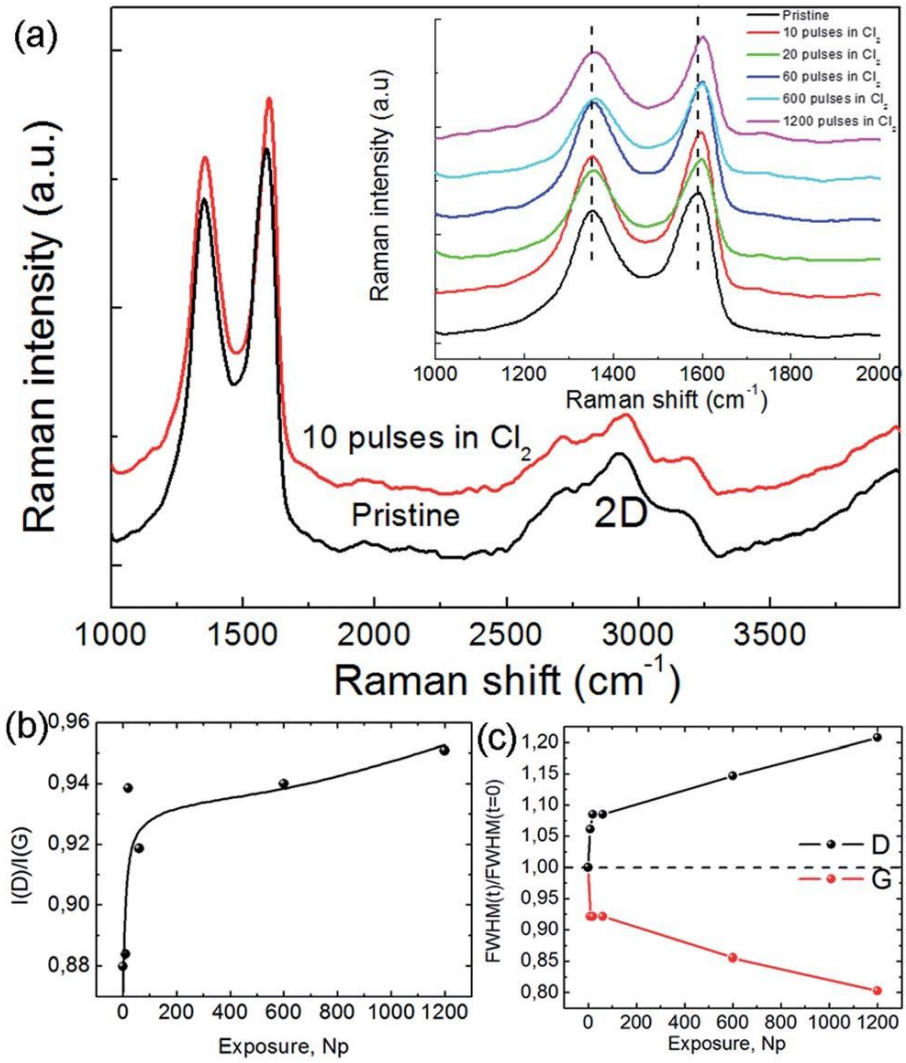

Figure 3.5: (a) Micro-Raman measurements of GO sheets before (pristine) and after irradiation with 10 laser pulses in Cl_2; the evolution of the G and D bands with different numbers of pulses is presented in the inset; (b) dependence of the I_D/I_G ratio on the number of the laser pulses, N_p; (c) dependence of theD and G band's FWHM(normalized values) on N_p.

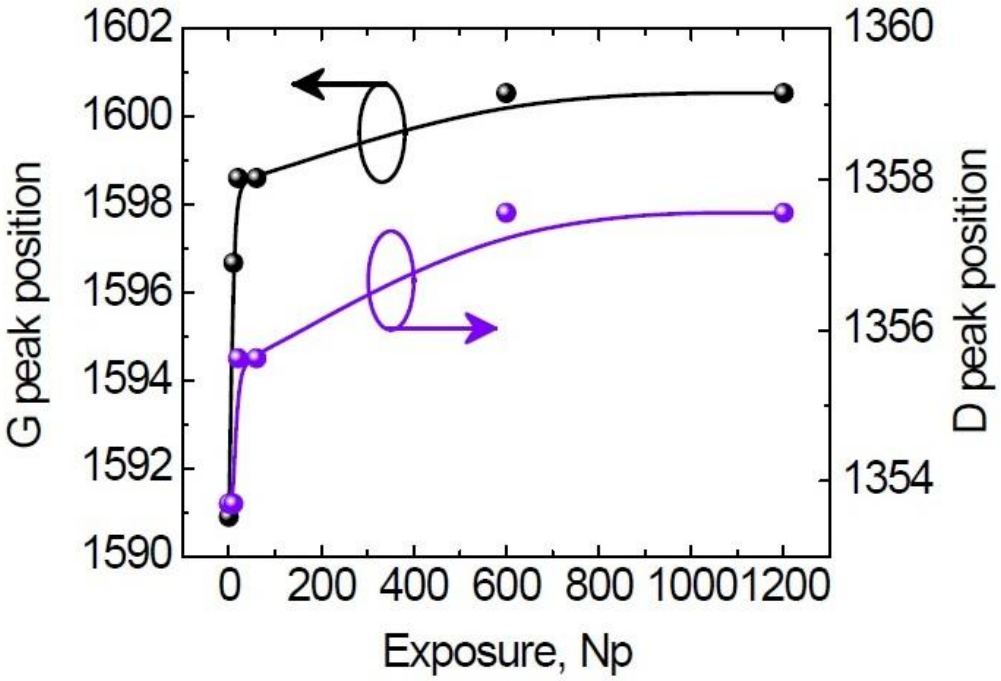

Figure 3.6: Dependence of the D and G bands positions on number of laser pulses, N_p

Concerning the mechanism behind laser-induced doping, it can be postulated that upon excitation with UV laser pulses, chlorine and nitrogen radicals are generated in the gas phase via photodissociation of Cl_2 and NH_3 precursor gases respectively[181]. Subsequently, the radicals formed preferentially react with the GO lattice via, thermodynamically favorable, free radical addition reactions[157,166] . At the same time, electrons generated under irradiation can be captured by GO hence leading to GO reduction[182]. Further investigations are currently in progress to explore and understand the exact mechanism behind the laser-induced doping process.

To investigate how N- and Cl-doping affect the microscopic electronic properties of graphene, bottom-gate, bottom-contact FETs were initially prepared using pristine GO sheets. The transistor structures were fabricated using heavily doped p-type Si wafers acting as a common back-gate electrode and a 200 nm thermally grown SiO_2 layer as the gate dielectric (Figure 3.7a and b). Using conventional photolithography, the gold source–drain (S–D) electrodes were defined with channel lengths and widths in the range 1–40 μm and 1–20 mm, respectively. The GO flakes were deposited by dip-coating at room-temperature directly onto 1.5 cm x 1.5 cm size substrates containing few hundreds of pre-patterned S–D electrode pairs. The samples were then thermally annealed at 200 ^oC in nitrogen. As-prepared

devices were subjected to in situ laser irradiation under identical conditions used for the experiments performed on nanolayers.

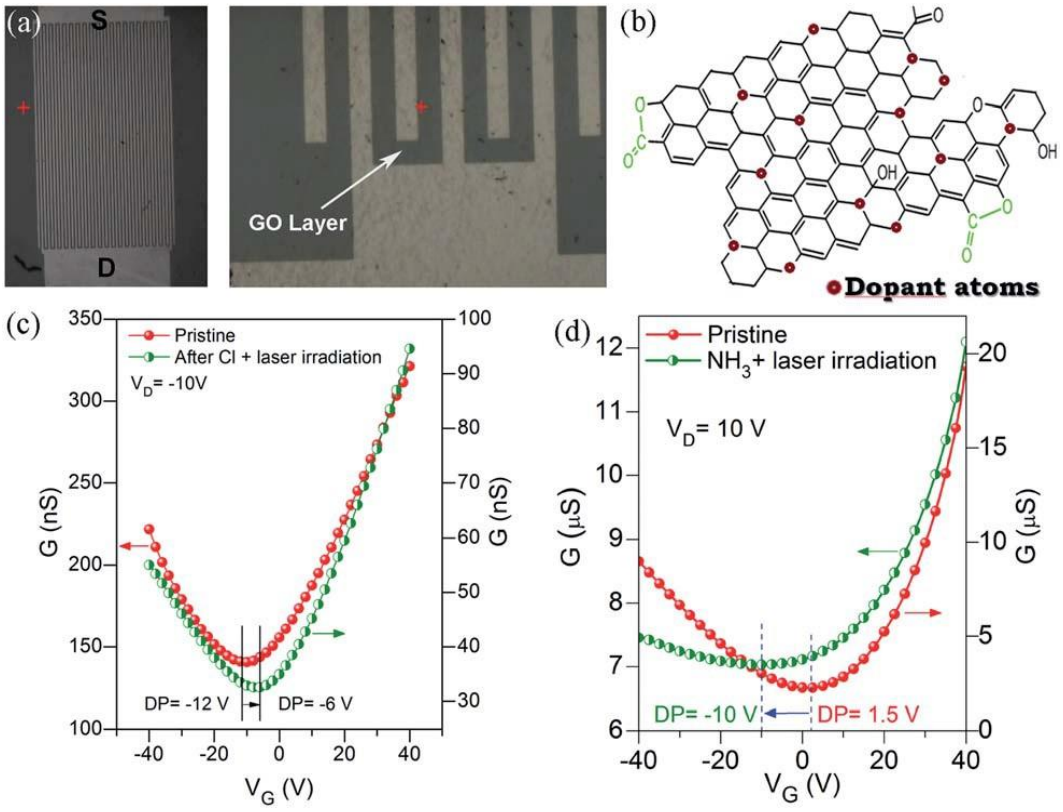

Figure 3.7: (a) Optical microscopy images of GO FETs; (b) schematic representation of reduced and doped GO lattices; (c) transfer characteristics measured for FETs based on rGO before (pristine) and after exposure of the channel to Cl and laser irradiation (Cl_2 + laser irradiation); (e) transfer characteristics measured for FETs based on rGO before (pristine) and after exposure of the channel to NH_3 and laser irradiation (NH_3 + laser irradiation).

Figure 3.7c and d show the channel transconductances (G) versus gate voltage (V_G) characteristics of two GO transistors before and after laser irradiation in the presence of Cl_2 and NH_3 gases, respectively. For the annealed GO devices (pristine) the G–V_G plot shows the typical 'V' shaped ambipolar transfer characteristic with a distinct asymmetry in the electron and hole branches. The charge neutrality point (CNP) for the pristine GO devices was found to vary between 2 V and -12 V. The often measured positive values for the DP indicate unintentional p-doping, probably caused by oxygen species physisorbed on the surface/edges of the GO layers during device preparation[169]. In order to study the impact of laser irradiation in the presence of different dopant gases on the transport properties of GO channels, the transfer

curves for each device were recorded prior to and after laser irradiation with and without the dopant gas presence. To ensure the validity of the changes in the transfer curves following the doping process, the laser treatment was performed in situ in post-fabricated transistors. In a typical experiment the pristine transfer curve of a transistor based on undoped GO was recorded followed by laser treatment in the presence of the dopant precursor gas. Afterwards, the new transfer curve was measured and compared to that obtained in the pristine state. In the time periods among the measurements, the transistor was kept in an inert atmosphere in order to avoid unintentional doping due to physisorbed atoms and molecules.

Laser treatment in the presence Cl_2 gas leads to a drop in the overall channel conductance under both p- and n-channel operation. The clear shift in the CNP to more positive voltages is most likely the result of the enhanced p-type conductivity of the GO channel due to the photochemically induced p-type doping of GO[153,183]. This observation is in qualitative agreement with the shift in the work function (WF) of the GO layer from 4.91 eV to 5.23 eV measured before and after laser irradiation, respectively (Figure 3.8a). Laser irradiation of the control samples under an inert atmosphere is found to have no distinguishable impact on the transporting characteristics of the device (Figure 3.8b). Based on these results we conclude that the observed changes in the channel conductance can only be attributed to p-doping caused primarily by laser induced photo-reaction with the dopant gas (Cl_2).

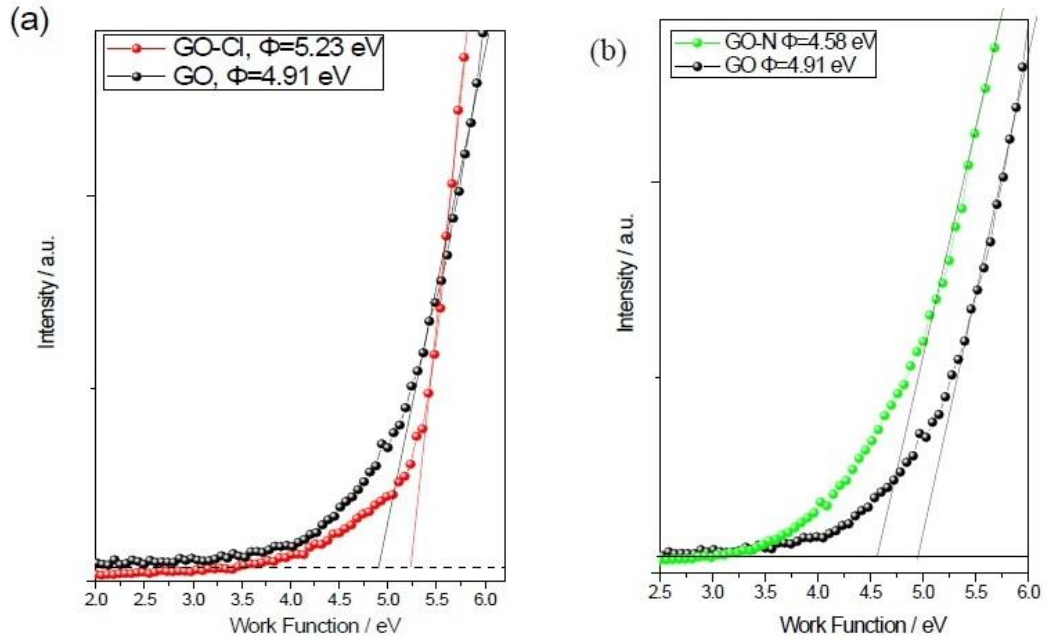

Figure 3.8: UPS spectra of GO films before (pristine) and after irradiation with 10 laser pulses in 50 Torr Cl_2(a) and NH_3 (b).

When the GO channel was irradiated with laser light in the presence of NH_3 (Figure 3.7d), the device characteristics exhibit the opposite trend to that seen in transistors irradiated in the presence of Cl_2 gas (Figure 3.7c). In particular, the CNP is found to shift to more negative gate voltages indicative of n-type doping[184]. This observation is in good agreement with the measured shift in the WF function from 4.91 eV for the pristine GO to 4.6 eV for laser irradiated GO in the presence of NH_3 (Figure 3.8b). Table 3.1 summarizes the respective on/off ratios and mobility values for GO transistors treated in Cl_2 and NH_3 respectively. It is clear that the photochemical process is rapid, since a few nanosecond pulses in the presence of a reactive dopant gas are sufficient to induce up to a five-fold increase of the channel on/off ratio[155]. In contrast to the WF changes described above, the relatively small change of the on/off ratio indicates a minor electronic effect due to dopant atoms.

Table 3.1: Carrier mobilities and on/off ratios of GO transistors subjected to laser treatment in Cl_2 and NH_3 respectively

	μ_{Iin} [$cm^2V^{-1}s^{-1}$		I_{ON}/I_{OFF}	
Sample	Before irradiation	After irradiation	Before irradiation	After irradiation
Laser treated in NH_3 50 mJ, 10 pulses)	3.10×10^{-3}	9.83×10^{-4}	2.25	8.91
Laser treated in Cl_2 (50 mJ, 10 pulses)	16.3×10^{-3}	3.81×10^{-3}	1.53	3.61

The general decrease in GO conductivity (holes and electrons) observed upon photochemical doping suggests an increase in the structural disorder, which is in agreement with the Raman measurements presented above. Such lattice disorder

could be caused either by interruption of the conjugated system or the introduction of scattering centers[185,156]. The decrease in both electron and hole mobilities together with the G-band narrowing is the indication that the laser induced photochemical reaction(s) gives rise to substitutional doping at the expense of surface charge transfer doping[155]. This observation is in contrast to the increase in carrier mobility and improvement in the lattice order observed upon laser treatment of GO under an inert atmosphere[167]. The present results confirm that laser irradiation of GO under an inert atmosphere does not induce any structural disorder and the presence of reactive dopant gas(es) combined with laser irradiation is the main reason for the observed doping effects.

3.1.4. Conclusions

Based on the results presented here it can be concluded that laser irradiation in the presence of a reactive gas can be used as an easy and catalyst-free approach for the synthesis of doped GO derivatives. The proposed method is simple and provides access to controllable reduction and doping of GO at room temperature hence allowing the combination of the technique with temperature sensitive substrate materials such as plastic. The rather simple and scalable method could potentially be used for the synthesis of novel graphene-based derivatives that are difficult or impossible to obtain via conventional synthetic routes.

3.2. Improving the efficiency of organic photovoltaics by tuning the work function of graphene oxide hole transporting layers

A facile, fast, non-destructive and roll-to-roll compatible photochemical method for simultaneous partial reduction and doping of graphene oxide (GO) films through ultraviolet laser irradiation in the presence of a Cl_2 precursor gas is demonstrated. The photochemical chlorinated GO–Cl films were fully characterized by XPS and Raman measurements, in which grafting of chloride to the edges and the basal plane of GO was confirmed. By tuning the laser exposure time, it is possible to control the doping and reduction levels and therefore to tailor the work function (WF) of the GO–Cl layers from 4.9 eV to a maximum value of 5.23 eV. These WF values match with the HOMO level of most polymer donors employed in OPV devices. Furthermore, high efficiency poly(2,7-carbazole) derivative (PCDTBT):fullerene derivative ($PC_{71}BM$) based OPVs with GO–Cl as the hole transporting layer (HTL) were demonstrated with a power conversion efficiency (PCE) of 6.56% which is 17.35% and 19.48% higher than that of the pristine GO and PEDOT:PSS based OPV devices, respectively. The performance enhancement was attributed to more efficient hole transportation due to the energy level matching between the GO–Cl and the polymer donor.

3.2.1. Introduction

Organic photovoltaic (OPV) devices utilizing polymer–fullerene bulk heterojunctions (BHJs) have been widely studied due to their promising advantages over their traditional inorganic Si based counter-parts, including low cost fabrication on light weight, large area and flexible substrates and the use of roll-to-roll (R2R) mass production techniques[186,187,188,189,190] . Recently, the research effort has been focused to the interface engineering of OPVs and especially to the introduction of buffer layers with electron blocking properties between the BHJ active layer and the transparent ITO electrode, in order to reduce recombination and leakage of current at the photoactive layer–electrode interface[191,192,193].

The highly doped poly(3,4-ethylenedioxythiophene):poly-(styrene sulfonate) (PEDOT:PSS) is the most regularly used a hole transporting layer (HTL) material for organic BHJ solar cells, because of its solution process ability, high work function, sufficient conductivity, and high optical transparency in the visible-NIR regime[194]. However, there are several drawback issues leading to OPV failure, which are directly related to PEDOT:PSS. The acidic and hygroscopic nature of PEDOT:PSS corrodes both the ITO electrode[195,196] and the processing equipment[197] at elevated temperatures, and can introduce water into the active layer, degrading the performance and long-term stability of the OPV device[198,199]. In addition, the strong anisotropy in the conductivity of the spin coated PEDOT:PSS films originating from their lamellar structure leads to inhomogeneous charge extraction in some locations and dead spots in others[200,201]. To overcome these drawbacks, several types of materials have been explored to serve as HTLs in BHJ solar cells, mainly focusing on metal oxide inorganic semiconductors[202,203,193,204,205]. However, the oxides are deposited using cost-intensive high vacuum techniques that are incompatible with low-cost solution-processable and r2r large area manufacturing of OPVs. So, it is obvious that the development of low cost and simply processable HTL materials compatible with OPV materials and r2r techniques is urgently demanded.

In this context, solution processable carbon nanotubes[206] and graphene based materials[207] were used as the HTL. In particular, spin coated graphene oxide (GO) derivatives have been studied as promising alternatives to PEDOT:PSS, due to their optical transparency, mechanical flexibility and compatibility with R2R production[208,188,209,210]. GO is a graphene sheet modified with oxygen functional groups in the form of epoxy and hydroxyl groups on the basal plane and various other types, such as carboxylic acid groups at the edges[211]. It can be produced by exfoliation of inexpensive graphite powders with strong oxidizing reagents[33]. The availability of reactive groups on both the basal plane and the GO sheets enables the manipulation of the size, shape and relative fraction of the sp2 hybridized domains of GO, allowing the tailoring of its optoelectronic properties[11,212,58].

However, the obtained performances are only comparable with the PEDOT:PSS based devices and not superior as would be expected due to the GO film higher transparency across the whole visible spectrum. The main barrier to higher performance enhancement is the work function (WF) of the asprepared GO film. The measured WFs are in the range of 4.7–4.9 eV[213,214] and do not match with the highest

occupied molecular orbital (HOMO) of the most commonly used electron donor materials in the state of the art BHJ OPV devices, as in the PEDOT:PSS case (>5.1 eV)[215]. Therefore, tuning of the GO WF with the polymer HOMO is needed. In this pathway, oxygen plasma treated and sulfated GO with increased WFs of 4.8 and 5.2 eV, respectively, were successfully utilized as the HTLs in OPVs[216,217]. Moreover, we recently demonstrated that spin coated GO films can be in situ non-thermal reduced by femtosecond pulsed laser beam irradiation[129].

In this work, a novel approach of WF tuning of GO HTLs is demonstrated, based on laser-induced doping of GO. In particular, pulsed laser irradiation of ultrathin GO films in the presence of a dopant chloride (Cl_2) precursor gas was employed for the simultaneous reduction and doping of GO. It is shown that the laser induced chloride atoms substitute the GO defects into both the edges and in the plane of the GO lattice[157]. In this way, the work function of irradiated layers can be tuned as a function of the laser exposure time. This process leads to a significant increase of the photocurrent and hence of the OPV device performance mainly due to an increase in the hole mobility of the respective devices.

3.2.2. Experimental

GO film fabrication

Graphite oxide was synthesized by the modified Hummers method and exfoliated to give a brown dispersion of GO under ultrasonication[218]. The resulting GO was negatively charged over a wide range of pH conditions, as the GO sheet had chemical functional groups of carboxylic acids. GO solution in ethanol (0.5 mg ml^{-1}) at pH 3.3 was dropped after an oxygen plasma treatment for 2 min in order to make the ITO surface hydrophilic. The GO solution was maintained for a waiting period of 2 min and was then spun at 3000 rpm for 30 s, followed by 30 min baking at 100 ^{o}C inside a nitrogen-filled glove box. The thickness of the films was analogous to the number of spinning repetitions; a film thickness of 3.4 nm was obtained with two successive coatings.

Photochemical doping and reduction of GO films

The as-spun GO layers on ITO/glass substrates were subjected to irradiation by a KrF excimer laser source emitting 20 ns pulses of 248 nm at a 1 Hz repetition rate that was

translated onto the film area. For uniform exposure of the whole sample to laser radiation, a top-flat beam profile of 20 x 10 mm^2 was obtained using a beam homogenizer. The whole process took place into a vacuum chamber at 50 Torr Cl_2 gas pressure maintained through a precision micro valve system. Different combinations of laser powers (P) and the number of pulses (N_P) were tested in an effort to optimize the photochemical functionalization processes. In a typical experiment, the sample was irradiated at a constant P with N_P = 10, 20, 30, 40, 50, 60, 120, 600 and 1200, corresponding to different photochemical reaction times.

Device fabrication

The photovoltaic devices reported were fabricated on 15 mm by 15 mm indium-tin-oxide (ITO) glass substrates with a sheet resistance of 15 Ω sq^{-1}. The impurities are removed from the ITO glass through a 3-step cleaning process. GO with different thicknesses were spin casted as described previously. Next, a photoactive layer consisting of a P3HT:PCBM (1 : 1 wt% ratio, 220 nm thick) or a PCDTBT:PC_{71}BM (1 : 4 wt% ratio, 80 nm thick) blend was spin coated on the HTL from a dichlorobenzene (o-DCB) or 1 : 4 ratio dichlorobenzene : chlorobenzene solution, respectively, at 1000 rpm. Both solutions were stirred for at least 72 hours at 80 C before use. The P3HT-PCBM devices were then post-annealed at 160 ^oC for 15 min in a glove box under a nitrogen atmosphere. For the PCDTBT:PC_{71}BM devices, a TiO_x electron transporting interlayer was dissolved in methanol (1 : 200) and then spin coated to a thickness of approximately 10 nm (6000 rpm, 40 s). Finally, a 100 nm thick Al layer was deposited by thermal evaporation through a shadow mask to define an active area of 6 mm^2. Devices were encapsulated for testing in air with a UV-curable epoxy and covered with a glass slide and were fixed on top of an aperture having exactly the same dimensions as the active area (overlap of ITO and Al electrodes) during all measurements.

Microscopic and spectroscopic characterization

The UV-VIS absorption spectra of the samples were recorded using a Shimadzu UV-2401 PC spectrophotometer over the wavelength range of 400–1000 nm. The morphology of the surfaces was examined by field emission scanning electron microscopy (FE-SEM; JEOL JSM-7000F) and by atomic force microscopy (AFM; Digital Instruments NanoScope IIIa). X-ray photoelectron spectroscopy (XPS)

measurements were carried out using a Specs LHS-10 Ultrahigh Vacuum (UHV) system. The XPS spectra were recorded at room temperature using unmonochromatized AlKa radiation under conditions optimized for the maximum signal (constant DE mode with a pass energy of 36 eV giving a full width at half maximum (FWHM) of 0.9 eV for the Au $4f_{7/2}$ peak). The analyzed area was an ellipsoid with dimensions 2.5 x 4.5 mm^2. The XPS core level spectra were analyzed using a fitting routine, which allows the decomposition of each spectrum into individual mixed Gaussian–Lorentzian components after a Shirley background subtraction. The ultraviolet photoelectron spectroscopy (UPS) spectra were obtained using HeI irradiation with $h\nu$ = 21.23 eV produced by a UV source (model UVS 10/35). During UPS measurements the analyser was working at the Constant Retarding Ratio (CRR) mode, with CRR = 10. The work function was determined from the UPS spectra by subtracting their width (i.e. the energy difference between the analyzer Fermi level and the high binding energy cutoff), from the HeI excitation energy. For these measurements a bias of -12.30 V was applied to the sample in order to avoid interference of the spectrometer threshold in the UPS spectra. All the work function values obtained by UPS were calibrated with scanning Kelvin probe microscopy (SKPM) measurements. The relative error is 0.02 eV.

Device parameters

Current–voltage (I–V) measurements were performed at room temperature using an Agilent B1500A Semiconductor Device Analyzer. For photovoltaic characterization the devices were illuminated with a 100 mW cm^{-2} power intensity of white light using an Oriel solar simulator with an AM1.5 filter through the glass/ITO side. A reference monocrystalline silicon solar cell from Newport was used to calibrate the lamp. X-ray photoelectron spectroscopy (XPS) was used to probe and quantify the level of dopants introduced into the GO lattice.

3.2.3. Results and discussion

Characterization of photochlorinated GO films

The photochlorinated GO (GO–Cl) was investigated by XPS, UPS, and atomic force microscopy (AFM). Figure 3.9 compares typical XPS spectra of the pristine GO and GO–Cl films. It can be clearly seen that the intensity of the O 1s peak relative to that of C 1s is reduced while the characteristic Cl 2p, due to chloride bonds, appears after the photochlorination process. The XPS results clearly indicate that simultaneous photoreduction and Cl doping of the GO nanosheets takes place.

Figure 3.9b shows in high-resolution the respective C 1s peaks of GO and GO–Cl, consisting of three kinds of components assigned to C–O (hydroxyl and epoxy), C=O (carbonyl), and C–(O)–O (carboxyl) functional groups.20 Upon photochlorination, the C–O/C–C intensity ratio decreases from 1.09 to 0.60 while the Cl 2p/C 1s intensity ratio becomes equal to 0.17. In particular, the C 1s spectrum of the as-prepared GO sheets shows an additional peak at higher binding energies, corresponding to large amounts of sp3 carbon with C–O bonds, carbonyls (C=O), and carboxylates (O–C=O)[171].

Figure 3.9c shows the high-resolution Cl 2p spectra of the GO–Cl film, confirming the Cl_2 doping in the GO lattice. The Cl 2p spectra can be fitted into two nonequivalent chlorine sites from the (A) 3/2 and (B) 1/2 levels. The more intense peak A was close to 200 eV corresponding to Cl–C covalent bonds at the edges, while the less intense peak B at 201.7 eV corresponds to the Cl–C=O groups[172]. The above findings indicate enhancement of the doping efficiency upon increasing the number of the GO oxygen groups, suggesting that Cl-doping most likely occurs at the edges and defect sites[173,174].

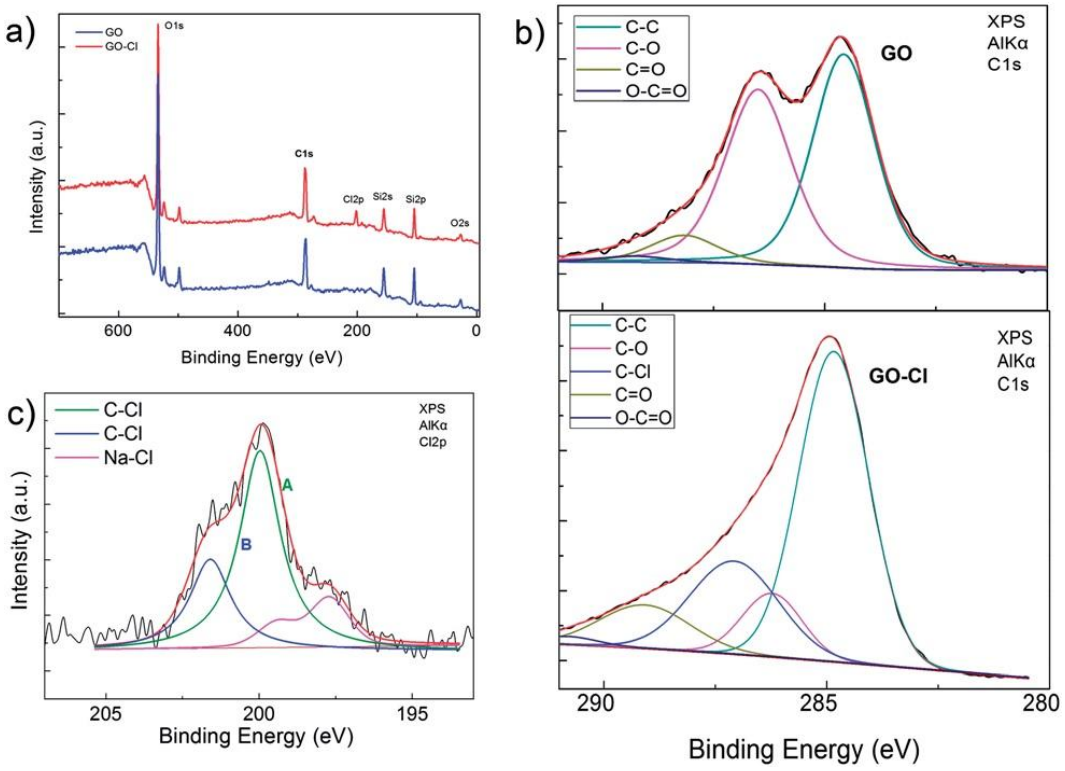

Figure 3.9: (a) XPS survey spectra and (b) high-resolution XPS C 1s spectra and (c) high-resolution Cl 2p XPS spectra of GO and GO–Cl films.

Tuning of the laser source key parameters can lead to respective tuning of the Cl_2 doping level of the GO. In particular, this can take place upon increasing the laser power (P) in the range from 10 to 50 mW or increase of the number of pulsed (N_P) at a certain P, giving rise to a corresponding decrease of the doping level. Figure 3.10a shows that the I(C–C)/I(C–O) ratio, which corresponds to the GO reduction degree, increases upon increasing the N_P, while the I(Cl 2p)/I(C 1s) ratio, which corresponds to Cl_2 doping, decreases. The maximum introduction of Cl-groups attained was 11.3 atom% as can be estimated by the ratio of the Cl 2p to the C 1s peak areas after considering the atomic sensitivity factors for Cl 2p and C 1s.

The work function of the respective GO–Cl layers determined by ultraviolet photoelectron spectroscopy (UPS) and scanning Kelvin probe microscopy (SKPM) for N_P values of 1–60 are shown in Figure 3.10b. It was observed that the WF rises with increased exposure, and tends to saturate at 5.23 eV for N_P = 60. As can be seen in the respective UPS spectra shown in Figure 3.10c, this value is much higher than the respective WFs measured for GO (4.9 eV). The maximum WF is obtained at the

point, at which both the reduction and the doping rates start to significantly increase and decrease, respectively. Therefore, as can also be seen from the inset shown in Figure 3.7b, the WF increase is most likely due to a synergetic effect of the chloride doping and the partial reduction processes.

It is evident that laser radiation causes partial reduction of the GO sheets while at the same time chlorine molecules split into highly reactive radicals and react with the GO lattice via a free radical addition reaction. Under these conditions, tuning of the GO WF can be achieved by the formation of surface $C^{\delta+}$-$Cl^{\delta-}$ dipoles with different electronegativities (2.55 for C compared to 3.16 for Cl).

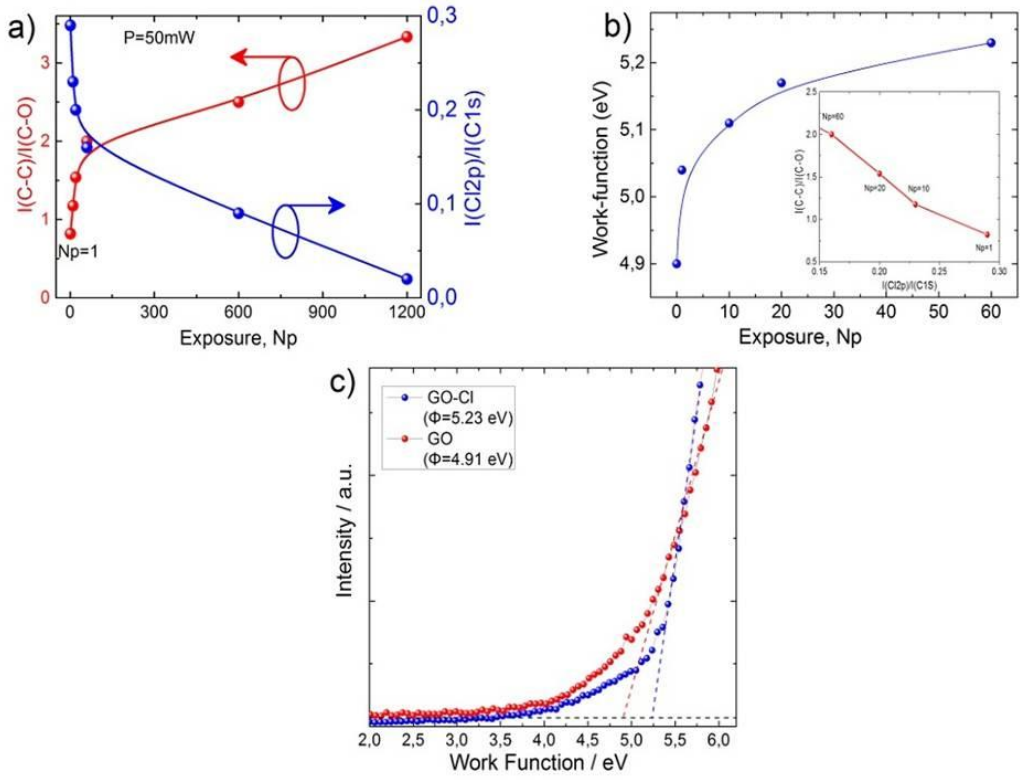

Figure 3.10: (a) GO reduction and doping levels as a function of N_P and (b) the work function of GO–Cl films as a function of the N_P exposure. The inset shows the dependence of Cl 2p doping (I(Cl 2p)/I(C 1S)) with the reduction degree ((I(C–C)/I(C–O)) (c) UPS spectra of the GO and GO–Cl (N_P = 60) films).

As shown in Figure 3.11a, such dipoles can be formed by chlorine atoms in Cl–C covalent bonds at the edges and/or Cl–C=O groups located outside the graphene

basal plane[219,220]. The induced polar character of C–Cl bonds is responsible for the downward shift of the Fermi level in the valence band of GO–Cl, and the subsequent increase in the work function from 4.9 eV in GO to 5.23 eV in GO–Cl (Figure 3.11b)[220,221]. In addition, the charge rearrangement by the electron drawing towards chlorine atoms, increase the number of hole charge carriers in the conjugated sp^2 network of GO–Cl, enhancing its p-type behavior[222]. Therefore, the strength of the out of plane dipole moment in the GO, and thus the WF can be tuned by (a) the variation of the overall oxygen content, realized by partial reduction and (b) the replacement of oxygen atoms with chloride ones with higher electronegativity upon doping.

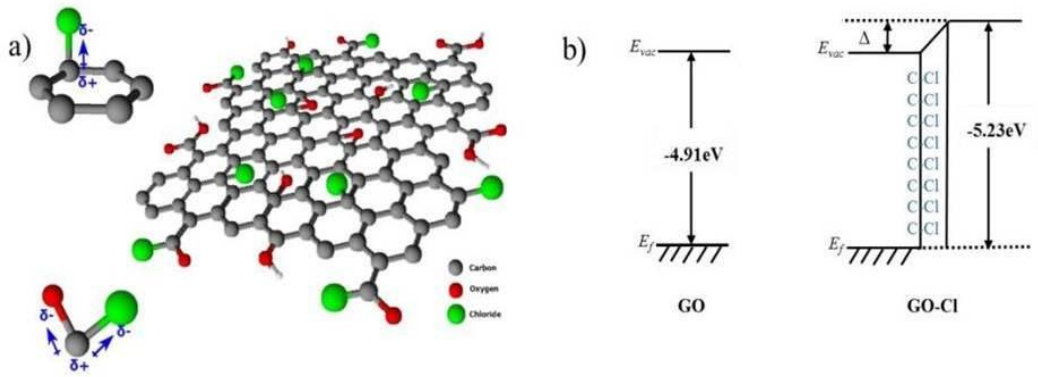

Figure 3.11: a) 3D chemical structure of the photochlorinated GO, illustrating the formation of dipoles by chlorine atoms in Cl–C covalent bonds at the edges and/or Cl–C=O groups located outside the graphene basal plane. (b) Schematic energy level diagram showing the effect of polar C–Cl bonds on the work function.

Photovoltaic characteristics

To explore the effects of the photochlorination of the GO layer on device performance, OPVs with the conventional device structure glass/indium tin oxide (ITO)/HTL/polymer:$PC_{71}BM$/ TiO_x/Al were fabricated. The HTL layers compared were PEDOT:PSS, GO and GO–Cl. The device structure and the energy level diagrams of the different materials used in the fabrication are shown in Figure 3.12a and b.

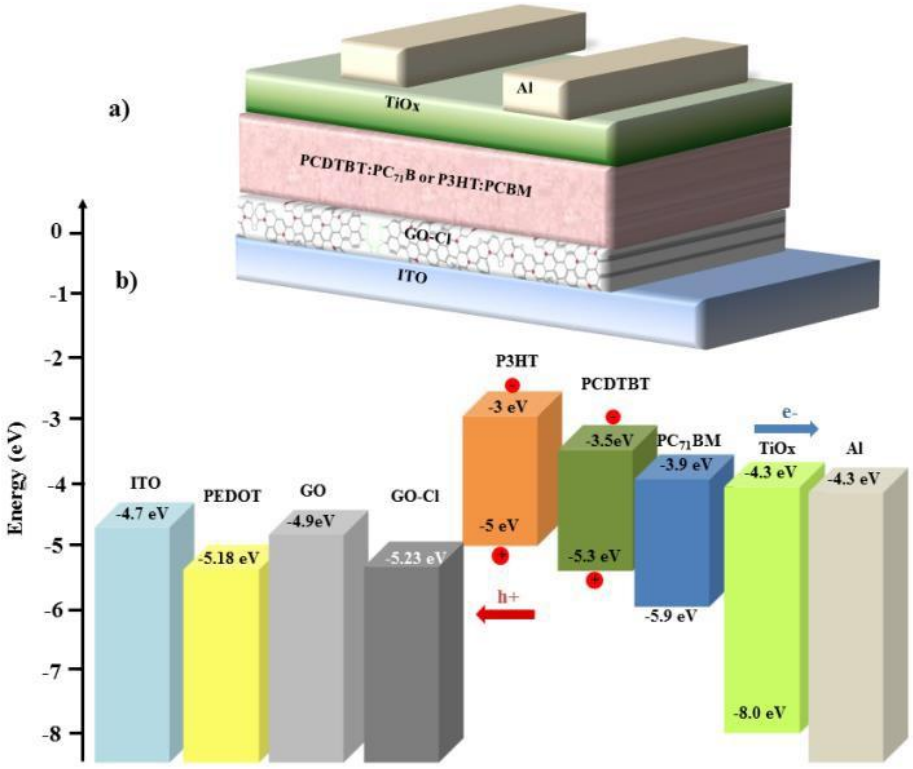

Figure 3.12: (a) Schematic illustration of the BHJ OPV device with the GO– Cl HTL and (b) the energy level diagram depicting the relevant energy levels under flat band conditions of all materials used in the OPV cells studied and not the actual interfaces.

Before analyzing the photovoltaic characteristics, it is important to describe the functionality of the HTL during the device operation. The solar light irradiates the photoactive layer through the HTL/ITO electrode side, while the active layer absorbs photons to produce excitons. The photo-excited excitons dissociate at the polymer–fullerene interface into electrons in the lowest unoccupied molecular orbital (LUMO) of the fullerene acceptor, and holes in the highest occupied molecular orbital (HOMO) of the polymer donor. Therefore, the HOMO level of the polymer donor should be ideally equal to the WF of the HTL, so that the holes can be readily transported to the ITO electrode through the HTL. In this context, two different polymer donors (a) P3HT with a HOMO of 5 eV and (b) PCDTBT with a HOMO of 5.3 eV were utilized, in order to examine the influence of the GO–Cl HTL WF on the photovoltaic characteristics. Reference devices incorporating PEDOT:PSS and pristine GO as the HTL were also fabricated for comparison. It should be noted that

the optimum thickness of the GO film is found to be around 3.4 nm for both GO and GO–Cl HTLs. This finding is in disparity with the first report of GO based HTLs, where the GO thin films with a thickness of 2 nm gave the highest efficiency[208], but in agreement with our previous studies[206] and recent studies of plasma treated GO HTLs, in which the same spinning conditions of the GO films, resulted in 1 and 3 nm thin films on mica and ITO substrates, respectively[216]. This effect may also be caused by the different lateral dimensions of GO flakes employed.

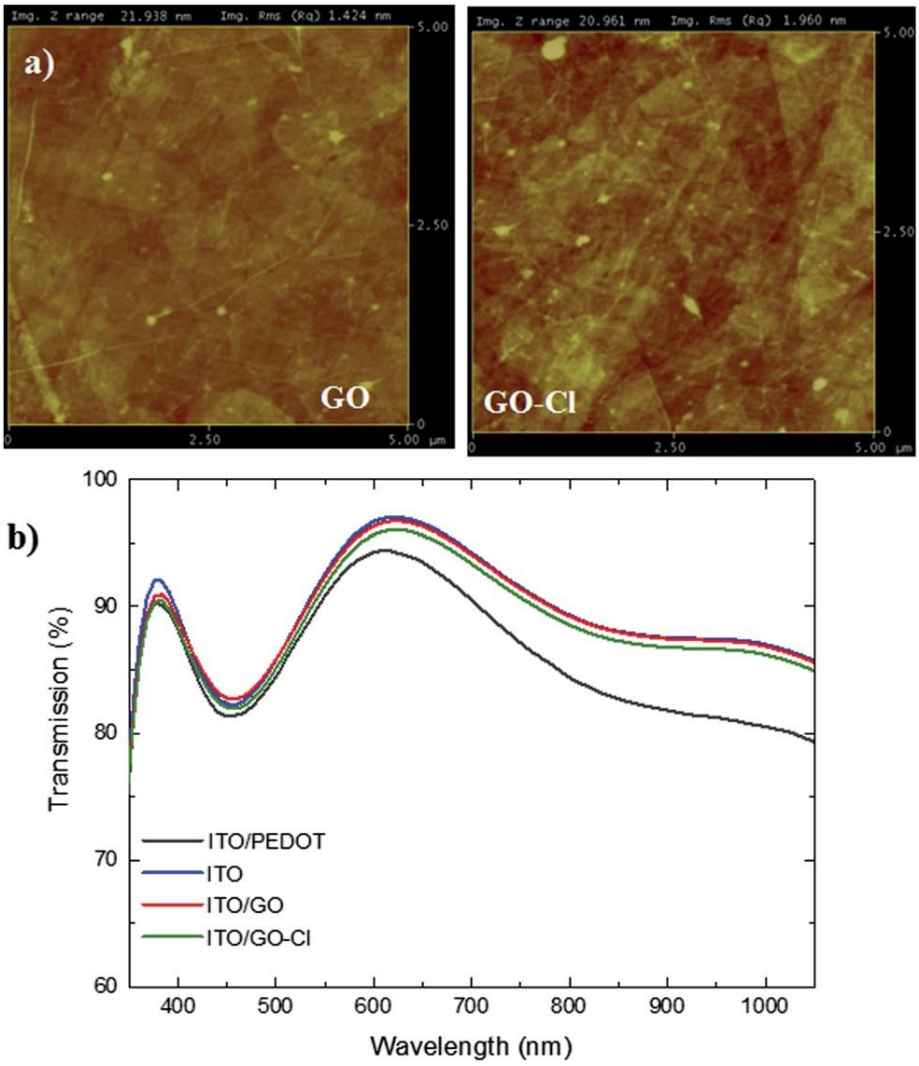

Figure 3.13: (a) 5 μm x μm AFM images of the GO (left) and the GO–Cl layer (right) with a RMS roughness of 1.424 and 1.96 nm on ITO/glass substrates. (b) Transmission spectra of GO and GO–Cl films spin coated on ITO/glass. The spectra of ITO glass and ITO glass coated with PEDOT:PSS are also shown.

Finally it is important to note that the mean roughness of both GO and GO–Cl HTLs is comparable as indicated by AFM measurements (Figure 3.13). This suggests

that the photochlorination process does not significantly affect the HTL film morphology. Figure 3.14 shows the typical illuminated current density–voltage (J–V) curves of the PCDTBT:$PC_{71}BM$ OPV devices with PEDOT:PSS, GO and GO–Cl (prepared at different exposure times) as the HTLs. As it can be seen in the J–V curves and the summarized photovoltaic parameters shown in Table 3.2, device performance is significantly enhanced by the photochlorination of the GO film and strongly depends on the WF of the GO–Cl layer. Indeed, the increase of the WF of GO–Cl films from 4.9 to 5.23 eV leads to a PCE of 6.56% which is 17.35% and 19.48% higher than that of the pristine GO and PEDOT:PSS based OPV devices, respectively. The PCE enhancement achieved via the GO film photochlorination is primarily a result of the increased JSC, which is proportional to the WF increase of the GO–Cl films.

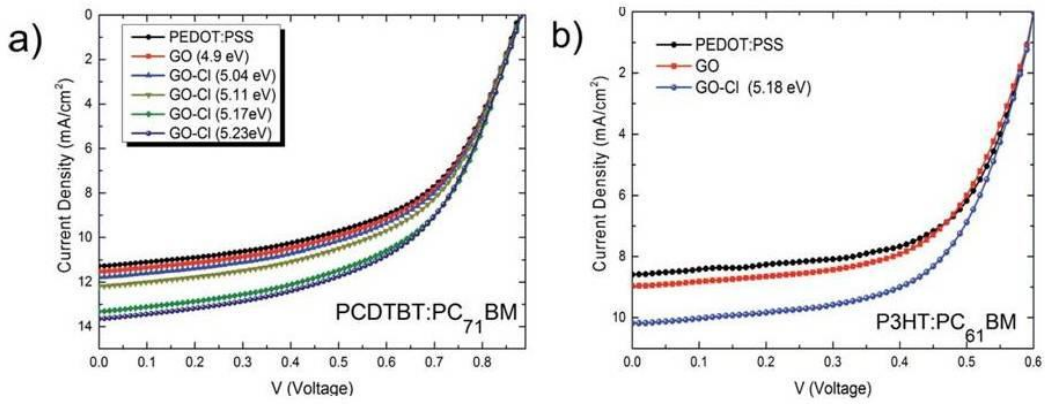

Figure 3.14: J–V characteristics of (a) PCDTBT:$PC_{71}BM$ and (b) P3HT:$PC_{61}BM$ photovoltaic devices with different HTLs under simulated A.M. 1.5, 100 mW cm^{-2} solar irradiation.

Table 3.2: Summary of the photovoltaic parameters of the fabricated OPVs with (a) PCDTBT:$PC_{71}BM$ and (b) P3HT:PC61BM active layers using different HTLs (the data were averaged from ten devices

HTL	J_{SC} ($mAcm^{-2}$)	V_{OC} (V)	FF (%)	PCE (%)
PCDTBT:$PC_{71}BM$				
PEDOT:PSS	11.27	0.88	55.3	5.49
GO 4.9 eV	11.52	0.88	55.1	5.59
GO-Cl 5.04 eV	11.78	0.88	55.1	5.71
GO-Cl 5.11	12.19	0.88	55.2	5.92
GO-Cl- 5.17 eV	13.32	0.88	55.1	6.46
GO-Cl 5.23 eV	13.65	0.88	54.7	6.56
P3HT:$PC_{61}BM$				
PEDOT:PSS	8.59	0.6	62.7	3.23
GO	8.96	0.6	61.0	3.28
GO-Cl 5,23 eV	10.18	0.6	61.3	3.74

This JSC increase cannot be attributed to the enhanced optical transmittance, since there was practically no difference in transparency between the pristine and photochlorinated GO HTLs (Figure 3.14b). Also, it should be noted that, the pristine GO based OPV slightly outperforms PEDOT: PSS due to a small increase of J_{SC}. Such an increase may be attributed to the improved hole transportation due to the 2D nature of the HTL. Our results suggest that the photocurrent enhancement can be explained by an improvement on the hole transport efficiency facilitated by the perfect match of the GO–Cl WF with the HOMO level of the polymer. To validate this presumption, hole-only devices with the structure ITO/HTL/PCDTBT:$PC_{71}BM$/ MoO_3/Au were fabricated for all different types of devices. The hole mobility was estimated from the J–V characteristics in the low voltage region, where the current is described by the Mott–Gurney square law[223]:

$$J_{SCLC} = \frac{9}{8} \varepsilon_o \varepsilon_r \mu_e \frac{(V - V_{bi})^2}{d^3}$$

where J_{SCLC} the current density of SCLC, ε_r is the relative permittivity of the organic active layer, ε_o is the permittivity of free space, V is the applied voltage, V_{bi} is the built-in voltage, μ_e is the electron mobility, and d is the thickness of the active layer[224].

It should be noted that the obtained hole mobilities refer to the complete device including the active and the HTLs. The hole mobilities of the devices prepared with PEDOT:PSS, GO and GO– Cl (5.23 eV) as the HTLs, respectively, are calculated from the currents in the square law region to be 9.64 x 10^{-5}, 1.2 x 10^{-4} and 2.35 x 10^{-4} cm^2 V^{-1} s^{-1}, respectively. Therefore, it is more than clear that the hole mobility increases as the GO–Cl WF increases, leading to higher PCEs due to improved hole transport. Further support of the enhancement effect of GO–Cl HTLs is the observation that OPV devices incorporating GO HTLs that were laser irradiated without the presence of chloride exhibit PCEs comparable with that of devices incorporating pristine GO HTLs. Moreover, the dark current density in reverse bias of the OPVs with GO–Cl is one order of magnitude lower than that of the OPVs with pristine GO HTLs, resulting in a higher diode rectification ratio and therefore better hole collection and electron blocking behavior. Therefore, it can be concluded that only the simultaneous partial reduction and chlorination of the GO films lead to an increased WF and hence the PCE.

A similar but less impressive performance enhancement was observed in OPVs with the P3HT polymer. As shown in Figure 3.13b, the devices with GO–Cl (5.23 eV) as the HTL, exhibited a PCE of 3.74%, which is 14% higher compared with the GO-based OPV device. This enhancement is lower than that obtained in the PCDTBT OPV device. This discrepancy in PCE enhancement is possibly due to the fact that the energy barrier between the HOMO of the PCDTB (5.3 eV) and the WF of GO–Cl (5.23 eV) is only 0.07 eV. While, in the P3HT (HOMO of 5 eV) case, the corresponding energy barrier is 0.23 eV. This reduced barrier in the case of PCDTBT enables more efficient charge transport and reduced recombination at the hole transport and photoactive layers, giving rise to higher PCE enhancement. Therefore, it can be concluded that tuning of the GO–Cl WF with respect to the energy levels of the polymer donor is the main performance enhancement factor. Indeed, the higher PCE enhancement observed using PCDTBT compared to the P3HT donor can be

attributed to the perfect match of the GO–Cl WF and the LUMO taking place in the former case. Optical or morphological side effects can be neglected, since the measured roughness and optical transmission of the pristine and the photochlorinated GO layers are comparable.

The OPVs with GO–Cl as the HTL exhibit significant higher lifetime stability when exposed to continuous solar illumination in air compared with OPVs using PEDOT:PSS. OPVs were tested under prolonged irradiation without any encapsulation. While OPVs with PEDOT:PSS as the HTL die after 20 h, OPVs fabricated with GO or GO–Cl HTLs preserve more than 70% and 50% of their initial PCEs for over 25 h and 45 h, respectively[188]. This result is due to the fact that PEDOT:PSS is spin coated from highly acidic suspension (pH ~ 1), which erodes ITO and causes indium migration into the photoactive layers. Also, water molecules can readily penetrate into the hygroscopic PEDOT:PSS layer, resulting in degraded device performance[196]. Thus, the GO–Cl not only enhances the device PCE but also acts against fast degradation of the device, offering a superior alternative HTL material.

Finally, it is important to note that the presented technique ensures low cost, since it is a room temperature process and applicable to flexible and light-weight substrates, and therefore compatible with large industrial roll-to-roll manufacturing of OPVs. A GO ink is printed onto flexible plastic foils using standard industrial inkjet printers, and then the GO film can be in situ photochlorinated using a scanning laser beam. Furthermore, the technique can be applied to other organic electronic devices, in which tuning of the electronic properties of the graphene ink is desirable.

3.2.4. Conclusions

In summary, ultraviolet laser irradiation in a chlorine gas medium was successfully employed as a facile and catalyst-free approach to prepare photochlorinated GO fims with controllable reduction and doping levels, and thus the work function. In effect, the resultant GO–Cl has been demonstrated to be an excellent HTL material for OPVs, significantly outperforming the reference PEDOT:PSS and pristine GO HTLs. This is attributed to its increased work function, which perfectly matches with the HOMO level of the PCDTBT, ensuring an ohmic contact at the interface. This new technique can employ other dopants not only to increase but also to decrease the GO

work function, aiming at its use as an electron transport layer, opening new avenues for the development of an all graphene based OPV.

3.3. Reduced Graphene Oxide Micromesh Electrodes for Large Area, Flexible, Organic Photovoltaic Devices

A laser-based patterning technique—compatible with flexible, temperature sensitive substrates—for the production of large area reduced graphene oxide micromesh (rGOMM) electrodes is presented. The mesh patterning can be accurately controlled in order to significantly enhance the electrode transparency, with a subsequent slight increase in the sheet resistance, and therefore improve the tradeoff between transparency and conductivity of reduced graphene oxide (rGO) layers. In particular, rGO films with an initial transparency of ~ 20% are patterned, resulting in rGOMMs films with a ~ 59% transmittance and a sheet resistance of ~ 565 Ω sq^{-1}, that is significantly lower than the resistance of ~ 780 Ω sq^{-1}, exhibited by the pristine rGO films at the same transparency. As a proof-of-concept application, rGOMMs are used as the transparent electrodes in flexible organic photovoltaic (OPV) devices, achieving power conversion efficiency of 3.05%, the highest ever reported for flexible OPV devices incorporating solution-processed graphene based electrodes. The controllable and highly reproducible laser-induced patterning of rGO hold enormous promise for both rigid and flexible large-scale organic electronic devices, eliminating the lag between graphene-based and indium–tin oxide electrodes, while providing conductivity and transparency tunability for next generation flexible electronics.

3.3.1. Introduction

Organic photovoltaics (OPVs) is a promising technology for future low cost energy supply due to its ability to employ flexible substrates enabling futuristic applications and mass production technologies such as roll-to-roll (r2r) manufacturinggh[225,226,227]. Being the first layer of an OPV device that comes in contact with the light, the transparent conductive electrode (TCE) is a vital determining factor to the device power conversion efficiency (PCE). Recently, OPV devices with efficiencies above

10% were certified, with their operation lifetimes exceeding industrially interesting levels[228,229]. Indium–tin oxide (ITO) is currently the dominant material used as TCE in rigid optoelectronic devices owing to its high transparency, T_r, in the visible spectrum and its good conductivity[230]. However, considering the employment of OPVs in everyday applications, the electrodes should be inexpensive, lightweight, and highly elastic in order to conserve their electrical properties under high stresses. In this context, ITO suffers from considerable limitations. First, it is expensive due to both the scarcity of indium reserves and the sputter deposition line expenses and second is not flexible, since its polycrystalline microstructure is brittle and cracks when the layer is bent or stretched repeatedly[231]. On top of that, indium is known to diffuse through the photoactive layer, leading to significant deterioration of the photovoltaic performance[232,233,234]. Therefore, the progress of flexible OPVs is much slower due to the lack of a flexible transparent and high conductive electrode; a r2r compatible substitutive material for ITO with a similar performance, but lower cost is highly desired.

Solution-processed carbon nanotubes[235,236], metallic nanowires[237] and conductive polymers[238] have been utilized as the TCE in organic electronic devices. However, they exhibit relatively high surface roughness or large sheet resistance, R_s, thus reducing the reproducibility rate of the devices.

Ever since the isolation of free standing graphene in 2004[20], graphene research has experienced a phenomenal growth. Graphene can be produced by several techniques, including micromechanical exfoliation of graphite[1], sonication-induced exfoliation[28], thermal- or plasma-enhanced chemical vapor deposition (CVD) deposition from a carbon feedstock gas[239,240], laser-induced exfoliation[241,242] and carbon nanotubes unzipping by either laser[243] or chemical treatment[244]. Graphene's exceptional electronic, optical, and mechanical properties make it highly attractive, believed to be the next wonder material for optoelectronics and thus triggering the application of graphene-based materials in the different layers of photovoltaic devices[245,246,247,248]. In particular, the enhanced electrical conductivity, combined with its high transparency in visible and near infrared spectra[249], emerged graphene as an ideal low cost ITO substitute.

CVD has been reported as the most successful approach to produce highly transparent and low R_s graphene electrodes[250]. Nonetheless, the as-grown graphene films have to be transferred onto a target substrate through a complicated process, increasing the manufacturing cost. An alternative low cost approach compatible with r2r mass production is the chemical exfoliation of graphene oxide (GO) either by ultrasonic dispersion or rapid thermal expansion followed by reduction with proper chemical[251] or laser-assisted routes[252,46,253]. The reduced GO (rGO) can be easily produced in bulk quantities as graphene ink,[254] taking advantage of its improved soluble character in common solvents[255]. In this context, there was an extensive research effort on the utilization of rGO as the TCE in OPVs[256,257,59]. Nonetheless, the recorded PCEs remain low (~1.0%), mainly due to the low T_r (70%) and high R_s of the rGO films (~ 1 kΩ sq^{-1}), compared to the highly commercialized ITO (90%, 15 Ω sq^{-1}). In the same context, our group has recently demonstrated an efficient laser-based reduction method for fabricating flexible conductive and transparent graphene films that can be spin-casted on temperature-sensitive substrates. The femtosecond (fs) laser-treated rGO (LrGO) films with 70% T_r and R_s of 1.6 kΩ sq^{-1} were integrated in polymer–fullerene photovoltaic cells, as the TCE leading to an effi ciency of 1.1%[129]. Therefore, it is evident that pristine rGO films cannot compete with ITO, due to their extremely high R_s (>1 kΩ sq^{-1}) for high transparency values.

One of the most eye-catching strategies for increasing the transparency of a TCE material is the employment of a mesh structure with periodic lines, as applied in copper[258] and silver[259] network mats. Their R_s and transparency can be controlled by varying the grid width, spacing, and thickness[260]. In this way, the transparency of the mesh film can be significantly increased compared with the pristine film, while the R_s alternation is minimal; the percolated network can conduct current even with the presence of large empty spaces. In this context, various patterning techniques were developed, such as lithography with block copolymer[261], ion beam[262], plasma etching[158,263], template method[264] and chemical etching[265]. Most recently, rGO meshes fabricated using standard photolithography and O_2 plasma methods were utilized as the TCE in OPVs[266,267], while laser-induced patterning of GO[268] has been reported for energy storage[269] and memory applications[270]. However in both cases, the employment of a mask aligner and the additional process step of the photoresist removal by O_2 plasma, induce high cost and complexity in the device fabrication.

In contrast to photolithography patterning, fs laser patterning[271] has been proposed as a versatile tool for high precision patterning on a wide range of materials and in large scale[272]. The main advantage of the induced fs laser patterning is that it can be applied to temperature-sensitive substrates, such as polyethylene terephthalate (PET), without practically affecting its integrity during processing. In this work, we propose a low cost, high throughput, fully scalable, and facile technique for one-step patterning of rGO films on PET or glass substrates based on fs laser irradiation. This technique which can be easily controlled over the entire illuminated area induces minimum thermal damage in the surrounding layers and more importantly is compatible to r2r production processes[273]. Furthermore, direct laser patterning has the advantage of arbitrary designability and reasonably high spatial resolution[274]. By utilizing this methodology, rGO micromeshes (rGOMM) are fabricated, enabling to overcome the tradeoff between R_s and T_r of pristine rGO layers. The optoelectrical properties of rGO thin films are found to be directly dependent on the interplay between the periodicity and the geometrical characteristics of the mesh pattern structure. Approximately 100 nm thick rGO films with 22.5% T_r can be patterned to form TCEs with significantly increased T_r (up to ~ 85%), and simultaneous tuning of the film conductivity and sheet resistance. As a proof of concept, we successfully employed the rGOMM as the TCE in small and large active area of PCDTBT:$PC_{71}BM$ based air processed OPV device, achieving PCE values of 3.67% and 3.05% on glass and flexible substrates, respectively. To the best of our knowledge, these are the highest PCEs reported for a solution processed graphene-based TCE in OPVs. This laser-based patterning technique can be considered as a universal strategy in order to fabricate large-scale graphene films with controlled electrical and optical properties for various flexible electronic device components.

3.3.2. Experimental

Preparation of GO

[218]GO was prepared from graphite powder (Alfa Aesar, ~ 200 mesh) according to a modified Hummers' method. In more detail, graphite powder (0.5 g) was placed into a mixture of H_2SO_4 (40 mL, 98%) and $NaNO_3$ (0.375 gr). The mixture was then stirred and cooled in an ice bath. While maintaining vigorous stirring, $KMnO_4$ (3.0 g) was

then added in portions over a period of 2 h. The reaction mixture was left for 4 h in order to reach room temperature before being heated to 35 ^{o}C for 30 min. It was then poured into a flask containing deionized water (50 mL) and further heated to 70 ^{o}C for 15 min. The mixture was then decanted into deionized water (250 mL) and the unreacted $KMnO_4$ was removed by adding 3% H_2O_2. The reaction mixture was then allowed to settle and decanted. The graphite oxide obtained was then purified by repeated centrifugation and redispersed in deionized water until neutralized pH was achieved. Finally, the resulting GO was dried at 60 ^{o}C in a vacuum oven for 48 h before use.

Preparation of rGO Films

GO films were prepared by vacuum filtering the aqueous solutions of GO through mixed cellulose ester membranes (0.025 μm, Millipore). By either varying the filtration volume or the concentration of GO in the solution, films with varied thicknesses and thus different transparencies can be produced. In this case, the initial concentration of the GO solution used for film preparation was 5 mg L^{-1} . Aliquots of the GO solution were further diluted in water, sonicated to achieve exfoliated sheets of GO, and filtrated. The GO-coated membrane was cut into the desired sizes, immersed in deionized water to be wetted, and placed with the fi lm side down onto the substrate (PET and glass) surface. The GO film was allowed to dry and adhere to the substrate at room temperature under a 1 kg weight. After 5 h the membrane was removed, leaving the GO films on the substrates, which were dried in a 60 °C oven. The process is highly repeatable and the films are well adhered to glass and plastic substrates. The reduction of GO films can be performed by exposing them to hydriodic acid (55%)/ acetic acid vapor[275]. In detail, the as-prepared PET/GO and glass/GO films were placed on a stand inside a small desiccator that contained a mixture of HI (2.0 mL) and AcOH (5.0 mL). The desiccator was sealed and placed in an oil bath at 40 ^{o}C for 24 h. The films were then washed with methanol and dried at 60 ^{o}C in an oven. For the R_s improvement, the prepared rGO films were subjected to additional chemical treatment, by dipping them in a HNO_3 bath for 1 h, followed by cleaning and drying the surface under nitrogen steam[250,276].

Fabrication of rGO Nanomesh

The rGO films were mounted on a computer controlled motorized X – Y translation stage. During the irradiation, the rGO films were scanned in two orthogonal directions (X and Y) in a fully controlled manner across a focused excimer laser beam (fluence ~ 0.4 Jcm^{-2} , beam size 0.02 mm^2 , pulse width 0.5 ps, respetition rate 1 Hz, emission wavelength 248 nm). The dependence of the transparency of the rGO films with the mesh periodicity was examined by controlling the movement step of X – Y stage. As a result of laser irradiation, part of the irradiated material was ablated in order to achieve higher transparency. By increasing the number of laser pulses, greater amount of the irradiated material was removed.

Device Fabrication and Measurements

PCDTBT and $PC_{71}BM$ were purchased from Solaris Chem. PCDTBT:$PC_{71}BM$ were dissolved in 1,2-dichlorobenzene: Chlorobenzene (3:1) (o-DCB:CB) in a 1:4 (4 mg:16 mg) ratio and stirred for at least 72 h at 80 ^oC before used. The ITO-based photovoltaic devices were fabricated on 20mm × 15 mm ITO-coated PET substrates with R_s of 100 Ω sq^{-1} (Sigma-Aldrich). The rGOMM electrodes were prepared on flexible PET (Goodfellow) substrates (20mm × 15 mm) with 90 μm thickness. The impurities were removed from the substrates through a three-step ultrasonication cleaning process (deionized water with soap, aceton, IPA). As a buffer layer, poly(ethylene-dioxythiophene) doped with poly(4-styrenesulfonate) (PEDOT:PSS), purchased from Heraeus, was spin-cast from an aqueous solution on the rGOMM and ITO-coated electrodes with a layer thickness of the layer was 20 nm and 30 nm, respectively, followed by baking for 15 min at 120 ^oC inside a nitrogen-filled glove box. The PCDTBT:$PC_{71}BM$ photoactive layer was subsequently deposited by spin-coating the blend solution at 1000 rpm on top of PEDOT:PSS layer until the thickness reaches approximately 70 nm, followed by drying at 60 ^oC for about 5 min under inert condition. Titanium suboxide (TiO_x), used as the electron transport layer, was prepared according to a literature method[277]. TiO_x was dissolved in methanol (1:200) and then spin-coated to a thickness of approximately 10 nm (6000 rpm, 40 s) in air[207]. The samples were heated at 80 ^oC for 1 min in air. Finally, 100 nm of Al was deposited through a shadow mask by thermal evaporation on the devices. The whole device fabrication occurred in ambient conditions.

The performances of the devices were measured at room temperature with an Air Mass 1.5 Global (A.M. 1.5 G) solar simulator at an intensity of 100 mW cm^{-2}. A reference monocrystalline silicon solar cell from Newport was used to calibrate the light intensity. All measurements were carried out in air immediately after device fabrication without encapsulation process.

3.3.3. Results and Discussion

The as-prepared, using the modified Hummers' method[218], GO was dispersed in water to form stable aqueous solutions. Vacuum fi ltration technique was used to deposit uniform layers of GO on top of mixed cellulose ester (MCE) membrane. The thickness and the homogeneity of the GO films can be accurately controlled by simply varying either the concentration of the GO solution or the filtration volume. The prepared GO films were transferred on glass and PET substrates for further treatment. To restore the conjugated structure of graphene and improve the films conductivity, chemical reduction is performed by exposing the GO films to hydriodic acid/acetic acid (HI/AcOH)[275]. Figure 3.15 presents the x-ray photoelectron spectroscopy (XPS) survey spectra of GO and rGO, indicating that most oxygen-containing groups are effectively removed during HI/AcOH reduction.

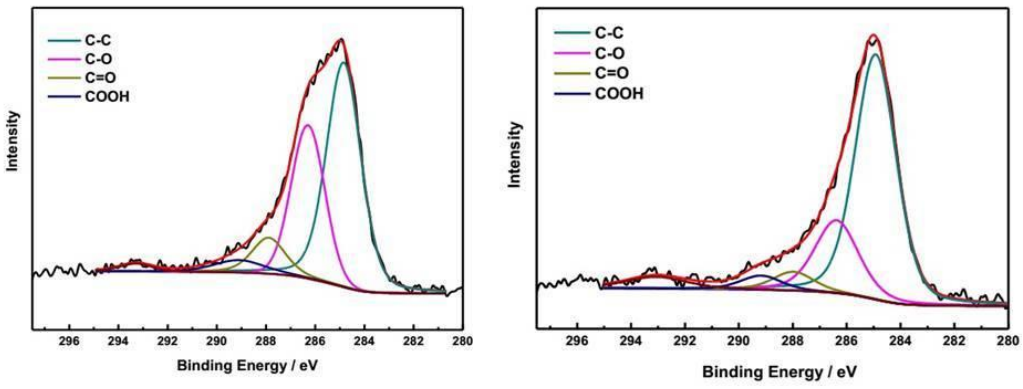

Figure 3.15: High-resolution XPS C1s spectra for a) GO and b) rGO (HI-AcOH).

Nitric acid (HNO_3) has been widely used as p-type dopant to improve the conductivity and charge transfer efficiency of carbon structures[250,276]. Figure 3.16a presents the correlation of R_s and T_r at 550 nm of rGO films to their thicknesses. Both T_r and R_s decrease with increasing film thickness, highlighting the inherent tradeoff between the two factors. The R_s as a function of transmittance before and after HNO_3 treatment is demonstrated in Figure 3.16b. It is clear that R_s shifts to lower values (~27% decrease) after additional treatment by dipping the prepared rGO films in a HNO_3 bath (65%) for 1 h.

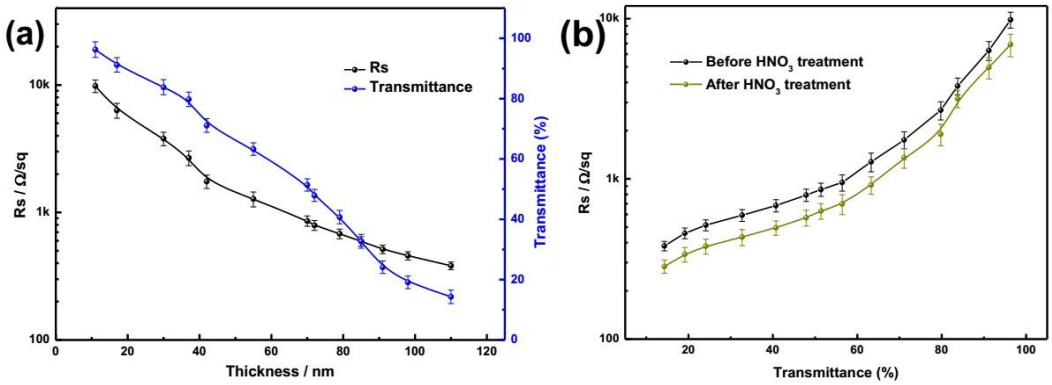

Figure 3.16: a) Transmittance and sheet resistance of rGO thin films as a function of thickness. b) Plot of sheet resistance vs transmittance at 550 nm before and after doping with nitric acid.

The selective laser patterning of rGO on top of glass or PET (Figure 3.17) was performed with the delivery of UV ultrashort laser pulses (248 nm, 500 fs) with 1 Hz repetition rate. Unlike previous studies[278], the proposed process is one-step and does not require time-consuming and labor-intensive lithography; no complex masks, post-processing, or clean room facilities are required. Even though it is a point-by-point patterning technique, the processing rate can be significantly increased using high repetition laser sources and multiple beam interference irradiation schemes[279]. Besides this, it is a fully automated technique, allowing processing of the rGO layers according to preprogrammed patterns. In our experiments, the rGO mesh periodicity, the number of pulses per pit, as well as the neck width of the mesh could be readily controlled.

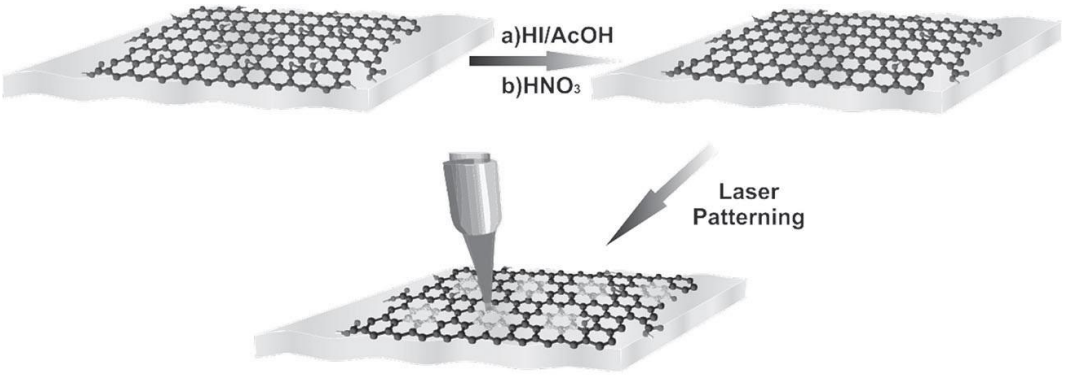

Figure 3.17: Schematic illustration of the rGO mesh electrodes preparation

The physical processes (Figure3.18) that follow fs laser–matter interactions are various and occur in different timescales. Specifically, the laser pulse energy is initially absorbed by the electrons and is transferred to the lattice over a picosecond timescale. Within a few nanoseconds a shock wave is propagating away from the electron plasma. On the microsecond timescale, the thermal energy diffuses out of the focal volume. The heat generation can be finely controlled by several factors including layer absorption properties, laser power, number of pulses per spot, and beam profile. For a certain beam and above a minimum laser energy value, single shot ablation can be observed that causes permanent structural changes. In our case, the excimer laser beam used had a rectangular intensity profile and its energy per pulse was adjusted with the aid of a half-wave plate. Besides this, the focusing optics defined the focal volume and thus the mesh pattern size (the latter is also defined by the number of laser pulses)[280] and its symmetry[281]. It was observed that the minimum laser fluence required to partially remove rGO was 386 $mJcm^{-2}$; this fluence was enough to attain a strong optical contrast between the processed and non-processed area, observed by optical microscopy. Upon increasing the laser pulse energy or the number of pulses per irradiating spot (exposure time), the irradiance is increased and consequently the ablated depth.

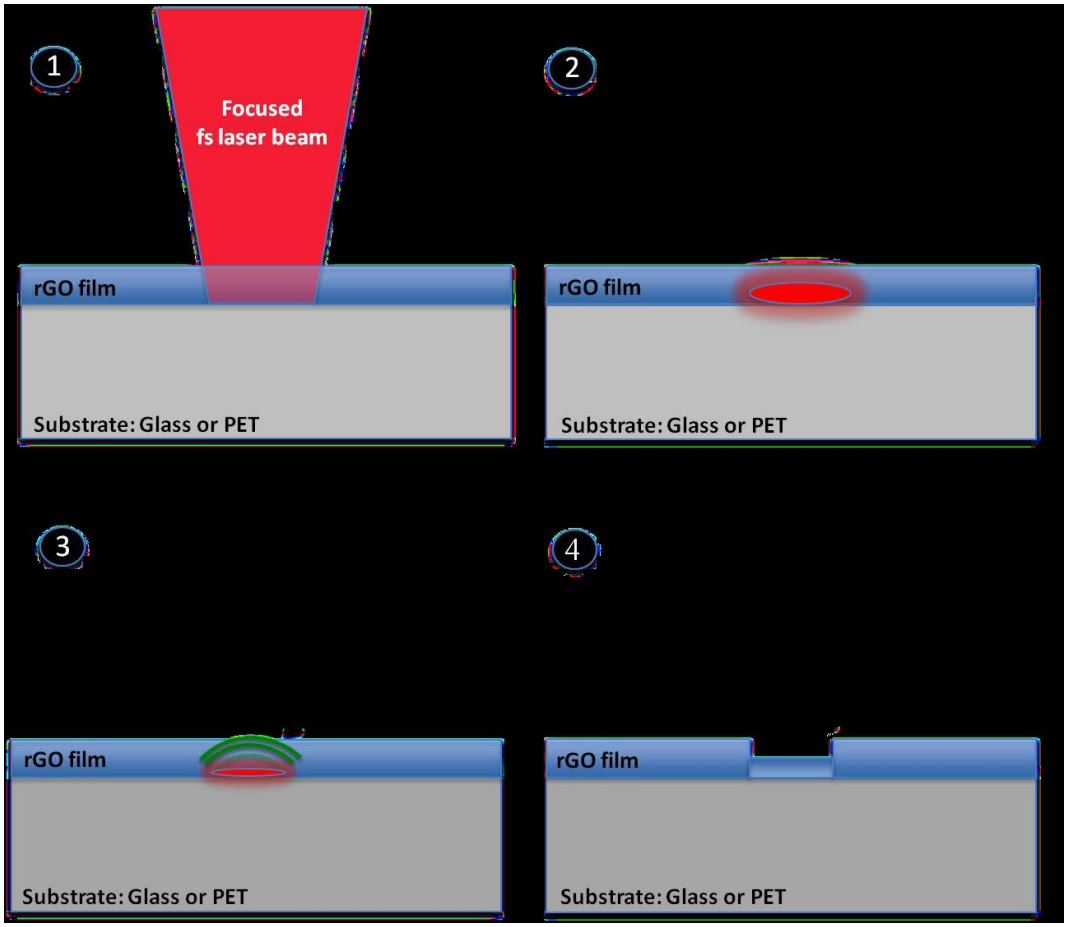

Figure 3.18: Cross section schematic of rGO film partially ablation 1) Irradiation with an UV focused fs laser pulse, 2) Absorption of the laser pulse energy 3) Due to sample heating a shock wave is generating and 4) ablates the film layer.

It is found that the ablation or pit depth is a key factor that determines the transparency and sheet resistance of laser-patterned rGO layers. Besides this, the number of fs laser pulses needed to achieve the optimum tradeoff between T_r and R_s is determined by the rGO layer thickness (initial T_r) and the substrate over which the film has been deposited. As we have previously demonstrated, the primary advantage of utilizing fs laser irradiation lies in the ability of in situ controlled epidermal treatment giving rise to minimum induced thermal effect on the supporting substrate[129]. This, in turn, enables for selective removal of the rGO material without practically affecting the integrity, even of thermally sensitive substrates underneath. It further allows the progressive removal of rGO upon using a series of pulses. This is in contrast to our experimental observation that the use of longer pulse duration gives rise to, uncontrolled, explosive ablation of the thin layer, causing the merge of

neighboring mesh features, as well as thermal distortion of flexible substrate due to heat of the accumulation effects. Both effects were found to be detrimental to the conductivity of the treated rGO layers.

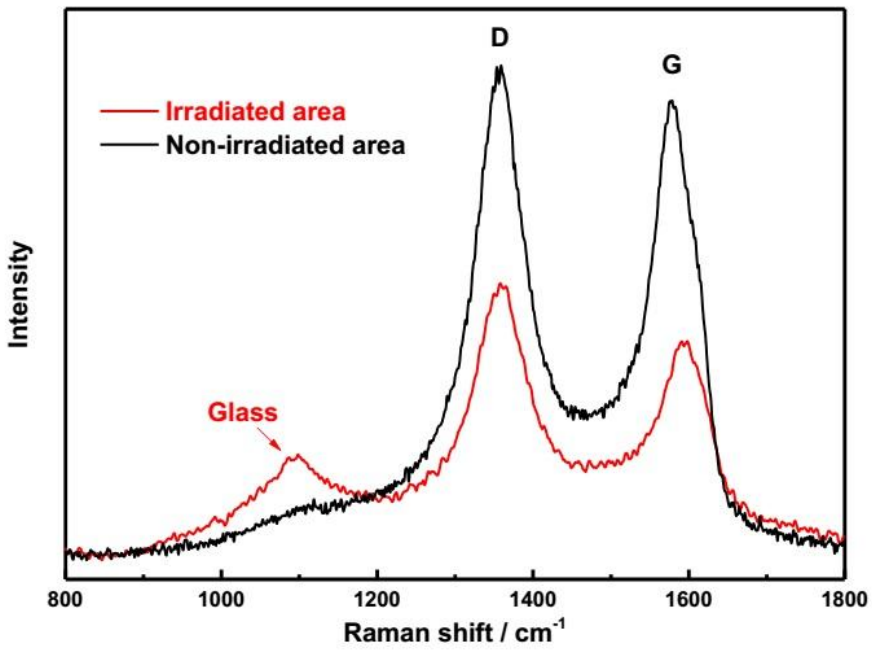

Figure 3.19: Raman spectra of rGO irradiated (red line) and non-irradiated areas (black line). In the case of irradiated areas the laser ablation of rGO in some areas is so intense that the glass substrate peak appears.

The effectiveness of laser patterning has been examined on the frame of the composition and surface morphology differences between the pristine and irradiated areas. The former were investigated through Raman spectroscopy, whereas the latter were examined by atomic force microscopy (AFM). The progressive material removal induced upon increasing the number of irradiation pulses, N, is demonstrated by the Raman spectra of the pristine and laser-patterned regions of the rGO mesh on glass, using N = 2 and N = 3 laser pulses of the threshold fluence, respectively (Figure3.19). The appearance of the D (1359 cm^{-1}) and G (1578 cm^{-1}) peaks in the irradiated area for N = 2 but with decreased intensity, demonstrates the partial etching of rGO from the irradiated areas. At the same time, a Raman peak at 1045 cm^{-1} corresponding to the glass substrate becomes more pronounced. On the contrary, for N = 3 the rGO

peaks disappear, indicating the complete removal of the rGO layer. AFM was employed to observe the difference in the surface morphology of irradiated and non-irradiated areas on the rGO films. Figure 3.20 demonstrates a quite homogeneous and smooth surface for the non-irradiated area, with a root-mean- square (rms) roughness value of 1.59 nm. Following laser treatment with N = 2, the rms roughness was increased to 6.99 nm due to the abrupt ablation process.

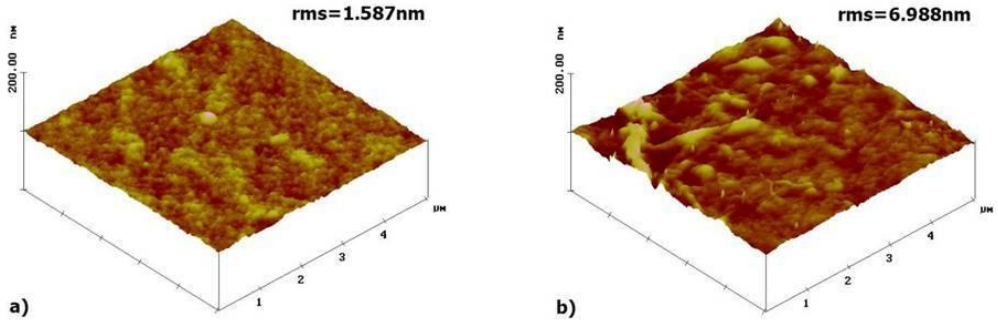

Figure 3.20: AFM images of a) non-irradiated and b) irradiated area in rGO film showing that roughness is increased after laser ablation.

Figure 3.21 presents scanning electron microscopy (SEM) images of the laser-generated rGO mesh patterns obtained upon irradiation with N = 2 at the threshold fluence. The bright spots in the illumination area reveal the partial ablation of the rGO layer, which is in agreement with the respective Raman spectra. In addition, the observed mesh pattern spatially shape variations are mainly due to small laser pulse energy fluctuations. Regarding the optimum neck width of the mesh, it should be as small as possible in order to reduce the losses due to light shadowing effects on the one hand and to retain the sheet conductivity on the other.

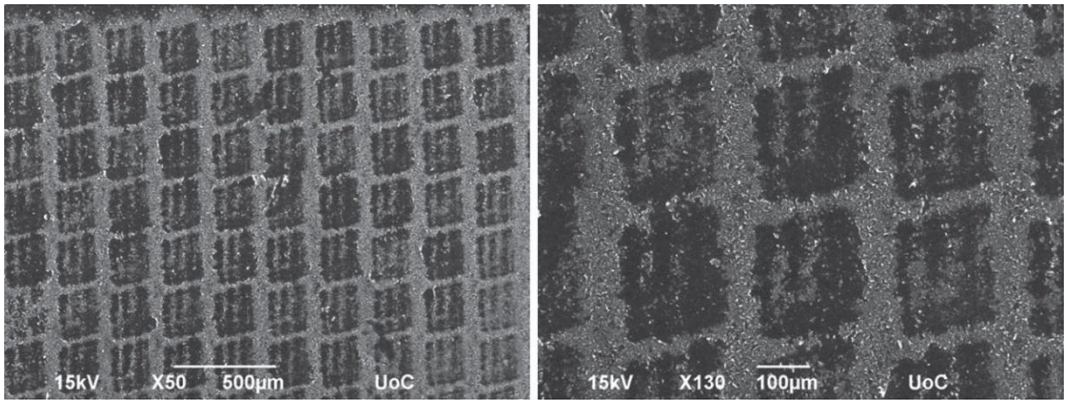

Figure 3.21: SEM images of the laser induced mesh patterns. The samples has been irradiated with N=2 fs pulses of 386 mJcm-2 fluence. The laser generated mesh has a period of 250 μm and the transparency has increased by ~ 48%.

One of the key challenges in rGO microelectronic devices applications is to tune the relation of T_r and R_s in a controllable manner[282]. The attractiveness of the technique proposed here is that it permits such fine tuning via variation of the irradiation dose (energy, number of pulses) and/or the periodicity and thus the neck width of the mesh. For instance, Figure 3.22 a–d demonstrate the progressive increase of T_r upon variation of the periodicity, D, of the rGOMMs pattern using the threshold fluence. Although the initial T_r of the rGO layer was ~ 20% it was significantly improved to ~ 85% for D ~ 213 μm (Figure 3.22d). At the same time, as shown in Figure 3.22e, the layer conductance slightly decreases, which is highly desirable for TCE applications. It should be noted here that, regardless of the substrate used, the lowest conductance changes can be only achieved provided that a continuous rGO film is realized after the laser patterning process, i.e., without complete removal of GO at the irradiated areas.

The cost effectiveness of the presented laser patterning technique can be supported by the following: (a) it does not require any strict operational conditions or complex facilities, compared to other techniques like e-beam and ion beam lithography[283], (b) it provides high flexibility for arbitrary graphene oxide patterning since it is noncontact and computer driven, (c) it is maskless in contrast to other patterning techniques[240,261], (d) the use of fs laser pulses make it compatible with

flexible, low cost substrates, (e) it is a one-step and not time-consuming process, (f) it is operated under open air and room temperature conditions, and (g) the fabrication setup is simple and easily controllable. Finally, the laser-assisted maskless patterning is easily reproducible since its key parameters, laser irradiance and micromesh periodicity, can be controlled with high precision.

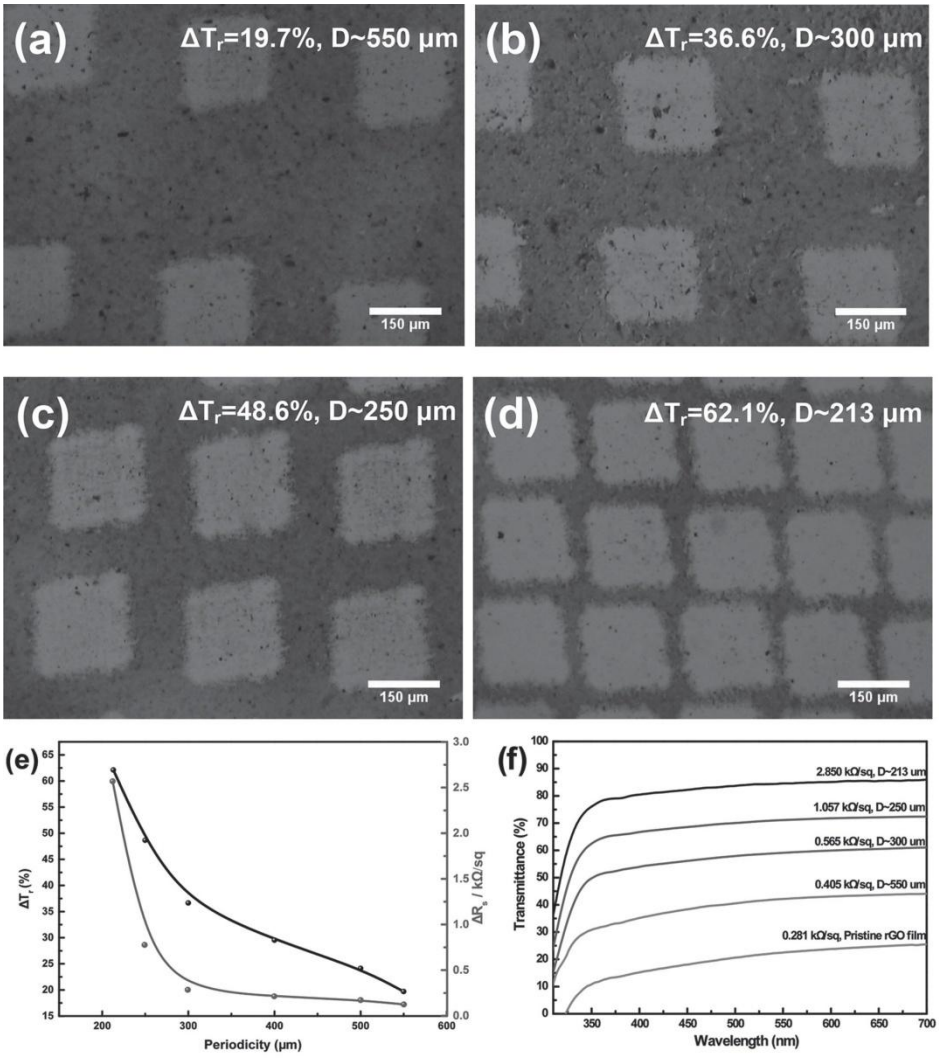

Figure 3.22: Optical microscopy images of laser-generated rGOMMs demonstrating the effect of the mesh periodicity on the film transmittance. Transparency was increased by a) ΔT_r=19.7%, b) ΔT_r=36.6%, c) ΔT_r=48.6%, d) ΔT_r=62.1% with ~ 550 μm, ~ 300 μm, ~ 250 μm and ~ 213 μm periodicity respectively. e) Transmittance difference at 550 nm (ΔT_r) and sheet resistance difference (ΔR_s) as a function of the periodicity (D) of the laser-induced rGOMM. The starting values for the pristine rGO layer were T_r 22.5% and R_s~281 Ωsq^{-1}. f) Optical transmittance spectra of rGOMMs with different periodicities, demonstrating also the Rs values of the rGO film after the laser patterning.

Compared with previously established patterning techniques, the presented laser-based method exhibits unique advantages. It is a one-step method, since no grid-like patterning masks or any further transfer steps, are required. In addition, there is no need of any photoresistive material[284] or prepatterned elastomeric stamps[285], while the use of fs laser pulses allows the pattering of microsize holes on top of flexible, temperature sensitive, and low cost materials. Finally, its operation can be performed under ambient and it is fully automated, since all the patterning parameters—mesh period and laser parameters—are precisely controlled by a specially designed software. The main disadvantage of the proposed laser technique is related with the finer mesh dimensions attainable, which are optical diffraction-limited. As a result, the technique can provide micrometer- or at most submicrometer-sized patterns, contrary to nanosized features that can be achieved by other competitive methods[261].

As a proof of the potential application of the proposed method for the fabrication of high performance transparent electrodes, we applied the rGOMM layers as the bottom TCE layer in flexible OPV devices, aiming to identify the optimum combination of T_r and R_s leading to the best PCE. For this purpose, we have used the rGOMM meshes demonstrated in Figure 3.22 e and 3.22 f. Devices were fabricated on PET substrates and the performance of OPV devices with PCDTBT:$PC_{71}BM$ photoactive blends deposited on rGOMMs was compared with those deposited on ITO. The OPV devices structure employed is schematically presented in Figure 3.23a, with holes collected in the TCE electrode and electrons in the Al metal electrode. Figure 3.23b presents the illuminated J – V characteristics for the best performed OPV device incorporating rGOMM as TCE, compared with the control ITO-based one, while Table 3.3 summarizes the averaged photovoltaic parameters of the whole series of OPV devices measured. The standard deviations of all measured quantities are presented in Figure 3.24.

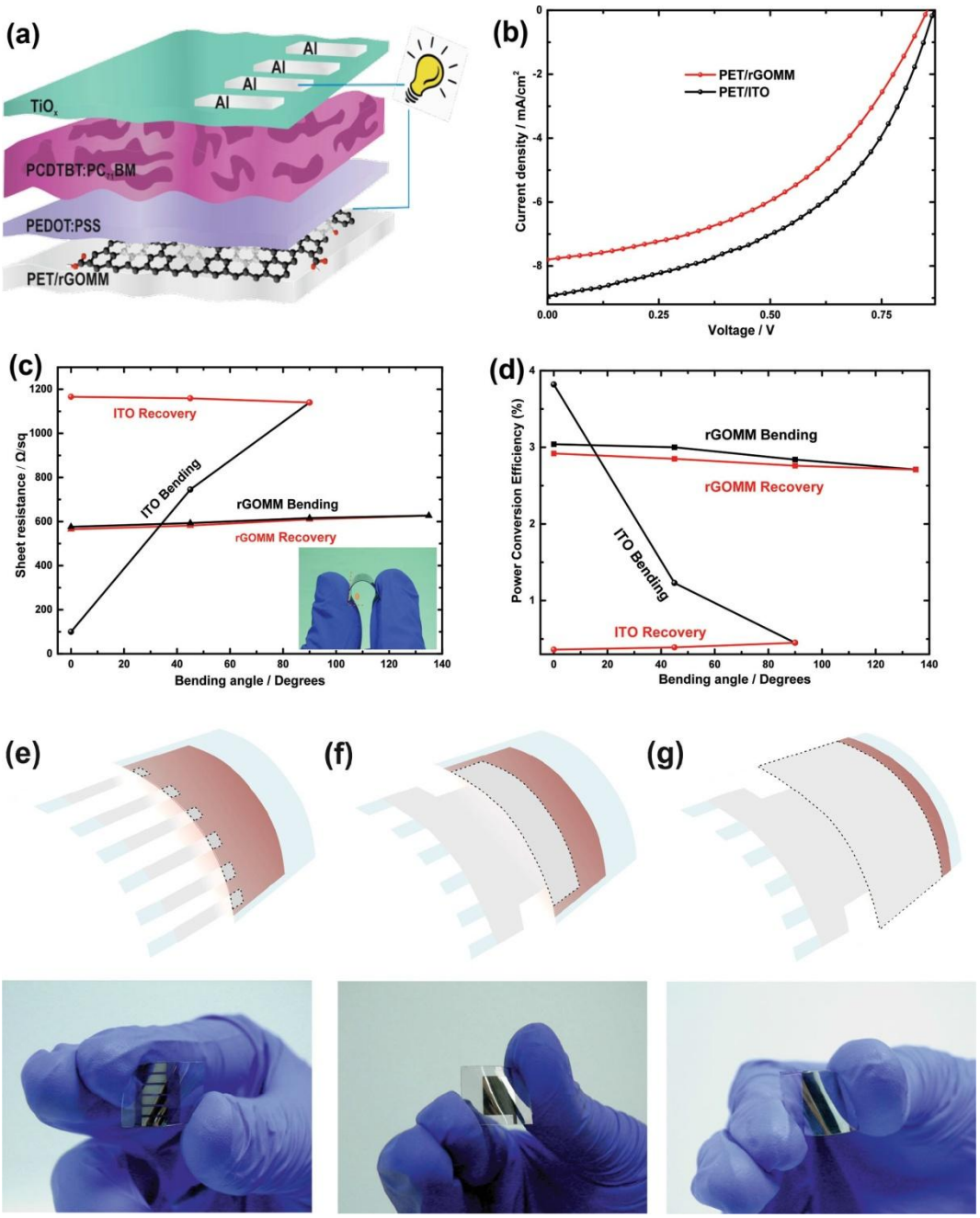

Figure 3.23: a) Schematic illustration of BHJ OPV device with the laser-induced rGOMM as TCE. b) The illuminated current-voltage (J-V) curves of the solar cells with rGOMM (red) and ITO (black) as TCE. c) Sheet resistance vs device bending angle of rGOMM- and ITO-based OPV cells. The inset photo represents a rGOMM-based device subjected to bending. d) PCE of rGOMM- and ITO-based flexible devices under and after bending at certain angles. Schematic illustration and photographs of devices exhibiting increased active areas; e) 4 mm^2, f) 50 mm^2 and g) 135 mm^2.

Table 3.3: Averaged photovoltaic parameters of the solar cells incorporating rGO, rGOMMs and ITO as TCE

PET/rGOMM (T, R_s)	J_{SC} ($mAcm^{-2}$)	V_{OC} (mV)	FF (%)	PCE (%)
22.5%, 281 Ωsq^{-1} (pristine rGO film)	4.51	837	47.2	1.78
42.2%, 405 Ωsq^{-1}	6.52	843	46.4	2.55
59.1%, 565 Ωsq^{-1}	7.81	848	45.9	3.05
71.1%, 1057 Ωsq^{-1}	3.72	840	42.3	1.32
84.6%, 2850 Ωsq^{-1}	2.37	832	37.6	0.74
PET/ITO	8.93	864	49.5	3.82

*Average photovoltaic characteristics for OPV devices with different TCEs. To account for experimental errors, the reported averages for each case are taken for 10 identical devices, consisting of six cells each.

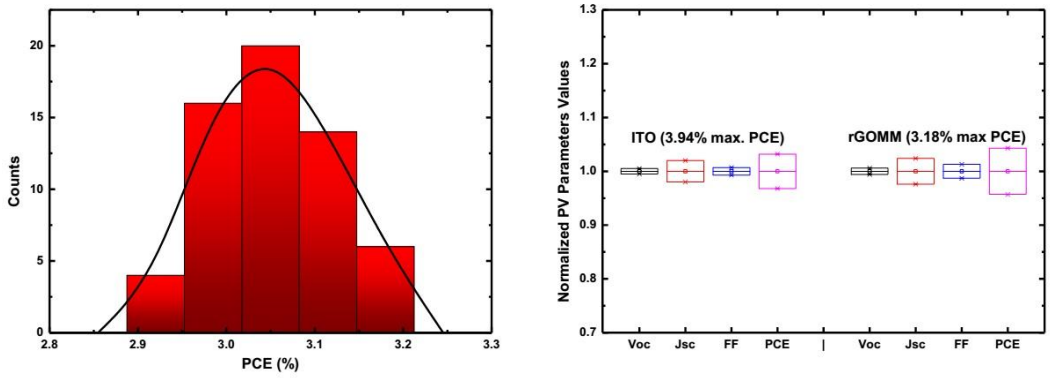

Figure 3.24: a) Histogram of average efficiencies for 60 cells. b) Standard deviations for the photovoltaic parameters values.

It can be clearly observed that the open circuit voltage (V_{oc}) remains almost constant for all devices, which is reasonable, considering that its value is derived by the energy levels offset between the highest occupied molecular orbital (HOMO) of PCDTBT and lowest unoccupied molecular orbital (LUMO) of $PC_{71}BM$. On the other hand, a tradeoff between the photocurrent (J_{sc}) and fill factor (FF) is observed. In

particular, the J_{sc} is increased as the T_r of the rGOMM layer becomes higher, up to the limit that R_s remains in the same order of magnitude compared to the starting material. The FF is mainly affected from the R_s of TCE, thus is constantly decreased as the mesh structure becomes denser. As can also be seen by the 3D graph of Figure 3.25, the optimum photovoltaic parameters for the rGOMM-based devices were extracted for T_r ~ 59.1% and R_s ~ 565 Ω sq^{-1}, with a resulting PCE of 3.05%.. Furthermore, OPV devices incorporating rGO films with different thicknesses and therefore different T and R_s pairs were also fabricated and characterized (Table 3.4). In this way, a direct comparison of the PV performance of the optimum devices, utilizing unpatterned rGO and patterned rGOMM films, can take place.

Table 3.4: Averaged photovoltaic parameters of the solar cells incorporating different (T, R_s) rGO and rGOMM as TCE.

	(T, R_s)	J_{SC} ($mAcm^{-2}$)	V_{OC} (mV)	FF (%)	PCE (%)
rGO	22.5%, 281 Ωsq^{-1}	4.51	837	47.2	1.78
	60.3%, 819 Ωsq^{-1}	5.92	834	42.5	2.12
	69.7%, 1235 Ωsq^{-1}	6.73	835	40.1	2.25
rGOMM	59.1%, 565 Ωsq^{-1}	7.81	848	45.9	3.05

It can be clearly seen that the performance of the rGOMM-based devices is superior to the devices, which utilize rGO films, mainly due to the difference in R_s , which has a strong effect on the devices FF. In particular, the unpatterned rGO-based device exhibits a maximum PCE of 2.12%, while the rGOMM-based device exhibits a PCE of 3.05%. Also, the device which utilizes rGO as the TCE with approximately the same transparency as the rGOMM film (60.3% and 59.1%, respectively) exhibits an even lower PCE of 2.12%, due to the significant difference in the R_s of the TCE. Therefore, the laser patterning technique clearly enables us to improve the tradeoff between T_r and R_s of the rGO films, since patterned films with the same transparency as the unpatterned rGO films exhibit much higher conductivity values.

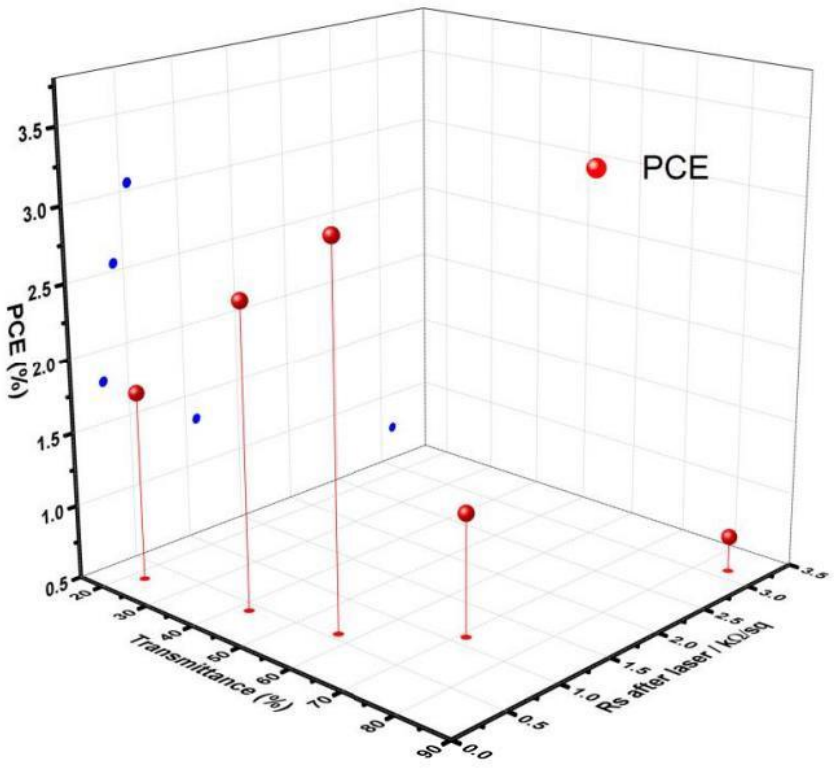

Figure 3.25: 3D graph for the variation in power conversion efficiency in flexible devices with respect to the transmittance and sheet resistance of the produced rGOMMs films.

Table 3.5.: Summary of the averaged photovoltaic parameters for optimum rGOMM and ITO electrodes with different device active area.

	Device area (mm^2)	J_{SC} ($mAcm^{-2}$)	V_{OC} (mV)	FF (%)	PCE (%)
rGOMM	4	7.81	848	45.9	3.05
	50	5.44	846	38.9	1.79 (41.1%↓)
	135	3.87	831	33.2	1.07 (64.9%↓)
ITO	4	8.93	864	49.5	3.82
	50	6.31	862	42.5	2.31 (39.5%↓)
	135	4.48	848	36.3	1.38 (63.2%↓)

Another important benefit of the flexible rGOMM electrode on PET substrate is its high durability under extreme bending conditions and its ability to retain its electrical properties. This capability is very important for every flexible electronic device. Indeed, as shown in Figure 3.23c the R_s change upon 90^o bending is negligible, as it does not change more than 8%, while the overall change is ~ 11% up to a bending angle of 135^o. Following the reverse route, the R_s returns near to its initial value, showing a slight increase (less than 2%). This implies that no appreciable change in the TCE structure occurs during bending. This excellent flexibility is advantageous over the conventional ITO, which showed a rapid increase in its R_s value under identical bending conditions (also shown in Figure 3.23c). This behavior can be attributed to the well-reported cracking effect of ITO that gives rise to a catastrophic electrical failure.

An important motivation for using solution-processed rGOMM electrodes is to realize highly flexible OPVs that can be used for compact roll-type solar modules. A similar behavior with above findings is observed in Figure 3.23d where the photovoltaic performance with respect to the device bending history is presented. Indeed, the rGOMM-based device almost retains its initial photovoltaic performance after extreme bending conditions, a result that is highly desired for flexible organic

electronic applications. On the contrary, ITO-based devices showed a remarkable different behavior; the device could operate only up to 45^{o} bending, but with a significant deterioration in its performance, while it is completely destroyed after 90^{o} bending, without the ability of retaining its initial PCE values.

Another important issue investigated in this work was whether our proposed method can be applicable to large area OPV devices (Figure 3.23e-g). This is crucial for the future development of this technology and its subsequent upscaling from single cells to solar modules. For this purpose, rGOMM- and ITO-based devices with increasing active area were fabricated and tested. As it can be clearly observed in Table 4 , the deterioration in the photovoltaic performance measured for both rGOMM- and ITO-based devices was practically the same, i.e., for 135 mm^2 active area PCE reduction measured was 63.2% for ITO and 64.9% for rGOMM, respectively. It can be concluded that the proposed electrode patterning method can be effectively applied to large area photovoltaic cells without compromising the photovoltaic efficiency.

The contribution of our work in the graphene-based TCE technology reported to date is illustrated in Figure 3.26. The figure indicates the PCE values of OPV devices fabricated on solution-processed graphene-based TCE reported in the literature, together with the corresponding values of rGOMM based devices reported here. Devices on rigid as well as flexible substrates are taken into account. It is more than clear that the proposed laser patterning technique produces high quality rGOMM electrodes and could potentially mitigate the lag between graphene-based and ITO-based TCEs.

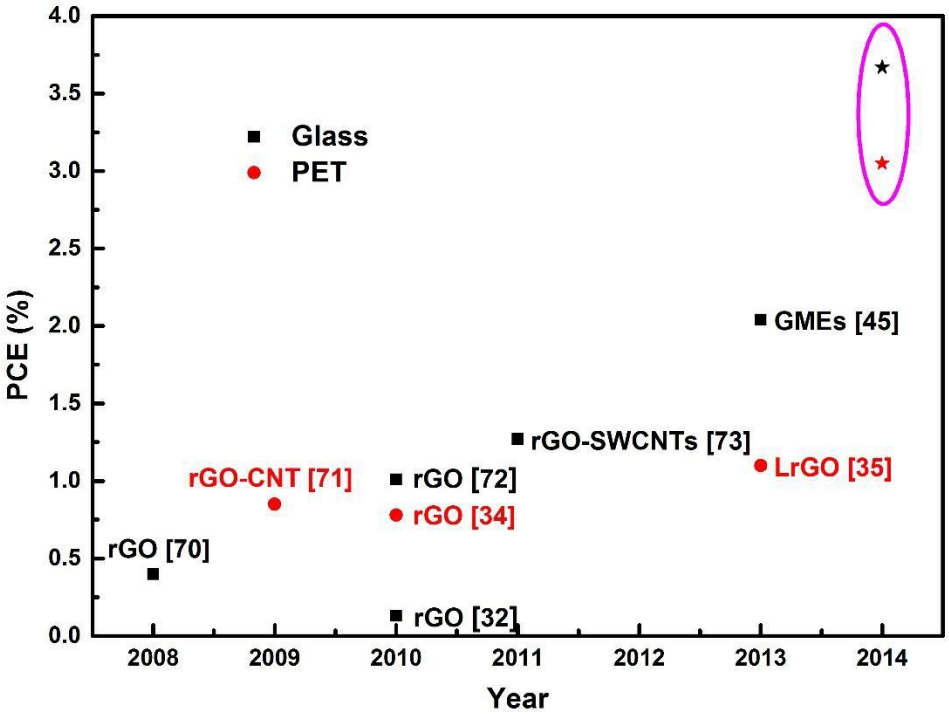

Figure 3.26. OPVs performance of OPV cells based on solution processed graphene-based TCEs reported to date in the literature.58,60,61,45,70,71,72,73 Black squares stand for rigid devices, while red circles for devices on flexible substrates. Stars illustrate the contribution of this work to the PCE improvement.

3.3.4. Conclusion

In conclusion, the successful development of a direct fs laser writing technique to fabricated pattern rGO mesh TCEs has been demonstrated. The technique enables the accurate control of rGO micromesh geometrical features on top of rigid (glass), as well as flexible (PET) substrate. As a result, the conductivity and transparency of the treated rGO films can be finely tuned and tailored for the specific application. Using this technique, it is shown that rGO electrode transparency can be readily changed from ~ 20% to up to ~ 85%, with only a slight increase in the respective R_s value. To demonstrate the application and the potential applicability of the proposed technique in the field of flexible transparent electronics, OPV devices that host the laser-induced rGOMMs films as the TCE electrode were fabricated, exhibiting superior performance compared to the ones that incorporate pristine rGO TCEs. The devices displayed a PCE of 3.05%, which is the highest reported to date for flexible OPV

devices incorporating solution-processed graphene based electrodes. Due to their chemical stability, mechanical flexibility, high transparency, and conductivity, along with their scalable production through solution processing and subsequent laser patterning, rGOMMS are excellent potential candidates for a wide range of new applications with tunable optoelectrical properties, including flexible electronic OPVs, perovskite solar cells, organic light emitting diodes, and photosensors, as well as traditional electronic devices based on rigid substrates.

Chapter IV: Laser fabrication of TMDs based nanomaterials

4.1. Short Pulse Laser Synthesis of Transition Metal Dichalcogenide Nanostructures in Ambient Conditions

The study of inorganic nanometer-scale materials with hollow closed-cage structures, such as inorganic fullerene-like nanostructures (IF) and nanotubes (INT), is a rapidly growing field. Numerous kinds of IF and INTs were synthesized for a variety of applications, particularly for lubrication, functional coatings and reinforcement of polymer matrices. To date, such nanostructures have been synthesized mostly by heating a transition metal or oxide thereof in the presence of precursor gases, which are however toxic and hazardous. In this context, one frontier of research in this field is the developement of new avenues for the green synthesis of IF structures and INTs, directly from the bulk of layered compounds. In the present work, we demonstrate a simple room temperature and environmentally friendly approach for the synthesis of IF and INTs via ultrashort pulse laser ablation of a mixture of transition-metal dichalcogenides in bulk form mixed with Pb/PbO, in ambient air. The method can be considered as a synergy of photothermally and photochemically induced chemical transformations. The ultrafast laser induced excitation of the material, complemented with the formation of extended hot annealing regions in the presence of the metal catalyst, facilitates the formation of different nanostructures. Being fast, easy and material independent, our method offers new opportunities for the synthesis of IF and INTs from different bulk metal chalcogenide compounds. Based on the capabilities of laser technology as well, this method could be advantageously be further developed into a versatile tool for the simultaneous growth and patterning of such nanostructures in preselected positions for a variety of applications.

4.1.1. Introduction

Since the discovery of the nested inorganic fullerene-like structures (IF-NPs) and inorganic nanotubes (INTs) of WS_2 and MoS_2 [73,74], by heating thin metal films of W and Mo in the presence of gaseous H_2S, a whole new field opened up with opportunities in research and applications. The multilayered two-dimensional elements are unstable in their microscopic form and spontaneously form closed structures with a hollow core. Layered materials formed from inorganic elements are abundant. In bulk form, these structures appear as platelets, wherein each platelet is composed of molecular slabs held by weak van der Waals forces. Typical examples of such structures from tungsten disulfide (WS_2) and molybdenum disulfide (MoS_2) were reported in numerous works. TMDs are trilayer X-M-X sandwiches where X = S or Se and M = a transition metal. Besides those, numerous fullerene-like NPs and INTs were synthesized through the years from different layered structure materials, including BN[286], TaS_2[287] and $NiCl_2$[288] and ternary layered (misfit) compounds[289]. Owing to their remarkable properties, many studies have focused on the stability and the structure[110,97,290,118] of the IF-NPs and INTs of WS_2 and MoS_2 in addition to their significant mechanical, optical and electronic properties[291]. As a result, IF nanostructures from WS_2 and MoS_2 have been effectively used and commercialized in various potential applications, particularly as solid lubricants[292]. In addition, numerous applications for these nanoparticles have been proposed, including in reinforcing polymer nanocomposites[293], nanoelectronics[294], energy production[295] and storage[296]. Besides this, the non-toxic nature of such materials, as has pointed-out by several works[297,298,299], is a prime motivation for medical applications[300]. The growth mechanism of these structures has become a highly explored topic for many researchers[301,75,302,107,303]. One can distinguish between two main research strategies: (a) high-temperature synthesis under chemically controlled atmosphere, and (b) using energy burst to ablate powder and induce a reaction under far from equilibrium conditions. The studies in (a) were mostly based on the reactions of hydrogen and hydrogen sulfide or sulfur-containing vapors with metal-oxide nanoparticles or another metal precursor at typical temperatures between 500-1000 °C. These conditions allow for the synthesis of metastable phases of MX_2 not far from

equilibrium conditions. The most common synthesis method in large-scale production of the IF-NPs and INTs is the sulfidization of the metal oxides under reducing conditions[304,107,305]. Here the reaction parameters can be modified and controlled systematically, enabling the mass production of IF and INT of WS_2 as well as MoS_2 for a variety of applications. On the other hand, reactions in the category (b) occur far from equilibrium conditions and cannot be easily controlled. Despite the great success with the production of single wall carbon nanotubes and C_{60}, these methods have not been well developed for their inorganic analogues, so far. Fortunately, this kind of reactions opens windows of metastability not accessible for the thermally induced reactions of (a). An excellent proof of concept was the first synthesis of MoS2 nanooctahedra, which were dubbed the "true inorganic fullerenes"[306]. In this context, different approaches were used by several research groups, such arc discharge[307,308], shock waves[309,310] solar ablation[306] and laser ablation[97,98], which yielded remarkable results. Another interesting approach was presented recently[96] utilizing a focused solar beam and a growth promoter in the form of a heavy metal. The beam is generating continuous extreme temperatures exceeding 2500 °C and temperature gradients (103 K/mm) in the presence of a metal catalyst (Pb), which lead to the formation of various inorganic nanotubes. The presence of the metal catalyst seems to promote the growth of new hybrid structures with metal core-semiconductor shell.

Furthermore, although considerable research has been devoted to the large-scale synthesis of IF and INTs nanostructures, less attention has been paid to avoiding the use of toxic and hazardous gases such as H_2S and H_2. Hence, the development of a more environmentally friendly synthetic method remains a challenge.

In this context, we demonstrate here a new synthesis path towards fullerene-like NPs and INTs from the bulk, via ultrafast laser ablation in ambient air (**Figure 4.1**).

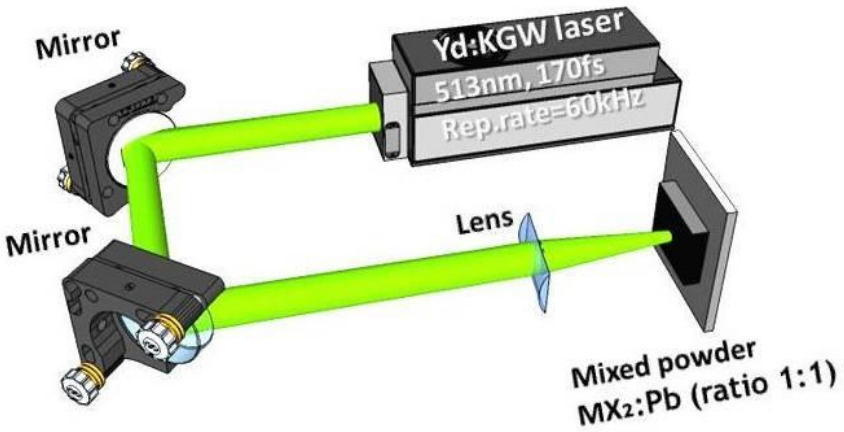

Figure 4.1 Schematic of the experimental setup used for the laser synthesis of TMD nanostructures under ambient conditions.

Contrary to previous laser ablation approaches[97,98], our method does not require inert conditions. The ultrafast laser induced excitation and ablation of the irradiated material leads to extreme temperatures and heat gradients, enabling the synthesis of metastable MX_2 phases in highly non-equilibrium conditions. Accordingly, this method provides the potential for the synthesis of nanostructures that cannot be attained by conventional synthetic routes. This technique is fast and does not require the use of hazardous precursor gases and thus expensive equipment. Not less important is the possibility for, on-demand, simultaneous growth and patterning of nanostructures in preselected locations. Finally, it is a material independent technique and thus can be further extended for the direct synthesis of other TMD nanostructures.

4.1.2. Experimental

Sample preparation and the laser ablation

MoS_2 (or WS_2) powder was mixed with Pb powder, as the metal catalyst, in a 1:1 molar ratio (11 gr each). Substrates of Al were sonicated in ethanol for 10 min. By using silver paint, the mixed powder was attached to the Al substrate. Pulsed laser ablation of the sample was performed in ambient air. A second harmonic Yb:KGW

laser (513nm, pulse duration 170fs, pulse repetition rate 60 kHz, fluence = 5,3 W/mm^2) was used for these experiments. The sample was mounted on a computer controlled motorized X – Y translation stage. During the irradiation, the sample was scanned in two orthogonal directions (X and Y) in a fully controlled manner across the focused laser beam in several spots in duration 1min each. The estimated number of laser pulses per each irradiation spot is $3.6x10^6$. A schematic of the experimental set up is shown in **Figure 4.1**.

Electron microscopy

The samples were examined by different electron microscopy techniques. Scanning electron microscope (JEOL 7000) equipped with an energy dispersive spectrometer (EDS-INCA PentaFET-x3) was used for the analysis of the samples. Transmission electron microscopy (TEM) was carried out with a Philips CM-120 instrument operating at 120 kV equipped with an energy-dispersive X-ray analyzer (EDS). High-resolution TEM (HRTEM) was performed with an FEI Technai F30-UT microscope operating at 300 kV. All powders that were analyzed by electron microscopy were dispersed in ethanol, using an ultrasonic bath, and the suspension was dripped on lacey carbon/Cu grids.

4.1.3. Results and Discussion

Scanning electron microscopy (SEM) images revealed that laser irradiation of MoS_2 gives rise to nanowhiskers and IF-NPs, while that of WS_2 yields INTs. For MoS_2 in particular, the irradiating powder is comprised of MoS_2 platelets (Figure 2a) decorated with nanowhiskers, with no indication of nanotubes.

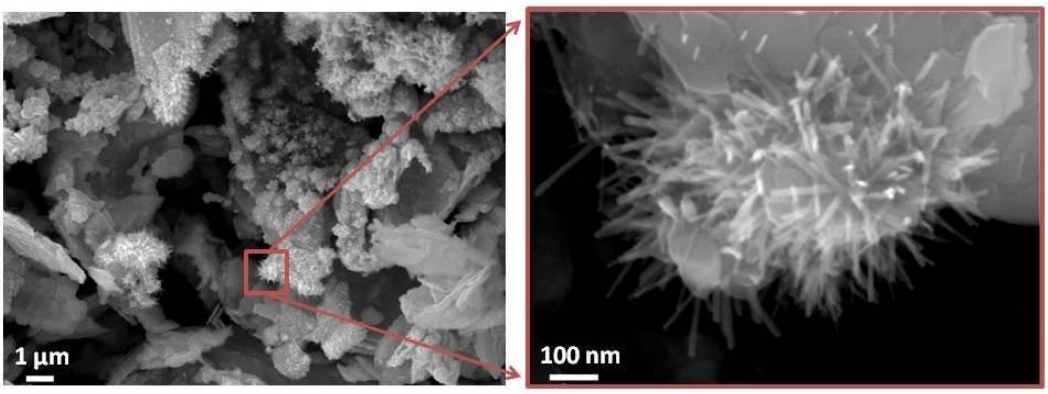

Figure 4.2: SEM imaging of MoS_2 NPs.

A closer inspection with TEM revealed interesting faceted IF-NPs, co-located in the same area with nanowhiskers, with sizes ranging between 80 and 200 nm, as presented in Figure 3a and b. The layered structure of the walls forming such NPs can be clearly resolved in the respective images. The inset of Figure 3c represents the line profile with the measured interlayer distance to be 0.61 nm, which corresponds to the interlayer distance (c/2) of MoS_2. While some of the IFs produced appear as having a hollow core, others seem to have a darker contrast inside their interior. Nevertheless, the EDS measurements performed on single particles consistently gave an almost perfect 1:2 Mo and S ratio as presented in the inset of Figure 3d. Besides this, the amount of oxygen was negligible, so the possibility of a core composed out of oxidized molybdenum or pure molybdenum can be discarded. Furthermore, the undistorted Mo to S ratio points to a MoS_2 core.

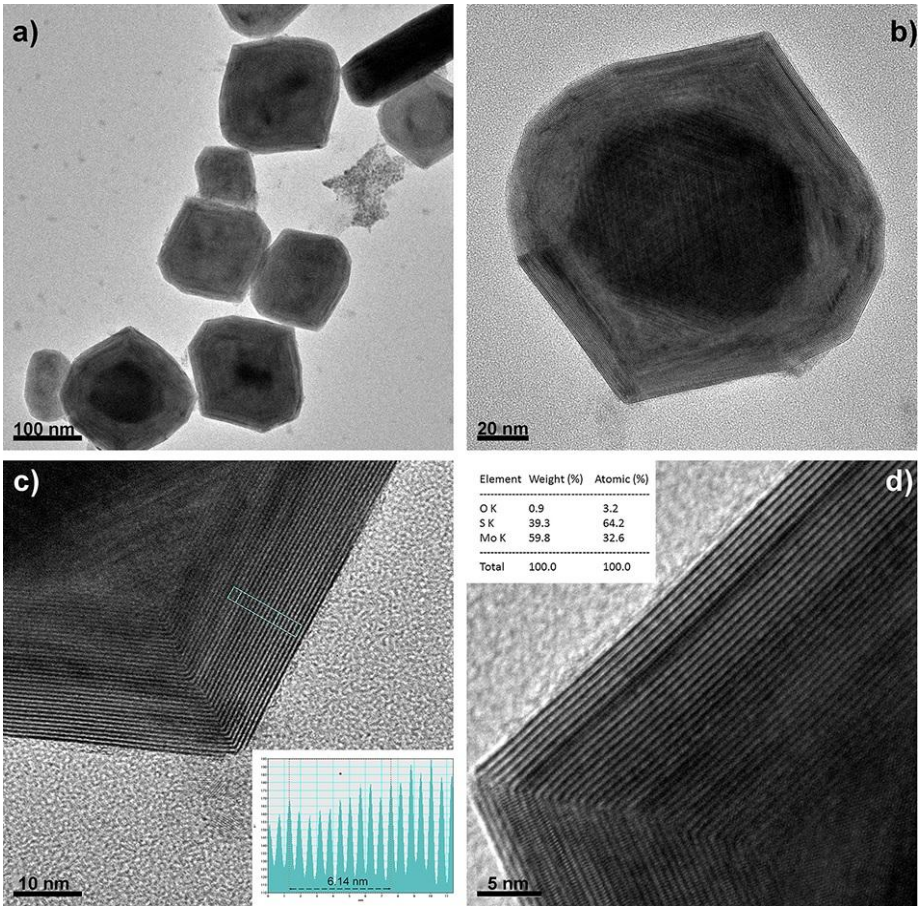

Figure 4.3: TEM analysis of IF-MoS_2 NPs: (a) an assembly and (b) a single IF-MoS2 NP. (c, d) Line profile and EDS measurement, respectively, performed on a single particle.

HRTEM imaging, as shown in Figures 4a and 4b, also revealed sharp edges and corners of these nanoparticles with distinct fringes, while the internal structure begins exactly where the layers end. This indicates the inside-out growth mechanism where a small MoS_2 (nano)platelet serves as a template (growth nucleus), which is subsequently sheathed layer by layer upon irradiation.

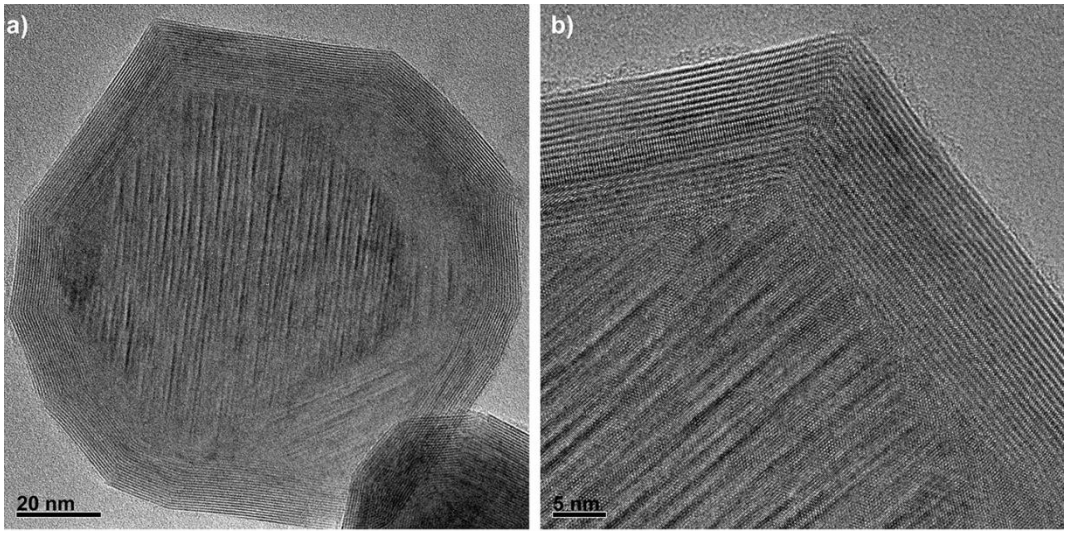

Figure 4.4: HRTEM analysis of IF-MoS_2 NPs: at low (a) and high (b) magnifications.

Figures 5 and 6 represent TEM images of the sharp corner and a faceted edge, respectively, at different tilt angles. The feature in Figure 5 is virtually unaltered as the tilt angle changes from -20° to +20°; this observation confirms that the imaged feature is a sharp corner. On the other hand, Figure 6 shows a faceted edge which appears as more rounded at negative angles, while it changes into sharper edges upon tilting to +20°.

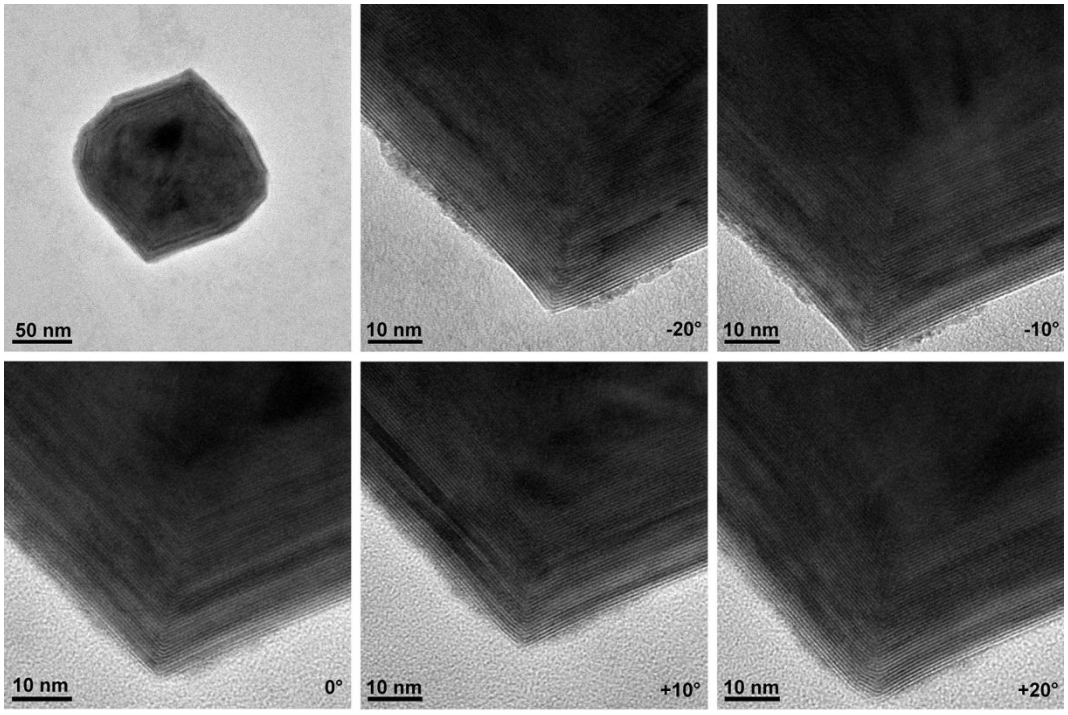

Figure 4.5: TEM tilting experiment of an IF-MoS2 NP, focused on a sharp corner.

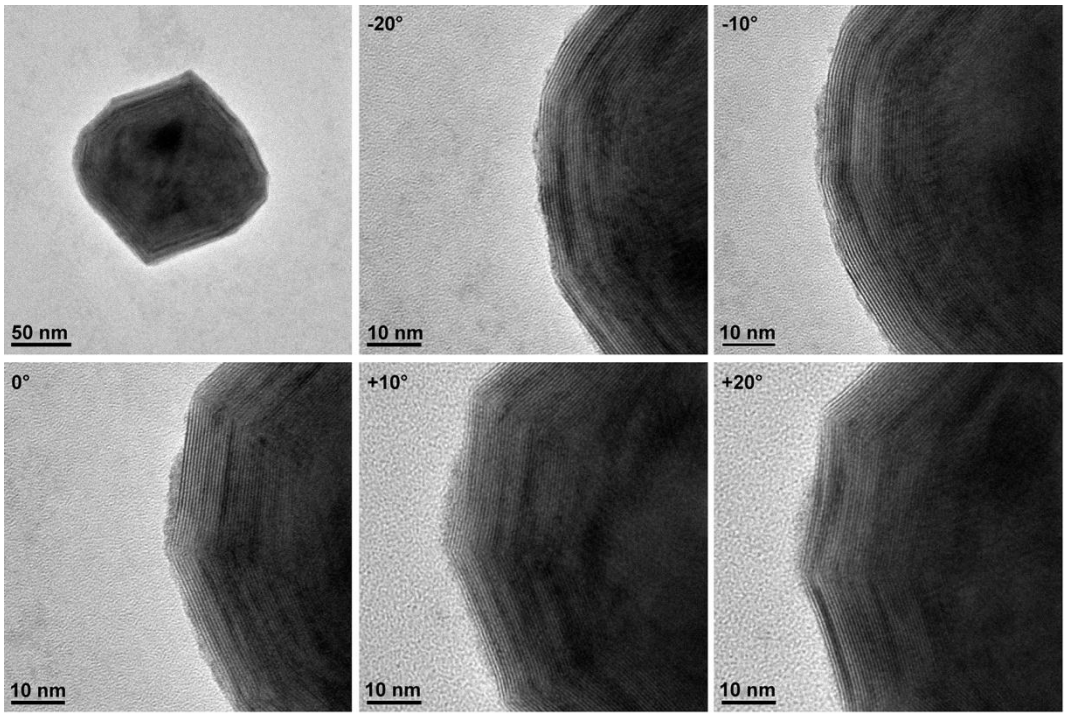

Figure 4.6: TEM tilting experiment of an IF-MoS2 NP, focused on a faceted edge.

On the other hand, SEM imaging of the irradiated WS_2 powder revealed that INTs are growing from WS_2 platelets (Figures 7a-7d). The nanotubes' dimensions ranged from 20 nm to 100 nm in width and were approximately 1 μm in length. It can be observed that the outermost surface of the exposed platelets appears to be completely covered by INTs. The mild sonication procedure used for preparation of TEM grids detaches the INTs from the platelets, leaving one of the edges open while the other is usually closed.

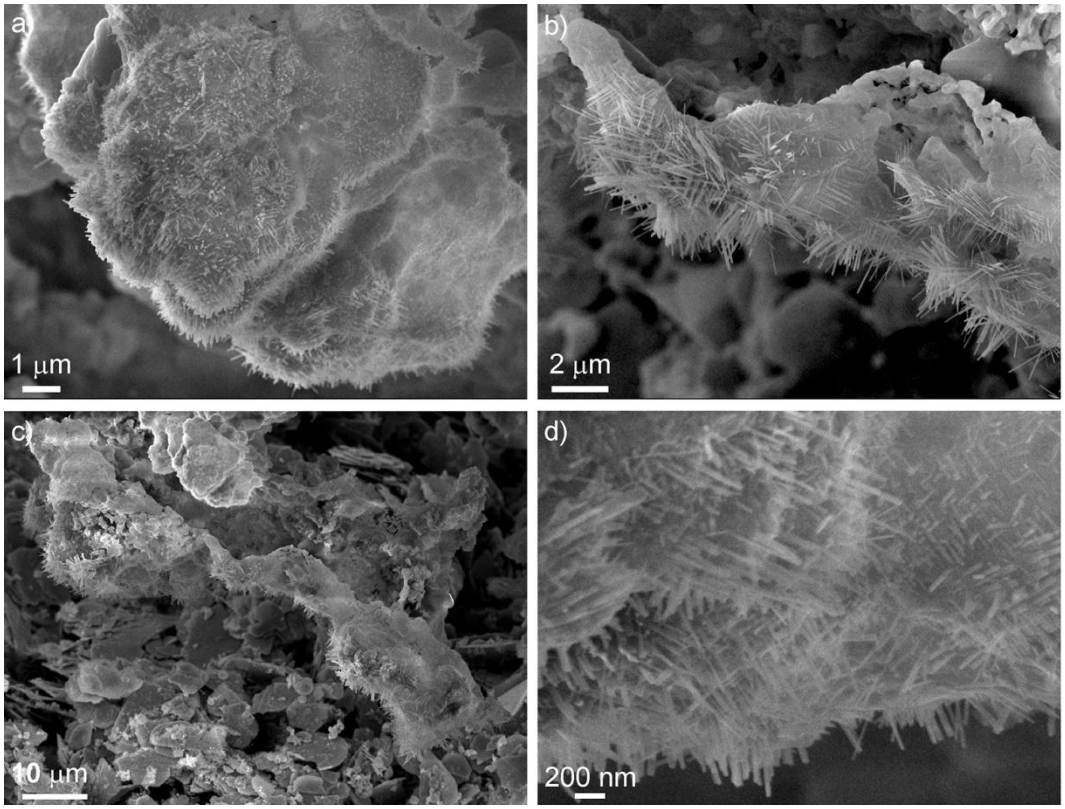

Figure 4.7: SEM imaging of WS_2 nanotubes protruding from the platelets: at low (a−c) and high (d) magnifications.

A representative WS_2 nanotube is presented in the TEM image of Figures 8a and 8b. The interlayer spacing, as shown in the inset of Figure 8a, is close to 0.625 nm, which is slightly larger than the distance between the two neighboring layers of WS_2 (c/2= 0.62 nm). Moreover, it was observed that some of the INTs synthesized exhibited hollow core, while the rest were filled with material.

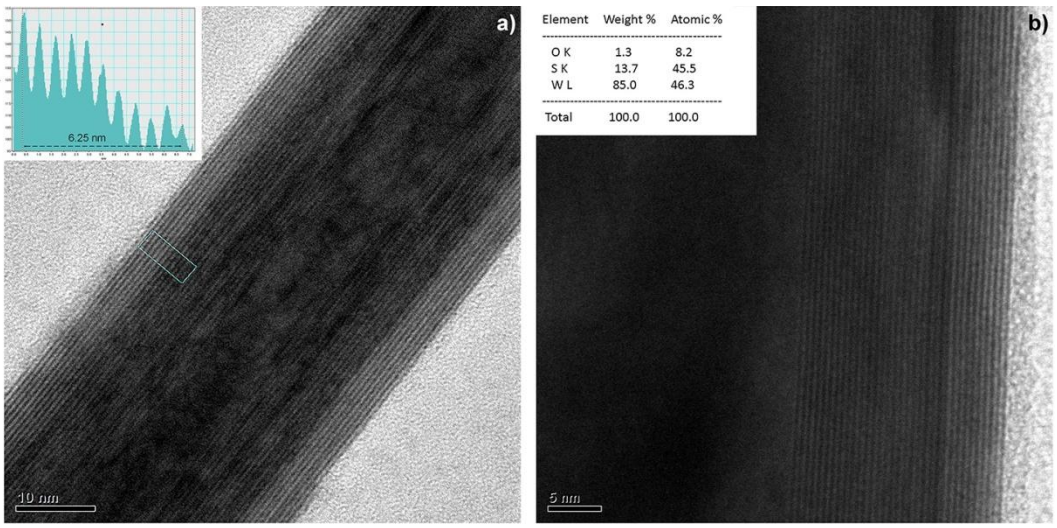

Figure 4.8: TEM analysis of WS_2 nanotubes. The insets show the (a) line profile and (b) EDS measurement performed on a single nanotube.

Since the number of layers on both sides of INTs is the same, as shown in Figure 4.9a and 4.9b, it is possible that the core is made through aposteriori filling of the pre-prepared nanotubes.

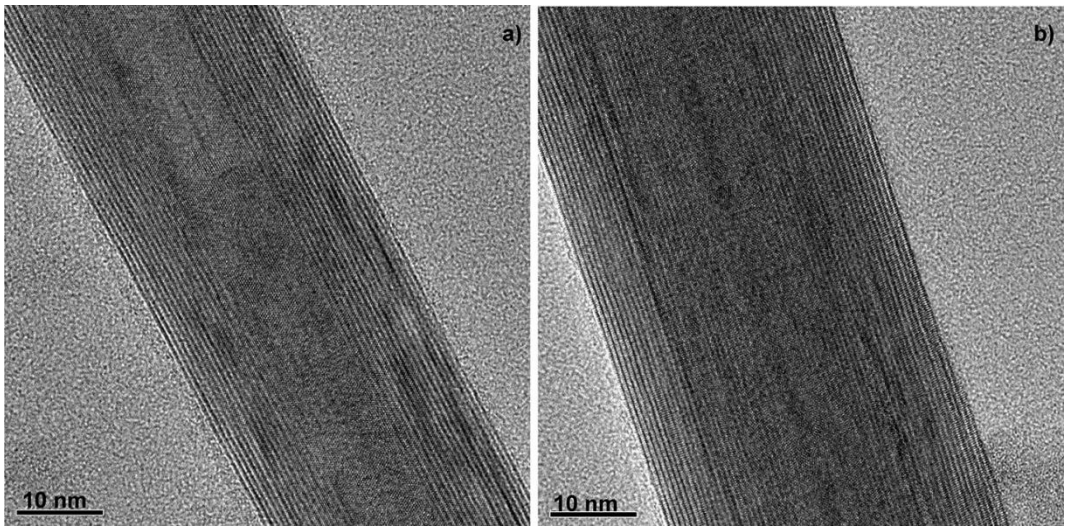

Figure 4.9: HRTEM of WS_2 nanotubes with (a) filled and (b) hollow cores.

In analogy to the case of the previously discussed IF-MoS_2 NPs, the amount of oxygen found in the laser-synthesized INT-WS_2 was negligible. On the contrary, EDS analysis of the W to S ratio was found to be approximately 1:1, in all cases as shown in the inset of Figure 8b. There can be several explanations for this phenomenon. Most likely, since W is much heavier than both Mo and S, the count rate is rather low. Hence, the deviations of the model calculations for the atomic %, that are extracted directly from the detector, are larger. Additionally, this analysis takes into account only specific lines (the K line for sulfur and the L line for tungsten). Although these are the predominant ones, including the other lines may change the W to S ratio. On the other hand, the existence of the core may be attributed to its filling with excess sulfur.

The first question arising from the experimental findings presented here is the role of lead on the synthesis of the inorganic nanostructures. Back in 2012, MX_2 (M=Mo,W; X=S,Se) nanotubes were produced by solar ablation of the respective

powder in the presence of lead. In fact, according to the proposed growth mechanism, the originally ablated MX2+Pb power was first converted into MO_{3-x} nanowhiskers. The lead atoms were incorporated into the MO_{3-x} lattice making it more stable and promoting the growth of a nanowhisker[96]. Further irradiation of the nanowhiskers in the presence of the chalcogenide vapor lead to back-conversion of the metal oxide into MX_2 nanotubes. More recently, core-shell nanotubes and fullerene-like structures of Pb@GaS were obtained via solar ablation of the mixed powder[311]. In this work, GaS layers wrapped the Pb nano-template conformably producing such intriguing nanostructures. In contrast to these cases, no lead was found within or in the vicinity of the IF/INT MoS_2/WS_2 nanostructures produced via the laser ablation approach presented here. It can therefore be concluded, that the presence of lead may not play any direct significant role in the production of the nanostructures reported here; further experiments are currently in progress to further confirm the insignificant role of lead. Nevertheless, no IF/INT were produced by laser ablation of Pb-free powder. Therefore, the comprehensive role of Pb in the synthesis is not fully understood at this time and requires further investigation.

Surprisingly, the same reaction conditions yield substantial amounts of hollow closed structures of MoS_2 and WS_2, but yet with dissimilar morphology. While, the outcome of the ablation of MoS_2 powder are fullerene-like NPs with acute corners, multiwall nanotubes are the main product of the WS_2 powder ablation. On the one hand it points out to the robustness of these nanostructures, which have been previously attained using different chemical strategies. The difference in the reaction products between MoS_2 and WS_2 is possibly a manifestation of the differences in their chemical stability. In the particular case of MoS_2, the ablated plum undergoes rapid oxidation under the intense laser flux in air, while the resultant oxide is rather volatile. Therefore, the IF-MoS_2 NPs have possibly been formed at the pristine surface left behind the ablated material. It should be emphasized here that the intense laser beam excites a large density of electrons, which eventually give rise to excess heat upon transferring of their energy to the lattice via phonons. Additionally, these photoexcited electrons can also provide a reducing local atmosphere on the surface of the ablated sample. Thus, the ablated MoS_2 plume, which resides in close vicinity to the powder surface is protected against oxidation and can contribute to the buildup of the IF-MoS_2 nanoparticles. On the contrary, WS_2 is chemically more stable and does not oxidize as easily as MoS_2. Therefore, the WS_2 ablation plume is likely to be rich

in WS_x vapor, which condenses back onto the mother tip of the tube protruding from the powder crystallites' surface. Experiments are under progress to monitor the evolution of each kind of nanostructure upon variation of the irradiation parameters.

Large amounts of pure WS_2 nanotubes' phases were obtained in the past by reacting WO_{3-x} and H2S at temperatures as high as 800-900 ^{o}C. Several growth mechanisms have been proposed and consequently a distinction was made between Type I and II[109] formation processes. In the case of Type I, the nanotubes grow spontaneously in high rate. Conversely, in Type II process, WO_{3-x} nanowhiskers grow first and are subsequently substituted chemically into WS_2 nanotubes. This process is rather slow (it takes a fraction of an hour) and is possibly not relevant to the present experimental conditions. While, Type I tubes are narrow (up to 40 nm), made of up to 10 walls and are open ended, Type II ones exhibit large diameters (50-150 nm), are usually longer (2-20 microns) and usually have closed tip. In the production process presented here, the situation is quite different. The ultrashort pulses are heating the lattice via a photothermal process, but at the same time provide the energy to photochemically break the chemical bonds between W and S and ablate the WS_2 moieties[312], which subsequently give back the energy to the environment and condense (Figure 10). This rapid process is analogous to the Type I nanotubes growth. As expected, no oxide core was identified in the analysis. Furthermore, as shown in Figure 7b, the tubes form a forest protruding perpendicular to the substrate and exhibit quite uniform length. This growth mode indicates an abrupt supply shortage of the plume, possibly via rapid energy loss to the environment, once the nanotubes reach a critical length. Although Type I nanotubes are mostly grown under the conditions used, TEM analysis revealed the presence of a fraction of Type II nanotubes in the ablated area. A direct comparison of the two types is presented in Figure 9; indeed, the nanotube shown in Figure 9a is akin to Type I (few layers and large diameter core), while that in Figure 9b is closer in shape to Type II (many layers and narrow core).

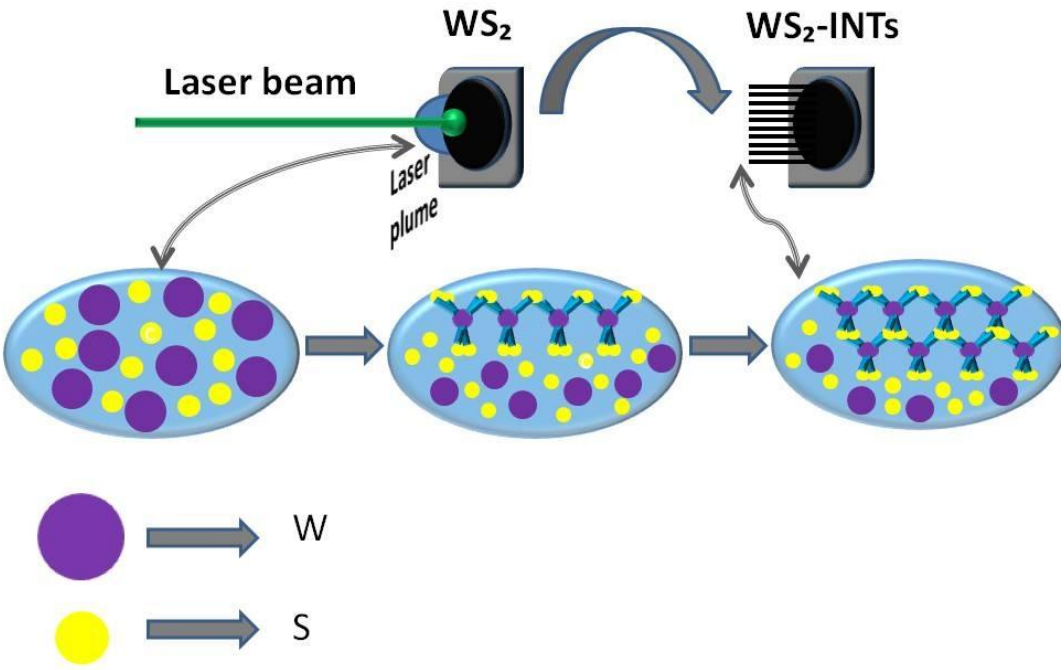

Figure 4.10: Schematic process of obtaining WS_2 nanotubes through ultrashort laser pulses from the respective powder.

Furthermore, it was observed that the nanotubes with large diameter mostly exhibited a closed tip, while the narrower ones showed an open tip. It can be concluded that the highly excited state conditions formed under ultrafast laser excitation and subsequent ablation give rise to growth processes, which are not necessarily relevant to that observed in high-temperature oven-induced reactions. Nonetheless, our finding that WS_2 nanotubes of similar structure can be produced, in similar or even higher yields compared to the alternative approaches, under such entirely different conditions, is indicative of the robustness of this structural motif.

4.1.4. Conclusion

The synthesis of WS_2 and MoS_2 nanostructures through ultrashort pulse laser irradiation of the bulk material in ambient conditions is demonstrated. It is shown

that, while this method produces nanotubes in the case of WS_2, irradiation of MoS_2 under identical conditions leads to IF NPs. The presented method is performed in ambient air and without use of any toxic precursor gases, making it a simple and environmentally friendly approach to obtaining high-quality inorganic nanostructures. Our results suggest that one can use a scanning laser beam for the formation of inorganic nanostructures at any preselected location and on temperature sensitive plastic substrates, which is destined to numerous applications, including formation of miniaturized electronic devices or tips for electron emission and scanning probe microscopy.

4.2 Pulsed laser growth of TMDs nanostructures

Introduction

In this section the application of the pulsed laser deposition technique (PLD) for the growth of hierarchical TMD structures, specifically the formation of WS_2 nanostructures onto microstructures. These techniques can be further developed for the formation of hierarchical TMD structures at any preselected location which are desirable to numerous applications, including field emission cathodes and scanning probe microscopy electron emitters. [144]

Pulsed laser deposition (PLD) is a physical vapor deposition technique, which utilizes the high-power of a pulsed UV laser beam to ablate material from a target and deposit in onto a substrate. The technique uses high power laser pulses to melt, evaporate and ionize material from the surface of a target. This "ablation" event produces a transient, highly luminous plasma plume that expands rapidly away from the target surface. The ablated material is collected on an appropriately placed substrate upon which it condenses and the thin film grows. The procedure is facile and the irradiation takes place under high vaccum.

Experimental

WS_2 targets were prepared by pressing 1gr of 99% WS_2 Sigma Aldrich in a 13mm dye at room temperature for 2 min at 4 metric tons. Pulsed laser ablation of solid WS_2 pellets was performed in a high vaccum $2x10^{-6}$ mbar with a KrF excimer laser (248nm, 20ns, pulse repetition rate 10 Hz) in the presence of Ar carrier gas. The laser spot size is adjusted via a movable focusing lens, while the laser energy density is controlled by an optical attenuator. A series of experiments were performed by changing the parameters that have strong influence on film properties, including the substrate temperature (varied between 500 to 600 ^{o}C), the target-to-substrate distances (varied from 2 to 5 cm) as well as the laser fluence (ranging from 2 to 5 J/cm^2) and

number of laser pulses (ranging from 1000 to 10000). The substrate used in all cases comprised arrays of Si microspikes (height of 10 μm, radius of curvature of 700 nm) fabricated using laser ablation of Si in SF_6 atmosphere.

All the samples were examined by scanning and transmission electron microscopy, as well as with Raman and XRD spectroscopy. In particular:

Electron microscopy: Scanning electron microscope (JEOL 7000) equipped with an energy dispersive spectrometer (EDS-INCA PentaFET-x3) was used for the analysis of the samples. Transmission electron microscopy (TEM) was carried out with a Philips CM-120 instrument operating at 200 kV.

Spectroscopy: Raman spectroscopy was performed using a Nicolet Almega XR Raman spectrometer (Thermo Scientific) with a 473 nm blue laser as an excitation source. X-ray diffraction spectroscopy was performed using a D/MAX-2000H.

Results and discussion

SEM imaging revealed the remarkable formation of TMD nanowalls decorating the microspikes (Figure 4.12). Further analysis was carried out in order to identify the optimum conditions for producing these nanostructures.

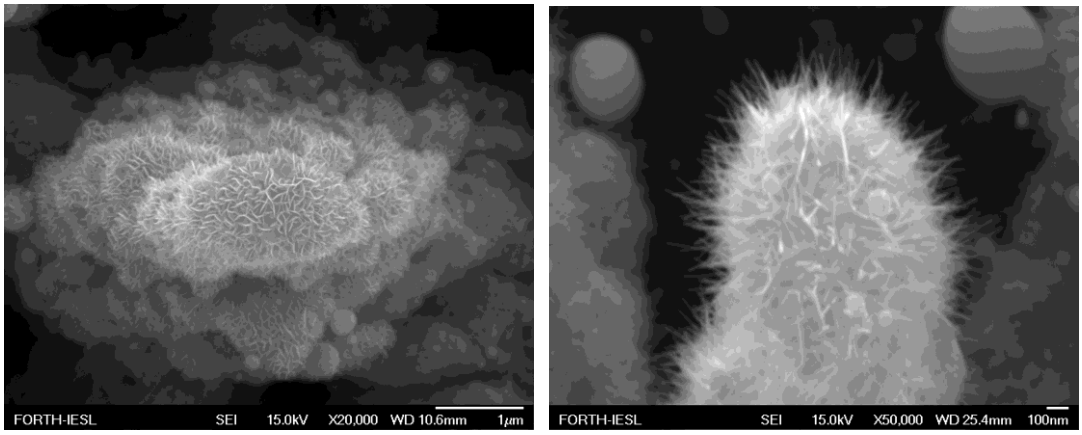

Figure 4.12: SEM images of WS_2 nanowalls decorated on spikes substrate

The corresponding film thickness was always measured from cross-sectional SEM images, as demonstrated in Figure 4.13.

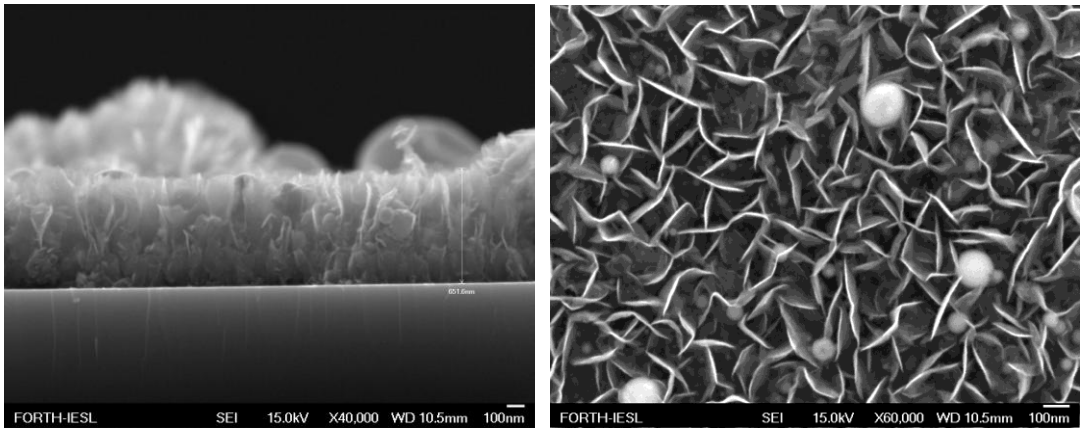

Figure 4.13: SEM cross-section of WS_2 film, used to define the as-grown film thickness.

The length of the nanowalls can be tuned upon changing the laser fluence, the substrate temperature and the target to substrate distance (Figure 4.14). In particular, in the case of constant substrate temperature and fluence we observed that the length of nanowalls decreases when the distance of the target to substrate increases (Fig. 4.14 a). On the other hand, for a certain substrate temperature and target to substrate distance, the length of the nanowalls increases as the fluence increases (Fig. 4.14 b). Finally for a certain laser fluence and a target-to-substrate distance, the length of the nanowalls increases until the substrate temperature reaches 600 ^{o}C and then decreases as the substrate temperature further rises (Fig. 4.14 c).

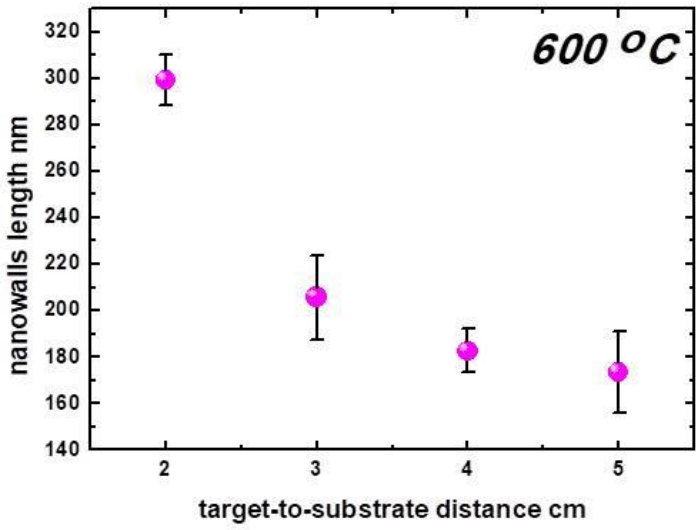

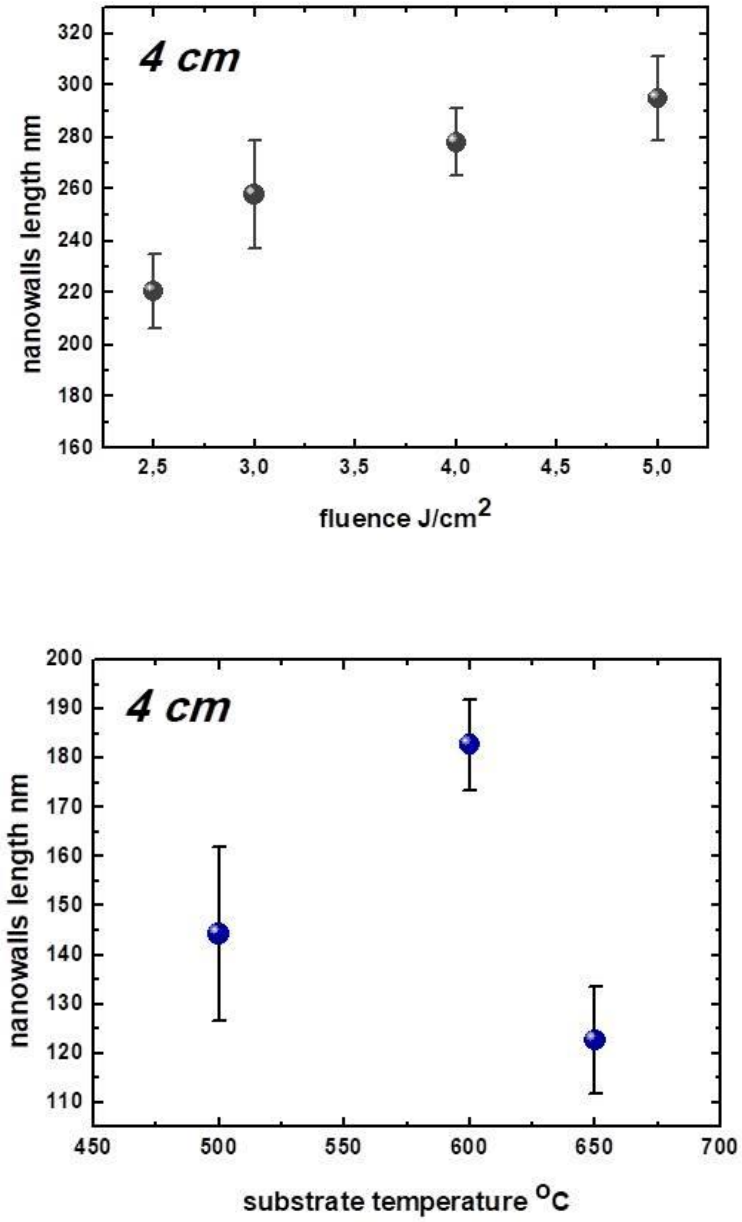

Figure 4.14: Parametric study has been performed by changing the distance of the target to substrate, the fluence and the temperature of the substrate.

EDS analysis of the W to S ratio was found to be approximately 1:1, in all cases. A closer inspection with TEM (Figure 4.15) revealed the synthesis of IF nanoparticles. The interlayer spacing, as shown in the figure is close to 0.64 nm, which is larger than the distance between the two neighboring layers of WS_2 (c/2= 0.62 nm).

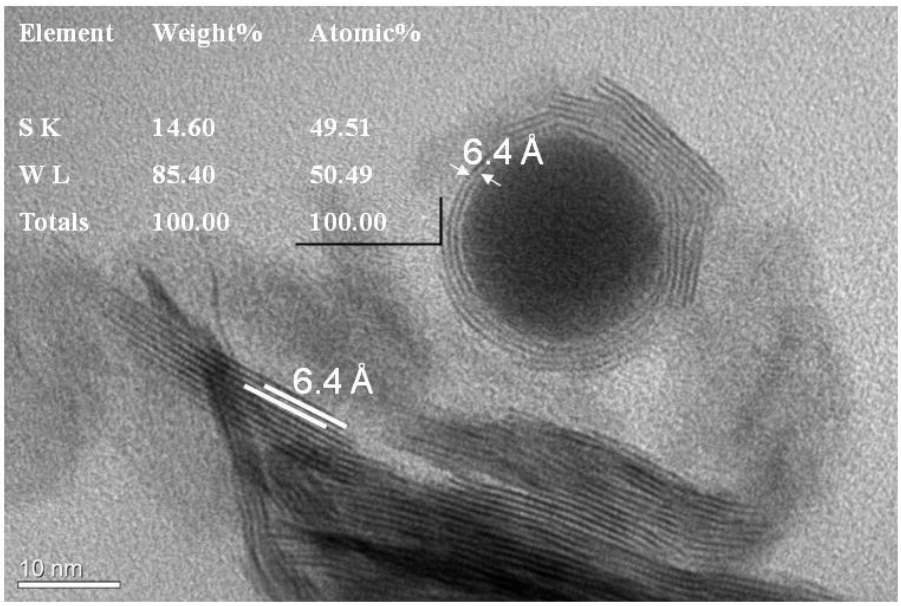

Figure 4.15: TEM analysis of WS_2 nanowalls and particles

Further analysis is performed via Raman spectroscopy (Figure 4.16a) All spectra showed the two prominent E_{1g} (at 355 cm^{-1}) and A_{2g} (at 420 cm^{-1}) bands, associated with the in-plane and out-of plane modes respectively of bulk WS_2. Comparing with the initial powder of WS_2, the bands become more broadened, (Figure 4.16b) particularly as the target-to-substrate distance decreases.

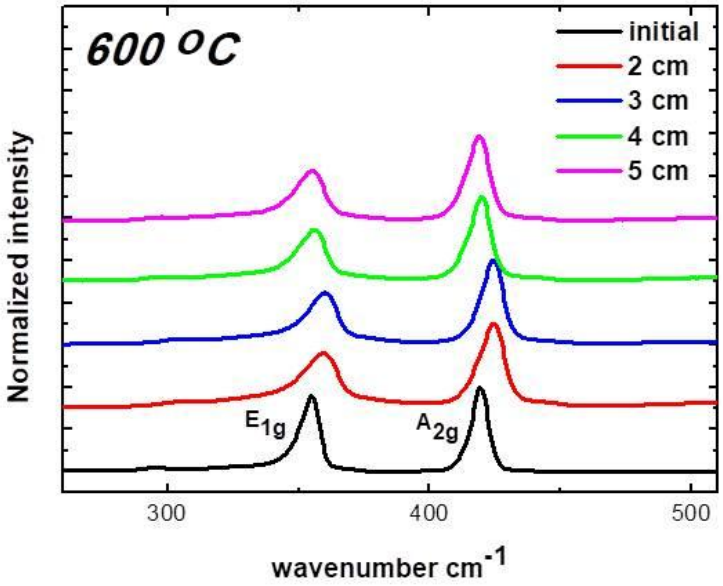

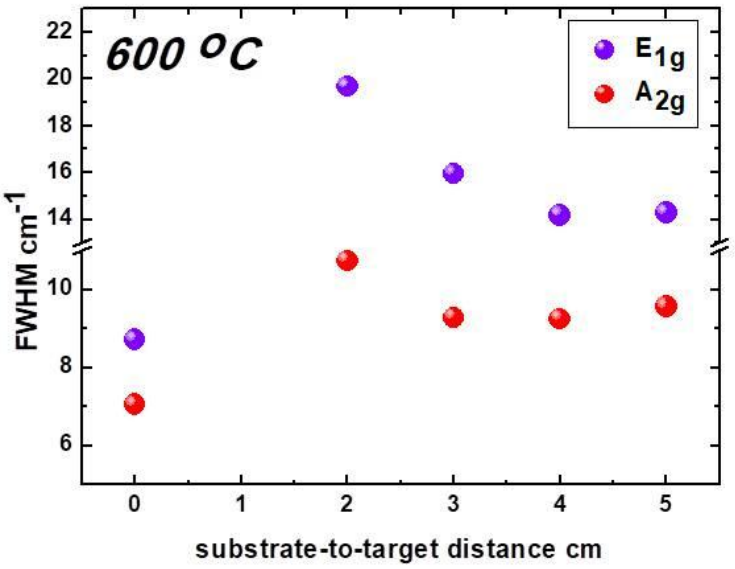

Figure 4.16: Raman measurements at a constant fluence and temperature and a varying distance of target to substrate

XRD measurements were additionally carried out to investigate the crystallinity of the as grown nanostructures, as demonstrated in Figure 4.17.

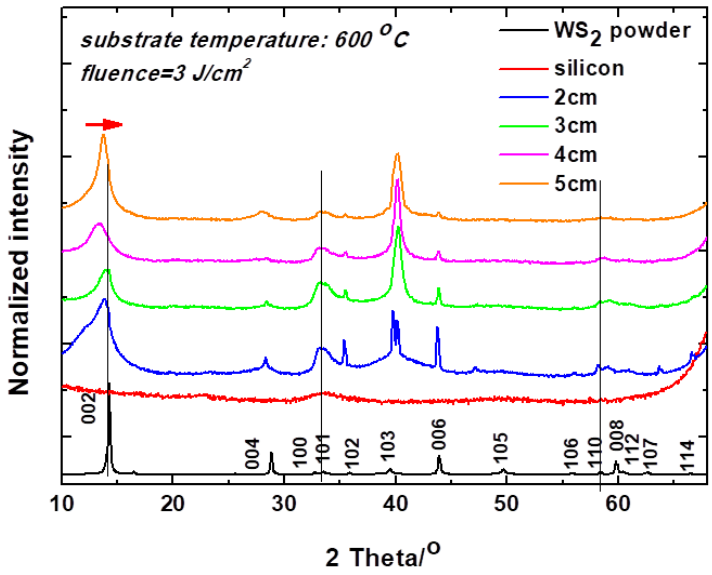

Figure 4.17: XRD measurements of the initial WS_2 powder as well as of the PLD grown TMD nanostructures at different target to substrate distances shown in the inset.

Chapter V: Summary and future work

In the first chapter of this thesis we have introduced the theoretical background of the graphene based and transition metal dichalcogenide nanomaterials. Dimensionality was emphasized and the ability of the same chemical element to exhibit different properties depending on whether it is arranged 0D, 1D, 2D or 3D crystal structure. In the end of that chapter the motivation of this thesis was presented. In particular, the development of simple techniques for the reduction of graphene oxide lattice and controllable doping of graphene, as well as the development of a more environmentally friendly synthetic methods for low dimensional transition metal dichalcogenide materials.

In the second chapter, the experimental setups that were developed as well as the characterization techniques employed during this thesis were presented. Specifically the laser in-situ photothermal reduction and doping of GO was demonstrated. Moreover the laser ablation on solid TMD targets in ambient air as well as in vaccum using the PLD technique were presented. Results on previous reports on Raman, XPS and XRD analysis of graphene and TMD nanostructures were additionally shown.

Chapter three was divided into three different subchapters, each one containing a separate project that was carried out during this thesis and based on the laser assisted fabrication of graphene based nanomaterials for opto-electronic devices. In the first subchapter a photochemical method for the simultaneous reduction and doping of GO layers through ultraviolet laser irradiation in the presence of a dopant precursor gas was presented. To demonstrate the potential of the approach for practical applications, the photochemical method was successfully employed for the in situ laser induced modification of prefabricated GO field effect transistors. In the second subchapter, a fast, non-destructive and r2r compatible photochemical method for the fabrication of chlorinated graphene oxide (GO-Cl) films with an increased WF of 5.23 eV was presented. In the third subchapter, a simple laser-based technique developed to improve and simultaneously tune the optoelectronic properties of graphene based TCEs, is presented. Taking advantage of the rGO solution processability and chemical stability, rGO micromeshes were patterned on flexible substrate and incorporated in as TCEs in OPV devices.

Chapter four was divided into two different subchapters, each one containing a separate project that was carried out during this thesis, and based on the laser fabrication of TMDs nanomaterials. In the first subchapter, a simple and environmentally friendly approach to produce high-quality inorganic WS_2 and MoS_2 nanostructures through ultrashort pulse laser irradiation of the bulk material in ambient conditions, is demonstrated. In the second subchapter, a novel approach for the fabrication of hierarchical TMD structures via PLD is presented and discussed.

Annex: Publications obtained from the work of this Thesis

1) The work of chapter 3.1 was published in *Journal of Materials Chemistry C* (K. Savva, A. Y.-H. Lin, C. Petridis, E. Kymakis, T. D. Anthopoulos and E. Stratakis, *J.Mater. Chem. C*, 2, 5931-5937, 2014)

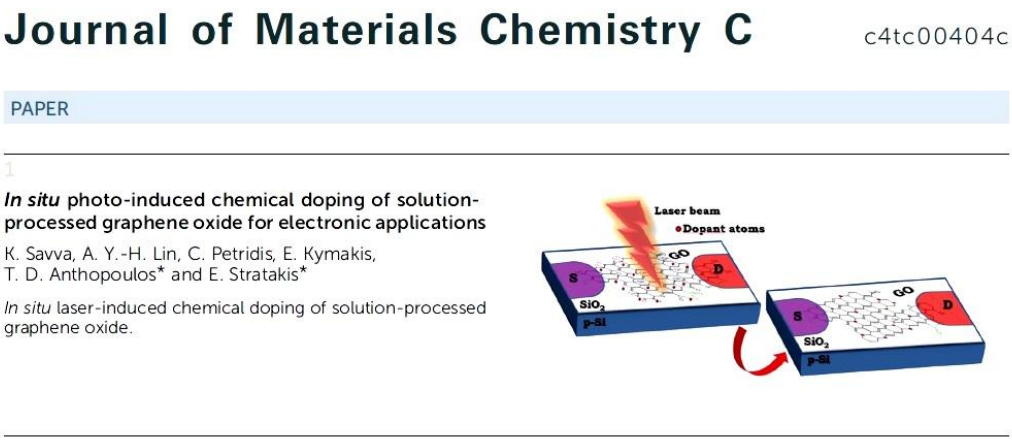

2) The work of chapter 3.2 was published in *Nanoscale* (E. Stratakis, K. Savva, D. Konios, C. Petridis and E. Kymakis, *Nanoscale*, 6, 6925–6931, 2014)

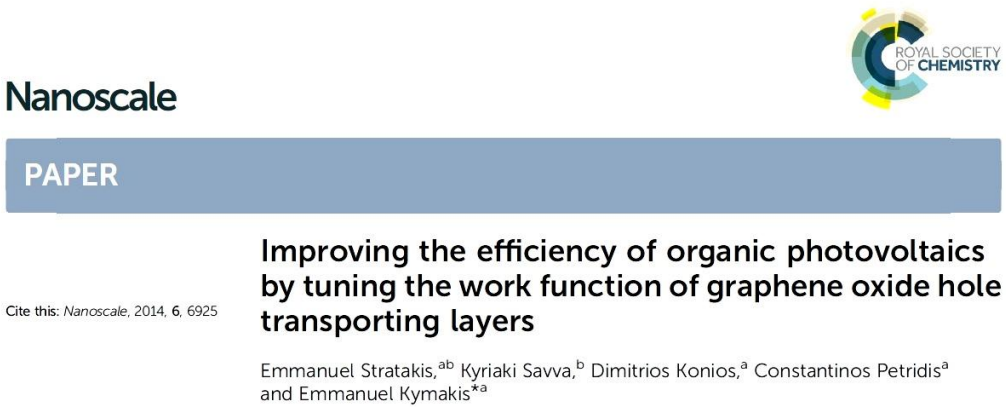

3) The work of chapter 3.3 was published in *Advanced Functional Materials* (D. Konios, C. Petridis, G. Kakavelakis, M. Sygletou, K. Savva, E. Stratakis and E. Kymakis, *Adv. Funct. Mater.* 25, 15, 2213-2221, 2015) and was hosted by the journal as its front cover of issue.

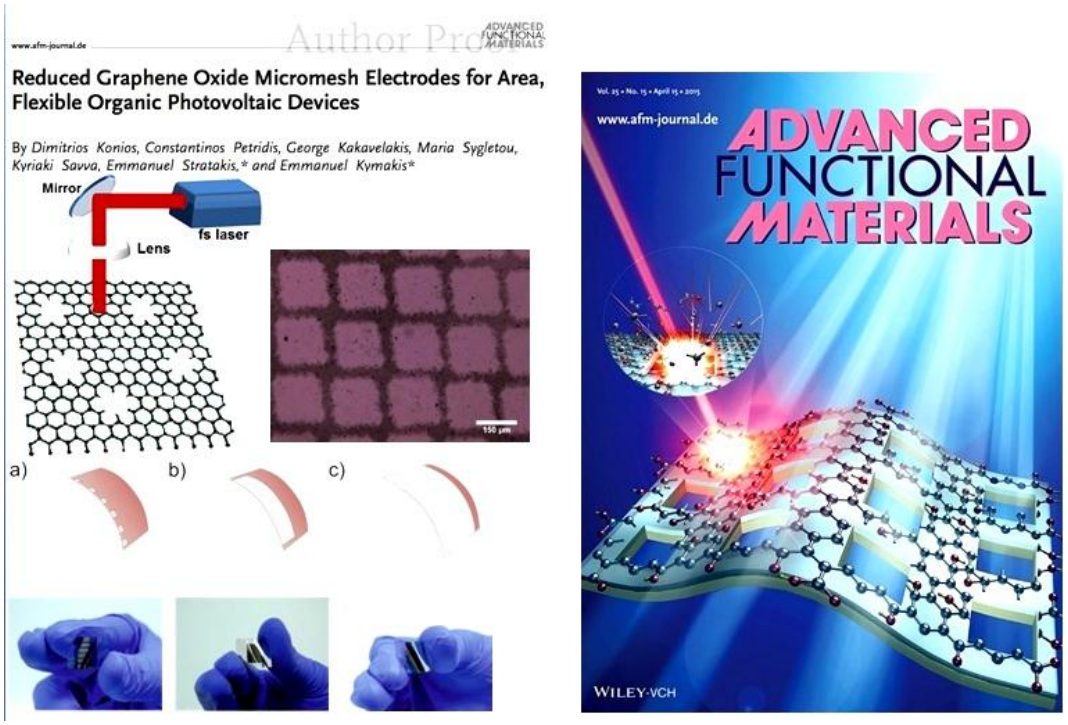

4) The work of chapter 4.1 was published in *ACS Omega*, (K. Savva, B. Višić, R. Popovitz-Biro, E. Stratakis and R., *ACS Omega* 2, 2649−2656, 2017)

ACS OMEGA

Article

http://pubs.acs.org/journal/acsodf

Short Pulse Laser Synthesis of Transition-Metal Dichalcogenide Nanostructures under Ambient Conditions

Kyriaki Savva,[†,‡,∥] Bojana Višić,[§,∥] Ronit Popovitz-Biro,[‡] Emmanuel Stratakis,*[,†,‡] and Reshef Tenne*[,§]

[†]Institute of Electronic Structure and Laser Foundation for Research and Technology - Hellas, Heraklion, 71110 Crete, Greece

[‡]Physics Department, University of Crete, Heraklion, 71004 Crete, Greece

[§]Weizmann Institute of Science, 7610001 Rehovot, Israel

ABSTRACT: The study of inorganic nanometer-scale materials with hollow closed-cage structures, such as inorganic fullerene-like (IF) nanostructures and inorganic nanotubes (INTs), is a rapidly growing field. Numerous kinds of IF nanostructures and INTs were synthesized for a variety of applications, particularly for lubrication, functional coatings, and reinforcement of polymer matrices. To date, such nanostructures have been synthesized mostly by heating a transition metal or oxide thereof in the presence of precursor gases, which are however toxic and hazardous. In this context, one frontier of research in this field is the development of new avenues for the green synthesis of IF structures and INTs, directly from the bulk of layered compounds. In the present work, we demonstrate a simple room-temperature and environmentally friendly approach for the synthesis of IF nanostructures and INTs via ultrashort-pulse laser ablation of a mixture of transition-metal dichalcogenides in bulk form mixed with Pb/PbO, in ambient air. The method can be considered as a synergy of photothermally and photochemically induced chemical transformations. The ultrafast-laser-induced excitation of the material, complemented with the formation of extended hot annealing regions in the presence of the metal catalyst, facilitates the formation of different nanostructures. Being fast, easy, and material-independent, our method offers new opportunities for the synthesis of IF nanostructures and INTs from different bulk metal chalcogenide compounds. On the basis of the capabilities of laser technology as well, this method could advantageously be further developed into a versatile tool for the simultaneous growth and patterning of such nanostructures in preselected positions for a variety of applications.

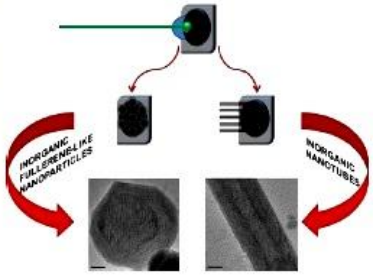

5) The work of chapter 4.2 is currently in preparation and will soon submitted

References

1. Novoselov, K. S. *et al.* Two-dimensional atomic crystals. *Proc. Natl. Acad. Sci.* **102,** 10451–10453 (2005).
2. Dresselhaus, M. S. *Physical Properties of Carbon Nanotubes*. *Carbon Nanotubes* (2005). doi:10.1142/p080
3. Article, P. Full-Text. *Nat. Mater.* **6,** 183–191 (2007).
4. Tenne, R. Advances in the synthesis of inorganic nanotubes and fullerene- like nanoparticles. *Angew. Chemie-International Ed.* **42,** 5124–5132 (2003).
5. Cooper, D. R. *et al.* Experimental review of graphene. (2011). doi:10.5402/2012/501686
6. Barbolina, I. I. *et al.* Submicron sensors of local electric field with single-electron resolution at room temperature. *Appl. Phys. Lett.* **88,** 88–91 (2006).
7. Han, M. Y., Özyilmaz, B., Zhang, Y. & Kim, P. Energy band-gap engineering of graphene nanoribbons. *Phys. Rev. Lett.* **98,** 1–4 (2007).
8. Schedin, F. *et al.* Detection of individual gas molecules adsorbed on graphene. *Nat. Mater.* **6,** 652–655 (2007).
9. Tombros, N., Jozsa, C., Popinciuc, M., Jonkman, H. T. & Van Wees, B. J. Electronic spin transport and spin precession in single graphene layers at room temperature. *Nature* **448,** 571–574 (2007).
10. Stankovich, S. *et al.* Graphene-based composite materials. *Nature* **442,** 282–286 (2006).
11. Dreyer, D. R., Park, S., Bielawski, C. W. & Ruoff, R. S. Graphite oxide. *Chem. Soc. Rev.* **39,** 228–240 (2010).
12. Zhu, Y. *et al.* Graphene and graphene oxide: Synthesis, properties, and applications. *Adv. Mater.* **22,** 3906–3924 (2010).
13. Eda, G. & Chhowalla, M. Chemically derived graphene oxide: Towards large-area thin-film electronics and optoelectronics. *Adv. Mater.* **22,** 2392–2415 (2010).
14. Eda, G., Fanchini, G. & Chhowalla, M. Large-area ultrathin films of reduced graphene oxide as a transparent and flexible electronic material. *Nat. Nanotechnol.* **3,** 270–274 (2008).
15. Wu, J. *et al.* Organic solar cells with solution-processed graphene transparent

electrodes. *Appl. Phys. Lett.* **92,** (2008).

16. Višić, B. Properties of two-dimensional graphene-like materials. *Nanomater. Energy* **4,** 18–29 (2015).
17. Akinwande, D., Petrone, N. & Hone, J. Two-dimensional flexible nanoelectronics. *Nat. Commun.* **5,** (2014).
18. Tenne, R. Recent advances in the research of inorganic nanotubes and fullerene-like nanoparticles. *Front. Phys.* **9,** 370–377 (2014).
19. Panchakarla, L. S. & Tenne, R. Inorganic Nanotubes and Fullerene-Like Nanoparticles at the Crossroad between Materials Science and Nanotechnology and Their Applications with Regard to Sustainability. *Nanotechnol. Energy Sustain.* 745–780 (2017). doi:10.1002/9783527696109.ch31
20. Novoselov, K. S. *et al.* Electric Field Effect in Atomically Thin Carbon Films. *Science (80-.).* **306,** 666–669 (2004).
21. Lee, C., Wei, X., Kysar, J. W. & Hone, J. Measurement of the elastic properties and intrinsic strength of monolayer graphene. *Science* **321,** 385–8 (2008).
22. Tiwari, A. & SyvßÏjßÏrvi, M. *Graphene Materials : Fundamentals and Emerging Applications.* (Wiley, 2015).
23. Balandin, A. A. *et al.* Superior Thermal Conductivity of Single-Layer Graphene. *Nano Lett.* **8,** 902–907 (2008).
24. P.R.Wallace. The Band Theory of Graphite - PhysRev.71.622. *Phys. Rev.* **329,** 622–634 (1946).
25. Allen, M. J., Tung, V. C. & Kaner, R. B. Honeycomb Carbon : A Review of Graphene. (2009).
26. Avouris, P. Graphene: Electronic and photonic properties and devices. *Nano Lett.* **10,** 4285–4294 (2010).
27. Hass, J., De Heer, W. A. & Conrad, E. H. The growth and morphology of epitaxial multilayer graphene. *J. Phys. Condens. Matter* **20,** (2008).
28. Hernandez, Y. *et al.* High-yield production of graphene by liquid-phase exfoliation of graphite. *Nat. Nanotechnol.* **3,** 563–568 (2008).
29. Miyamoto, Y., Zhang, H. & Tománek, D. Photoexfoliation of graphene from graphite: An Ab initio study. *Phys. Rev. Lett.* **104,** 19–22 (2010).
30. Lee, S. *et al.* Laser-Synthesized Epitaxial Graphene. *ACS Nano* **4,** 7524–7530 (2010).
31. Dhar, S. *et al.* A new route to graphene layers by selective laser ablation. *AIP*

Adv. **1,** 0–8 (2011).

32. Brodie, B. C. On the Atomic Weight of Graphite. *Philos. Trans. R. Soc. London* **149,** 249–259 (1859).
33. Jr, W. S. H. & Offeman, R. E. Preparation of Graphitic Oxide BY WILLIAM. *Water* **208,** 1937–1937 (1957).
34. Marcano, D. C. *et al.* Improved Synthesis of Graphene Oxide. *ACS Nano* **XXX,** 183–191 (2010).
35. Hofmann, U. & Holst, R. Über die Säurenatur und die Methylierung von Graphitoxyd. *Berichte der Dtsch. Chem. Gesellschaft (A B Ser.* **72,** 754–771 (1939).
36. U b e r das G r a p h i t o x y h y d r o x y d (G r a p h i t o x y d) . *Monatshefte* (1946).
37. Scholz, W. & Boehm, H. P. Betrachtungen zur Struktur des Graphitoxids. *Zeitschrift für Anorg. und Allg. Chemie* **369,** 327–340 (1969).
38. Nakajima, T., Mabuchi, A. & Hagiwara, R. A new structure model of graphite oxide. *Carbon N. Y.* **26,** 357–361 (1988).
39. Lerf, A., He, H., Forster, M. & Klinowski, J. Structure of Graphite Oxide Revisited ‖. *J. Phys. Chem. B* **102,** 4477–4482 (1998).
40. Josepovits, K., Sanakis, Y., Petridis, D. & De, I. Evolution of Surface Functional Groups in a Series of Progressively Oxidized Graphite Oxides. 2740–2749 (2006).
41. Gao, W., Alemany, L. B., Ci, L. & Ajayan, P. M. New insights into the structure and reduction of graphite oxide. *Nat. Chem.* **1,** 403–408 (2009).
42. Eng, A. Y. S., Chua, C. K. & Pumera, M. Refinements to the structure of graphite oxide: absolute quantification of functional groups via selective labelling. *Nanoscale* **7,** 20256–20266 (2015).
43. Schütze, M. Corrosion Books: Introduction to High Temperature Oxidation and Corrosion. By: A.S. Khanna - Materials and Corrosion 5/2003. *Mater. Corros.* **54,** 346–347 (2003).
44. Chua, C. K. & Pumera, M. Chem Soc Rev Chemical reduction of graphene oxide : a synthetic chemistry viewpoint. 291–312 (2014). doi:10.1039/c3cs60303b
45. Mcallister, M. J. *et al.* Expansion of Graphite. *Society* **19,** 4396–4404 (2007).
46. KUMAR, P., SUBRAHMANYAM, K. S. & RAO, C. N. R. Graphene

Produced By Radiation-Induced Reduction of Graphene Oxide. *Int. J. Nanosci.* **10,** 559–566 (2011).

47. Zhang, Y. L. *et al.* Photoreduction of Graphene Oxides: Methods, Properties, and Applications. *Adv. Opt. Mater.* **2,** 10–28 (2014).
48. Abdelsayed, V. *et al.* Photothermal deoxygenation of graphite oxide with laser excitation in solution and graphene-aided increase in water temperature. *J. Phys. Chem. Lett.* **1,** 2804–2809 (2010).
49. Huang, L. *et al.* Pulsed laser assisted reduction of graphene oxide. *Carbon N. Y.* **49,** 2431–2436 (2011).
50. Zhang, Y. *et al.* Direct imprinting of microcircuits on graphene oxides film by femtosecond laser reduction. *Nano Today* **5,** 15–20 (2010).
51. Shah, I. & John, Q. Laser modification of graphene oxide thin films studied by X-ray diffraction, X-ray photoelectron spectroscopy, Raman spectroscopy and electrical resistance measurements. (2018).
52. Guo, B., Fang, L., Zhang, B. & Gong, J. R. Graphene Doping: A Review. *Insciences J.* **1,** 80–89 (2011).
53. Boukhvalov, D. W. & Katsnelson, M. I. Tuning the gap in bilayer graphene using chemical functionalization: Density functional calculations. *Phys. Rev. B - Condens. Matter Mater. Phys.* **78,** 1–5 (2008).
54. Yang, M., Zhou, L., Wang, J., Liu, Z. & Liu, Z. Evolutionary chlorination of graphene: From charge-transfer complex to covalent bonding and nonbonding. *J. Phys. Chem. C* **116,** 844–850 (2012).
55. Li, X. *et al.* Simultaneous Nitrogen Doping and Reduction of Graphene Oxide. *J. Am. Chem. Soc.* **131,** 15939–15944 (2009).
56. Wu, J. *et al.* Controlled chlorine plasma reaction for noninvasive graphene doping. *J. Am. Chem. Soc.* **133,** 19668–19671 (2011).
57. Gopalakrishnan, K., Subrahmanyam, K. S., Kumar, P., Govindaraj, A. & Rao, C. N. R. Reversible chemical storage of halogens in few-layer graphene. *RSC Adv.* **2,** 1605–1608 (2012).
58. Loh, K. P., Bao, Q., Eda, G. & Chhowalla, M. Graphene oxide as a chemically tunable platform for optical applications. *Nat. Chem.* **2,** 1015–1024 (2010).
59. Yin, Z. Y. *et al.* Organic Photovoltaic Devices Using Highly Flexible Reduced Graphene Oxide Films as Transparent Electrodes. *ACS Nano* **4,** 5263–5268 (2010).

60. Robinson, J. T., Perkins, F. K., Snow, E. S., Wei, Z. & Sheehan, P. E. Reduced graphene oxide molecular sensors. *Nano Lett.* **8,** 3137–3140 (2008).
61. Guo, L. *et al.* Two-beam-laser interference mediated reduction, patterning and nanostructuring of graphene oxide for the production of a flexible humidity sensing device. *Carbon N. Y.* **50,** 1667–1673 (2012).
62. Vasu, K. S., Chakraborty, B., Sampath, S. & Sood, A. K. Probing top-gated field effect transistor of reduced graphene oxide monolayer made by dielectrophoresis. *Solid State Commun.* **150,** 1295–1298 (2010).
63. Joung, D., Chunder, A., Zhai, L. & Khondaker, S. I. High yield fabrication of chemically reduced graphene oxide field effect transistors by dielectrophoresis. *Nanotechnology* **21,** 1–8 (2010).
64. Guo, L. *et al.* Bandgap tailoring and synchronous microdevices patterning of graphene oxides. *J. Phys. Chem. C* **116,** 3594–3599 (2012).
65. Wang, Q. H., Kalantar-Zadeh, K., Kis, A., Coleman, J. N. & Strano, M. S. Electronics and optoelectronics of two-dimensional transition metal dichalcogenides. *Nat. Nanotechnol.* **7,** 699–712 (2012).
66. Late, D. J., Rout, C. S., Chakravarty, D. & Ratha, S. Emerging Energy Applications of Two-Dimensional Layered Materials. *Can. Chem. Trans.* **3,** 118–157 (2015).
67. Chhowalla, M. *et al.* The chemistry of two-dimensional layered transition metal dichalcogenide nanosheets. *Nat. Chem.* **5,** 263–275 (2013).
68. Lewerenz, H. J., Heller, A. & DiSalvo, F. J. Relationship between surface morphology and solar conversion efficiency of tungsten diselenide photoanodes. *J. Am. Chem. Soc.* **102,** 1877–1880 (1980).
69. Tributsch, H. Layer-Type Transition Metal Dichalcogenides - a New Class of Electrodes for Electrochemical Solar Cells. *Berichte der Bunsengesellschaft für Phys. Chemie* **81,** 361–369 (1977).
70. Tenne, R. & Wold, A. Passivation of recombination centers in *n* -WSe_2 yields high efficiency (>14%) photoelectrochemical cell. *Appl. Phys. Lett.* **47,** 707–709 (1985).
71. Radisavljevic, B., Radenovic, A., Brivio, J., Giacometti, V. & Kis, A. Single-layer MoS2 transistors. *Nat. Nanotechnol.* **6,** 147–150 (2011).
72. Tenne, R. Fullerene-like materials and nanotubes from inorganic compounds with a layered (2-D) structure. *Colloids Surfaces A Physicochem. Eng. Asp.*

208, 83–92 (2002).

73. Tenne, R., Margulis, L., Genut, M. & Hodes, G. Polyhedral and cylindrical structures of tungsten disulphide. *Nature* **360,** 444–446 (1992).
74. Margulis, L., Salitra, G., Tenne, R. & Talianker, M. Nested fullerene-like structures. *Nature* **365,** 113–114 (1993).
75. Chopra, N. G. *et al.* Boron Nitride Nanotubes. *Science (80-.).* **269,** 966–967 (1995).
76. Rosenfield Hacohen, Y., Grunbaum, E., Tenne, R., Sloan, J. & Hutchison, J. L. Cage structures and nanotubes of NiCl2 [5]. *Nature* **395,** 336–337 (1998).
77. Nath, M., Rao, C. N. R., Popovitz-biro, R. & Albu-yaron, A. Nanoparticles Produced by Laser Ablation of HfS 3 in Liquid Medium : Inorganic Fullerene-Like Structures of Hf2S. *Chem. Mater.* **16,** 2238–2243 (2004).
78. Albu-Yaron, A. *et al.* Synthesis of fullerene-like Cs2O nanoparticles by concentrated sunlight. *Adv. Mater.* **18,** 2993–2996 (2006).
79. Avivi, S., Mastai, Y. & Gedanken, A. A new fullerene-like inorganic compound fabricated by the sonolysis of an aqueous solution of TlCl3. *J. Am. Chem. Soc.* **122,** 4331–4334 (2000).
80. Srolovitz, D. J., Safran, S. A., Homyonfer, M. & Tenne, R. Morphology of nested fullerenes. *Phys. Rev. Lett.* **74,** 1779–1782 (1995).
81. Tenne, R. Doped and heteroatom-containing fullerene-like structures and nanotubes. *Adv. Mater.* **7,** 965–995 (1995).
82. Y. Feldman, † *et al.* Bulk Synthesis of Inorganic Fullerene-like MS2 (M = Mo, W) from the Respective Trioxides and the Reaction Mechanism. (1996). doi:10.1021/JA9602408
83. Feldman, Y., Margulis, L., Homyonfer, M. & Tenne, R. Preparation of Nested Fullerenes and Nanotubes of MoS2. *High Temp. Mater. Process.* **15,** 163–170 (1996).
84. Feldman, Y., Zak, A., Popovitz-Biro, R. & Tenne, R. New reactor for production of tungsten disulfide hollow onion-like (inorganic fullerene-like) nanoparticles. *Solid State Sci.* **2,** 663–672 (2000).
85. A. Zak, Y. Feldman, V. Alperovich, R. Rosentsveig, and & Tenne*, R. Growth Mechanism of MoS2 Fullerene-like Nanoparticles by Gas-Phase Synthesis. (2000). doi:10.1021/JA002181A
86. Li, X. L. & Li, Y. D. Formation of MoS2 Inorganic Fullerenes (IFs) by the

Reaction of MoO3 Nanobelts and S. *Chem. - A Eur. J.* **9,** 2726–2731 (2003).

87. Camacho-Bragado, G. A. *et al.* Structure and catalytic properties of nanostructured molybdenum sulfides. *J. Catal.* **234,** 182–190 (2005).
88. Rothschild, A. *et al.* Encapsulation of WC within 2H-WS2 inorganic fullerene-like cages. *Chem. Commun.* **0,** 363–364 (1999).
89. Whitby, R. L. D. *et al.* Complex WS2 nanostructures. *Chem. Phys. Lett.* **359,** 68–76 (2002).
90. Alexandrou, I. *et al.* Structural investigation of MoS_2 core–shell nanoparticles formed by an arc discharge in water. *Nanotechnology* **14,** 913–917 (2003).
91. Hu, J. J., Bultman, J. E. & Zabinski, J. S. Inorganic fullerene-like nanoparticles produced by arc discharge in water with potential lubricating ability. *Tribol. Lett.* **17,** 543–546 (2004).
92. Remskar, M. *et al.* Self-assembly of subnanometer-diameter single-wall MoS2nanotubes. *Science (80-.).* **292,** 479–481 (2001).
93. Vollath, D. & Szabó, D. . Synthesis of nanocrystalline MoS2 and WS2 in a microwave plasma. *Mater. Lett.* **35,** 236–244 (1998).
94. Brüser, V. *et al.* Single- to Triple-Wall WS2 Nanotubes Obtained by High-Power Plasma Ablation of WS2 Multiwall Nanotubes. *Inorganics* **2,** 177–190 (2014).
95. Li, X.-L., Ge, J.-P. & Li, Y.-D. Atmospheric Pressure Chemical Vapor Deposition: An Alternative Route to Large-Scale MoS2 and WS2 Inorganic Fullerene-like Nanostructures and Nanoflowers. *Chem. - A Eur. J.* **10,** 6163–6171 (2004).
96. Brontvein, O. *et al.* New High-Temperature Pb-Catalyzed Synthesis of Inorganic Nanotubes. *J. Am. Chem. Soc.* **134,** 16379–16386 (2012).
97. Philip A. Parilla, *,† *et al.* Formation of Nanooctahedra in Molybdenum Disulfide and Molybdenum Diselenide Using Pulsed Laser Vaporization. (2004). doi:10.1021/JP036202+
98. Sen, R. *et al.* Encapsulated and hollow closed-cage structures of WS2 and MoS2 prepared by laser ablation at 450–1050°C. *Chem. Phys. Lett.* **340,** 242–248 (2001).
99. Rosenfeld Hacohen, Y. *et al.* Synthesis of NiCl2 nanotubes and fullerene-like structures by laser ablation: theoretical considerations and comparison with MoS2 nanotubes. *Phys. Chem. Chem. Phys.* **5,** 1644–1651 (2003).

100. Schuffenhauer, C. *et al.* Synthesis of Fullerene-Like Tantalum Disulfide Nanoparticles by a Gas-Phase Reaction and Laser Ablation. *Small* **1,** 1100–1109 (2005).
101. Feldman, Y. *et al.* Bulk Synthesis of Inorganic Fullerene-like MS_2 (M = Mo, W) from the Respective Trioxides and the Reaction Mechanism. *J. Am. Chem. Soc.* **118,** 5362–5367 (1996).
102. Tenne, R. Inorganic Nanotubes and Fullerene-Like Materials. *Chem. - A Eur. J.* **8,** 5296–5304 (2002).
103. Rosentsveig, R., Margolin, A., Feldman, Y., Popovitz-Biro, R. & Tenne, R. WS 2 Nanotube Bundles and Foils. *Chem. Mater.* **14,** 471–473 (2002).
104. Feldman, Y., Wasserman, E., Srolovitz, D. J. & Tenne, R. High-rate, gas phase growth of MoS2 nested inorganic fullerenes and nanotubes. *Science (80-.).* **267,** 222–225 (1995).
105. Therese, H. A., Li, J., Kolb, U. & Tremel, W. Facile large scale synthesis of WS 2 nanotubes from WO 3 nanorods prepared by a hydrothermal route. *Solid State Sci.* **7,** 67–72 (2005).
106. Zhu, Y. Q. *et al.* Production of WS 2 Nanotubes. 1190–1194 (2000).
107. ZAK, A., SALLACAN-ECKER, L., MARGOLIN, A., GENUT, M. & TENNE, R. INSIGHT INTO THE GROWTH MECHANISM OF WS_2 NANOTUBES IN THE SCALED-UP FLUIDIZED-BED REACTOR. *Nano* **04,** 91–98 (2009).
108. Tenne, R., Rosentsveig, R. & Zak, A. Inorganic nanotubes and fullerene-like nanoparticles: Synthesis, mechanical properties, and applications. *Phys. Status Solidi Appl. Mater. Sci.* **210,** 2253–2258 (2013).
109. Tenne, R. Recent advances in the research of inorganic nanotubes and fullerene-like nanoparticles. *Front. Phys.* **9,** 370–377 (2014).
110. Enyashin, A. N. *et al.* Structure and Stability of Molybdenum Sulfide Fullerenes. *Angew. Chemie Int. Ed.* **46,** 623–627 (2007).
111. Lauritsen, J. V. *et al.* Size-dependent structure of MoS2 nanocrystals. *Nat. Nanotechnol.* **2,** 53–58 (2007).
112. Kaplan-Ashiri, I. *et al.* Mechanical behavior of individual WS2 nanotubes. *J. Mater. Res.* **19,** 454–459 (2004).
113. Ifat Kaplan-Ashiri, † *et al.* Microscopic Investigation of Shear in Multiwalled Nanotube Deformation. (2007). doi:10.1021/JP070832K

114. Yu, M.-F., Files, B. S., Arepalli, S. & Ruoff, R. S. Tensile Loading of Ropes of Single Wall Carbon Nanotubes and their Mechanical Properties. *Phys. Rev. Lett.* **84,** 5552–5555 (2000).
115. Min-Feng, Oleg Lourie, Mark J.Dyer, Katerina Moloni, Thomas F.Kelly, R. S. R. Strenght and Breaking Mechanism of Multiwalled Carbon Nanotubes Under Tensile Load. *Sciencec* **287,** 1–4 (2000).
116. Kaplan-Ashiri, I. *et al.* On the mechanical behavior of WS2 nanotubes under axial tension and compression. *Proc. Natl. Acad. Sci.* **103,** 523–528 (2006).
117. Seifert, G., Terrones, H., Terrones, M., Jungnickel, G. & Frauenheim, T. On the electronic structure of WS2 nanotubes. *Solid State Commun.* **114,** 245–248 (2000).
118. Seifert, G., Terrones, H., Terrones, M., Jungnickel, G. & Frauenheim, T. Structure and Electronic Properties of MoS 2 Nanotubes. *Phys. Rev. Lett.* **85,** 146–149 (2000).
119. A. Rothschild, †, J. Sloan, ‡ and & R. Tenne*, †. Growth of WS2 Nanotubes Phases. (2000). doi:10.1021/JA994118V
120. Scheffer, L. *et al.* Scanning tunneling microscopy study of WS2 nanotubes. *Phys. Chem. Chem. Phys.* **4,** 2095–2098 (2002).
121. Watanabe, S., Noshiro, J. & Miyake, S. Tribological characteristics of WS2/MoS2 solid lubricating multilayer films. *Surf. Coatings Technol.* **183,** 347–351 (2004).
122. Zabinski, J. S., Donley, M. S. & Prasad, S. V. Synthesis and Characterization of Tungsten Disulfide Films Grown By Pulsed-Laser Deposition. *J. Mater. Sci.* **29,** 4834–4839 (1994).
123. Zak, A. *et al.* Scaling Up of the WS_2 Nanotubes Synthesis. *Fullerenes, Nanotub. Carbon Nanostructures* **19,** 18–26 (2010).
124. Adini, A. R. *et al.* Alleviating fatigue and failure of NiTi endodontic files by a coating containing inorganic fullerene-like WS2 nanoparticles. *J. Mater. Res.* **26,** 1234–1242 (2011).
125. Rapoport, L., Fleischer, N. & Tenne, R. Fullerene-like WS2 Nanoparticles: Superior Lubricants for Harsh Conditions. *Adv. Mater.* **15,** 651–655 (2003).
126. Rapoport, L. *et al.* Polymer Nanocomposites with Fullerene-like Solid Lubricant. *Adv. Eng. Mater.* **6,** 44–48 (2004).
127. Alla Zak, † *et al.* Alkali Metal Intercalated Fullerene-Like MS2 (M = W, Mo)

Nanoparticles and Their Properties. (2002). doi:10.1021/JA012060Q

128. Rothschild, A., Cohen, S. R. & Tenne, R. WS2 nanotubes as tips in scanning probe microscopy. *Appl. Phys. Lett.* **75,** 4025–4027 (1999).
129. Kymakis, E., Savva, K., Stylianakis, M. M., Fotakis, C. & Stratakis, E. Flexible organic photovoltaic cells with in situ nonthermal photoreduction of spin-coated graphene oxide electrodes. *Adv. Funct. Mater.* **23,** 2742–2749 (2013).
130. Chichkov, B. N., Momma, C., Nolte, S., Von Alvensleben, F. & Tünnermann, A. Femtosecond, picosecond and nanosecond laser ablation of solids. *Appl. Phys. A Mater. Sci. Process.* **63,** 109–115 (1996).
131. Parilla, P. A. *et al.* The first true inorganic fullerenes? *Nature* **397,** 114 (1999).
132. Rosenfeld Hacohen, Y. *et al.* Synthesis of NiCl2 nanotubes and fullerene-like structures by laser ablation: Theoretical considerations and comparison with MoS2 nanotubes. *Phys. Chem. Chem. Phys.* **5,** 1644–1651 (2003).
133. Schuffenhauer, C. *et al.* Synthesis of fullerene-like tantalum disulfide nanoparticles by a gas-phase reaction and laser ablation. *Small* **1,** 1100–1109 (2005).
134. Albu-Yaron, A. *et al.* Preparation and structural characterization of stable Cs2O closed-cage structures. *Angew. Chemie - Int. Ed.* **44,** 4169–4172 (2005).
135. Levi, R. *et al.* Hollow V2O5 nanoparticles (Fullerene-Like Analogues) prepared by laser ablation. *J. Am. Chem. Soc.* **132,** 11214–11222 (2010).
136. Wu, H. *et al.* Biocompatible inorganic fullerene-like molybdenum disulfide nanoparticles produced by pulsed laser ablation in water. *ACS Nano* **5,** 1276–1281 (2011).
137. T, C. J. Pulsed Laser Deposition. **48,** 45–48 (2014).
138. Krebs, H. *et al.* Pulsed Laser Deposition (PLD) - a Versatile Thin Film Technique UHV-chamber. *Adv. Solid State Phys. SE - 36* 505–518 (2003). doi:10.1007/978-3-540-44838-9_36
139. Eason, R. & Wiley InterScience (Online service). *Pulsed laser deposition of thin films : applications-led growth of functional materials*. (Wiley-Interscience, 2007).
140. Singh, R. K. & Narayan, J. Pulsed-Laser Evaporation Technique for Deposition of Thin-Films - Physics and Theoretical-Model. *Phys. Rev. B* **41,** 8843–8859 (1990).
141. Yang, Z. & Hao, J. Progress in pulsed laser deposited two-dimensional layered

materials for device applications. *J. Mater. Chem. C* **4,** 8859–8878 (2016).

142. Late, D. J. *et al.* Pulsed laser-deposited MoS2 thin films on W and Si: Field emission and photoresponse studies. *ACS Appl. Mater. Interfaces* **6,** 15881–15888 (2014).
143. Loh, T. A. J., Chua, D. H. C. & Wee, A. T. S. One-step Synthesis of Few-layer WS2 by Pulsed Laser Deposition. *Sci. Rep.* **5,** 1–9 (2015).
144. Stratakis, E. CHAPTER 10. Hierarchical Field Emission Devices. in 230–243 (2014). doi:10.1039/9781849737500-00230
145. Berkdemir, A. *et al.* Identification of individual and few layers of WS2 using Raman Spectroscopy. *Sci. Rep.* **3,** 1755 (2013).
146. Viršek, M., Jesih, A., Milošević, I., Damnjanović, M. & Remškar, M. Raman scattering of the MoS2 and WS2 single nanotubes. *Surf. Sci.* **601,** 2868–2872 (2007).
147. Zou, S. D. Y. and L. X. C. and H. B. Y. and B. B. L. and Y. Y. H. and L. W. and M. G. Y. and T. C. and G. T. Study of the hydrostatic pressure dependence of the Raman spectrum of W/WS2 fullerene-like nanosphere with core-shell structure. *J. Phys. Condens. Matter* **19,** 425228 (2007).
148. Li, X.-L., Ge, J.-P. & Li, Y.-D. Atmospheric Pressure Chemical Vapor Deposition: An Alternative Route to Large-Scale MoS2 and WS2 Inorganic Fullerene-like Nanostructures and Nanoflowers. *Chem. - A Eur. J.* **10,** 6163–6171 (2004).
149. Prabakaran, A. *et al.* WS22D nanosheets in 3D nanoflowers. *Chem. Commun.* **50,** 12360–12362 (2014).
150. Web, I. S. I. *et al.* Graphene : Status and Prospects. *Science (80-.).* **1530,** 1530–1534 (2014).
151. Yu, S., Zheng, W., Wang, C. & Jiang, Q. Nitrogen/boron doping position dependence of the electronic properties of a triangular graphene. *ACS Nano* **4,** 7619–7629 (2010).
152. Casiraghi, C. Doping dependence of the Raman peaks intensity of graphene close to the Dirac point. *Phys. Rev. B - Condens. Matter Mater. Phys.* **80,** 2–4 (2009).
153. Luo, Z., Pinto, N. J., Davila, Y. & Charlie Johnson, A. T. Controlled doping of graphene using ultraviolet irradiation. *Appl. Phys. Lett.* **100,** (2012).
154. Bekyarova, E. *et al.* Chemical Modification of Epitaxial Graphene. 820382

(2009).

155. Liu, H., Liu, Y. & Zhu, D. Chemical doping of graphene. *J. Mater. Chem.* **21,** 3335–3345 (2011).
156. Hall, E. O. *et al.* No Title. 610–613 (2009).
157. Li, B. *et al.* Photochemical chlorination of graphene. *ACS Nano* **5,** 5957–5961 (2011).
158. Zhang, L. *et al.* Photocatalytic Patterning and Modification of Graphene.pdf. 2706–2713 (2011).
159. Zhang, L. *et al.* Simultaneous reduction and N-doping of graphene oxides by low-energy N2+ion sputtering. *Carbon N. Y.* **62,** 365–373 (2013).
160. Gong, P. *et al.* Photochemical synthesis of fluorinated graphene via a simultaneous fluorination and reduction route. *RSC Adv.* **3,** 6327 (2013).
161. Kumar, N. A. *et al.* Plasma-assisted simultaneous reduction and nitrogen doping of graphene oxide nanosheets. *J. Mater. Chem. A* **1,** 4431 (2013).
162. Huan, T. N., Van Khai, T., Kang, Y., Shim, K. B. & Chung, H. Enhancement of quaternary nitrogen doping of graphene oxide via chemical reduction prior to thermal annealing and an investigation of its electrochemical properties. *J. Mater. Chem.* **22,** 14756 (2012).
163. Liu, Y. *et al.* Realization of ferromagnetic graphene oxide with high magnetization by doping graphene oxide with nitrogen. *Sci. Rep.* **3,** (2013).
164. Singh, G. *et al.* Study of simultaneous reduction and nitrogen doping of graphene oxide Langmuir-Blodgett monolayer sheets by ammonia plasma treatment. *Nanotechnology* **24,** (2013).
165. Wang, S. *et al.* Band-like transport in surface-functionalized highly solution-processable graphene nanosheets. *Adv. Mater.* **20,** 3440–3446 (2008).
166. Liu, H. *et al.* Photochemical Reactivity of Graphene Supporting Information. *Nature* 563–568 (2008).
167. Petridis, C. *et al.* Post-fabrication, in situ laser reduction of graphene oxide devices. *Appl. Phys. Lett.* **102,** (2013).
168. Guo, L. *et al.* Laser-mediated programmable n doping and simultaneous reduction of graphene oxides. *Adv. Opt. Mater.* **2,** 120–125 (2014).
169. Wehling, T. O. *et al.* Molecular doping of graphene. *Nano Lett.* **8,** 173–177 (2008).
170. Somers, L. High Yield Preparation of Macroscopic Graphene Oxide

Membranes High Yield Preparation of Macroscopic Graphene Oxide Membranes. 9–11 (2015). doi:10.1021/ja807934n

171. Stankovich, S. *et al.* Synthesis of graphene-based nanosheets via chemical reduction of exfoliated graphite oxide. *Carbon N. Y.* **45,** 1558–1565 (2007).
172. Wang, D.-W. *et al.* A microporous–mesoporous carbon with graphitic structure for a high-rate stable sulfur cathode in carbonate solvent-based Li–S batteries. *Phys. Chem. Chem. Phys.* **14,** 8703 (2012).
173. Wang, X. *et al.* N-doping of graphene through electrothermal reactions with ammonia. *Science (80-.).* **324,** 768–771 (2009).
174. Bahr, J. L. *et al.* Functionalization of Carbon Nanotubes by Electrochemical Reduction of Aryl Diazonium Salts : A Bucky Paper Electrode Functionalization of Carbon Nanotubes by Electrochemical Reduction of Aryl Diazonium Salts : A Bucky Paper Electrode. **3,** 6536–6542 (2011).
175. Ramanathan, T., Fisher, F. T., Ruoff, R. S. & Brinson, L. C. Amino-fimctionalized carbon nanotubes for binding to polymers and biological systems. *Chem. Mater.* **17,** 1290–1295 (2005).
176. Karousis, N., Economopoulos, S. P., Sarantopoulou, E. & Tagmatarchis, N. Porphyrin counter anion in imidazolium-modified graphene-oxide. *Carbon N. Y.* **48,** 854–860 (2010).
177. Ferrari, A. C. Raman spectroscopy of graphene and graphite: Disorder, electron-phonon coupling, doping and nonadiabatic effects. *Solid State Commun.* **143,** 47–57 (2007).
178. Zhan, D. *et al.* Electronic structure of graphite oxide and thermally reduced graphite oxide. *Carbon N. Y.* **49,** 1362–1366 (2011).
179. Pimenta, M. A. *et al.* Studying disorder in graphite-based systems by Raman spectroscopy. *Phys. Chem. Chem. Phys.* **9,** 1276–1290 (2007).
180. Das, A. *et al.* Monitoring dopants by Raman scattering in an electrochemically top-gated graphene transistor. *Nat. Nanotechnol.* **3,** 210–215 (2008).
181. Baumfalk, R., Nahler, N. H. & Buck, U. Photodissociation of oriented HXeI molecules in the gas phase. *J. Chem. Phys.* **114,** 4755–4758 (2001).
182. Tateishi, H. *et al.* Photoreaction of Graphene Oxide Nanosheet in Water. *J. Phys. Chem. C* **752,** 19280–19286 (2011).
183. Eda, G. *et al.* Transparent and conducting electrodes for organic electronics from reduced graphene oxide. *Appl. Phys. Lett.* **92,** 1–4 (2008).

184. Lin, Y. C., Lin, C. Y. & Chiu, P. W. Controllable graphene N-doping with ammonia plasma. *Appl. Phys. Lett.* **96,** (2010).
185. Eda, G. *et al.* Graphene oxide gate dielectric for graphene-based monolithic field effect transistors. *Appl. Phys. Lett.* **102,** 13–17 (2013).
186. Chen, H.-Y. *et al.* Polymer solar cells with enhanced open-circuit voltage and efficiency. *Nat. Photonics* **3,** 649–653 (2009).
187. Zhao, G. J., He, Y. J. & Li, Y. 6.5% efficiency of polymer solar cells based on poly(3-hexylthiophene) and indene-C60 bisadduct by device optimization. *Adv. Mater.* **22,** 4355–4358 (2010).
188. Stratakis, E. & Kymakis, E. Nanoparticle-based plasmonic organic photovoltaic devices. *Mater. Today* **16,** 133–146 (2013).
189. Jayawardena, K. D. G. I. *et al.* 'Inorganics-in-Organics': recent developments and outlook for 4G polymer solar cells. *Nanoscale* **5,** 8411 (2013).
190. Brabec, C. J. *et al.* Polymer-Fullerene Bulk-Heterojunction Solar Cells. *Adv. Mater.* **22,** 3839–3856 (2010).
191. Steim, R., Kogler, F. R. & Brabec, C. J. Interface materials for organic solar cells. *J. Mater. Chem.* **20,** 2499 (2010).
192. Yip, H.-L. & Jen, A. K.-Y. Recent advances in solution-processed interfacial materials for efficient and stable polymer solar cells. *Energy Environ. Sci.* **5,** 5994 (2012).
193. Po, R., Carbonera, C., Bernardi, A. & Camaioni, N. The role of buffer layers in polymer solar cells. *Energy Environ. Sci.* **4,** 285–310 (2011).
194. Zhang, F., Ceder, M. & Inganäs, O. Enhancing the photovoltage of polymer solar cells by using a modified cathode. *Adv. Mater.* **19,** 1835–1838 (2007).
195. Yan, H. *et al.* High-performance hole-transport layers for polymer light-emitting diodes. Implementation of organosiloxane cross-linking chemistry in polymeric electroluminescent devices. *J. Am. Chem. Soc.* **127,** 3172–3183 (2005).
196. Jørgensen, M., Norrman, K. & Krebs, F. C. Stability/degradation of polymer solar cells. *Sol. Energy Mater. Sol. Cells* **92,** 686–714 (2008).
197. Yang, X. H. *et al.* Efficient polymer electrophosphorescent devices with interfacial layers. *Adv. Funct. Mater.* **16,** 2156–2162 (2006).
198. Van De Lagemaat, J. *et al.* Organic solar cells with carbon nanotubes replacing In2 O3: Sn as the transparent electrode. *Appl. Phys. Lett.* **88,** 3–6 (2006).

199. So, F. & Kondakov, D. Degradation mechanisms in small-molecule and polymer organic light-emitting diodes. *Adv. Mater.* **22,** 3762–3777 (2010).
200. Hains, A. W. & Marks, T. J. High-efficiency hole extraction/electron-blocking layer to replace poly(3,4-ethylenedioxythiophene):poly(styrene sulfonate) in bulk-heterojunction polymer solar cells. *Appl. Phys. Lett.* **92,** 2006–2009 (2008).
201. M. Kemerink, S. Timpanaro, M. M. de Kok, E. A. Meulenkamp, and F. J. T. Three-dimensional inhomogeneities in PEDOT : PSS films. *J. Phys. Chem. B* **108,** 18820–18825 (2004).
202. Garcia, A. *et al.* Improvement of interfacial contacts for new small-molecule bulk-heterojunction organic photovoltaics. *Adv. Mater.* **24,** 5368–5373 (2012).
203. White, M. S., Olson, D. C., Shaheen, S. E., Kopidakis, N. & Ginley, D. S. Inverted bulk-heterojunction organic photovoltaic device using a solution-derived ZnO underlayer. *Appl. Phys. Lett.* **89,** (2006).
204. Greiner, M. T. *et al.* Universal energy-level alignment of molecules on metal oxides. *Nat. Mater.* **11,** 76–81 (2012).
205. Vasilopoulou, M. *et al.* Hydrogenated under-stoichiometric tungsten oxide anode interlayers for efficient and stable organic photovoltaics. *J. Mater. Chem. A* **2,** 1738–1749 (2014).
206. Kymakis, E. *et al.* Spin coated carbon nanotubes as the hole transport layer in organic photovoltaics. *Sol. Energy Mater. Sol. Cells* **96,** 298–301 (2012).
207. Wang, H. *et al.* Multifunctional TiO2nanowires-modified nanoparticles bilayer film for 3D dye-sensitized solar cells. *Optoelectron. Adv. Mater. Rapid Commun.* **4,** 1166–1169 (2010).
208. Li, S., Tu, Ḱ. K., Lin, Ḱ. C., Chen, C. & Chhowalla, M. Solution-Processable Graphene Oxide as an Efficient Hole Transport Layer in Polymer Solar Cells. **4,** 3169–3174 (2010).
209. Kim, H. P., Mohd Yusoff, A. R. Bin & Jang, J. Organic solar cells using a reduced graphene oxide anode buffer layer. *Sol. Energy Mater. Sol. Cells* **110,** 87–93 (2013).
210. Liu, X., Kim, H. & Guo, L. J. Optimization of thermally reduced graphene oxide for an efficient hole transport layer in polymer solar cells. *Org. Electron. physics, Mater. Appl.* **14,** 591–598 (2013).
211. Ishii, Y., Yang, D., Velamakanni, A., An, S. J. & Stoller, M. Structural

Characterization of C-Labeled Graphite Oxide. *Science (80-.).* **321,** 1815–1818 (2008).

212. Matyba, P., Yamaguchi, H., Chhowalla, M., Robinson, N. D. & Edman, L. Flexible and Metal-Free Light-Emitting Electrochemical Cells Based on Graphene and PEDOT-PSS as the Electrode Materials. *ACS Nano* **5,** 574–580 (2011).
213. Liu, J. *et al.* Hole and electron extraction layers based on graphene oxide derivatives for high-performance bulk heterojunction solar cells. *Adv. Mater.* **24,** 2228–2233 (2012).
214. Lee, B. R. *et al.* Highly Efficient Polymer Light-Emitting Diodes Using Graphene Oxide as a Hole Transport Layer. *ACS Nano* **6,** 2984–2991 (2012).
215. Chochos, C. L. & Choulis, S. A. How the structural deviations on the backbone of conjugated polymers influence their optoelectronic properties and photovoltaic performance. *Prog. Polym. Sci.* **36,** 1326–1414 (2011).
216. Yang, D. *et al.* Chemically modified graphene oxides as a hole transport layer in organic solar cells. *Chem. Commun.* **48,** 8078 (2012).
217. Liu, J., Xue, Y. & Dai, L. Sulfated Graphene Oxide as a Hole-Extraction Layer in High- Performance Polymer Solar Cells. *J. Phys. Chem. Lett.* **3,** 1928–1933 (2012).
218. Li, D., Müller, M. B., Gilje, S., Kaner, R. B. & Wallace, G. G. Processable aqueous dispersions of graphene nanosheets. *Nat. Nanotechnol.* **3,** 101–105 (2008).
219. Kumar, P. V., Bernardi, M. & Grossman, J. C. The impact of functionalization on the stability, work function, and photoluminescence of reduced graphene oxide. *ACS Nano* **7,** 1638–1645 (2013).
220. Kim, J. Y. *et al.* Chlorination of reduced graphene oxide enhances the dielectric constant of reduced graphene oxide/polymer composites. *Adv. Mater.* **25,** 2308–2313 (2013).
221. Kwon, K. C., Choi, K. S. & Kim, S. Y. Increased work function in few-layer graphene sheets via metal chloride Doping. *Adv. Funct. Mater.* **22,** 4724–4731 (2012).
222. Wassei, J. K., Cha, K. C., Tung, V. C., Yang, Y. & Kaner, R. B. The effects of thionyl chloride on the properties of graphene and graphene–carbon nanotube composites. *J. Mater. Chem.* **21,** 3391 (2011).

223. Chiu, M. Y., Jeng, U. S., Su, C. H., Liang, K. S. & Wei, K. H. Simultaneous use of small- and wide-angle X-ray techniques to analyze nanometerscale phase separation in polymer heterojunction solar cells. *Adv. Mater.* **20,** 2573–2578 (2008).

224. Shrotriya, V., Wu, E. H. E., Li, G., Yao, Y. & Yang, Y. Efficient light harvesting in multiple-device stacked structure for polymer solar cells. *Appl. Phys. Lett.* **88,** (2006).

225. Sariciftci, N., Smilowitz, L., Heeger, A. J. & Wudl, F. Photoinduced Electron Transfer from a Conducting Polymer to Buckminsterfullerene. *Science (80-.).* **258,** 1474–1476 (1992).

226. Yu, G., Gao, J., Hummelen, J. C., Wudl, F. & Heeger, A. J. device structure consisted Polymer Photovoltaic Cells : Enhanced Efficiencies via a (Ca The on a g | | g. *Science (80-.).* **270,** 1789–1791 (1995).

227. Li, G., Zhu, R. & Yang, Y. Polymer solar cells. *Nat. Photonics* **6,** 153–161 (2012).

228. Yalçin, L. & Öztürk, R. Performance comparison of c-Si, mc-Si and a-Si thin film PV by PVsyst simulation. *J. Optoelectron. Adv. Mater.* **15,** 326–334 (2013).

229. Scharber, M. C. & Sariciftci, N. S. Progress in Polymer Science Efficiency of bulk-heterojunction organic solar cells. *Prog. Polym. Sci.* **38,** 1929–1940 (2013).

230. Park, S. H. *et al.* Bulk heterojunction solar cells with internal quantum efficiency approaching 100%. *Nat. Photonics* **3,** 297–303 (2009).

231. Hecht, D. S., Hu, L. & Irvin, G. Emerging transparent electrodes based on thin films of carbon nanotubes, graphene, and metallic nanostructures. *Adv. Mater.* **23,** 1482–1513 (2011).

232. Wu, J. *et al.* Organic light-emitting diodes on solution-processed graphene transparent electrodes. *ACS Nano* **4,** 43–8 (2010).

233. Jose da Silva, W., Kim, H. P., Rashid bin Mohd Yusoff, A. & Jang, J. Transparent flexible organic solar cells with 6.87% efficiency manufactured by an all-solution process. *Nanoscale* **5,** 9324 (2013).

234. Paci, B. *et al.* Spatially-resolved in-situ structural study of organic electronic devices with nanoscale resolution: The plasmonic photovoltaic case study. *Adv. Mater.* **25,** 4760–4765 (2013).

235. Tyler, T. P., Brock, R. E., Karmel, H. J., Marks, T. J. & Hersam, M. C. Electronically monodisperse single-walled carbon nanotube thin films as transparent conducting anodes in organic photovoltaic devices. *Adv. Energy Mater.* **1,** 785–791 (2011).
236. Kymakis, E., Stratakis, E., Koudoumas, E. & Fotakis, C. Plasmonic Organic Photovoltaic Devices on Transparent Carbon Nanotube Films. *IEEE Tran. Elec. Dev.* **58,** 4 (2011).
237. De, S. *et al.* Silver Nanowire Networks as Flexible ,. **3,** 1767–1774 (2009).
238. Na, S.-I., Kim, S.-S., Jo, J. & Kim, D.-Y. Efficient and Flexible ITO-Free Organic Solar Cells Using Highly Conductive Polymer Anodes. *Adv. Mater.* **20,** 4061–4067 (2008).
239. Li, X. *et al.* Transfer of large-area graphene films for high-performance transparent conductive electrodes. *Nano Lett.* **9,** 4359–4363 (2009).
240. Kim, K. S. *et al.* Large-scale pattern growth of graphene films for stretchable transparent electrodes. *Nature* **457,** 706–710 (2009).
241. Klemens, T. & Anna, S. RSC Advances. 56335–56352 (2016). doi:10.1039/C6RA08981J
242. Maitra, U., Matte, H. S. S. R., Kumar, P. & Rao, C. N. R. Strategies for the Synthesis of Graphene, Graphene Nanoribbons, Nanoscrolls and Related Materials. *Chim. Int. J. Chem.* **66,** 941–948 (2012).
243. Kumar, P., Panchakarla, L. S. & Rao, C. N. R. Laser-induced unzipping of carbon nanotubes to yield graphene nanoribbons. *Nanoscale* **3,** 2127 (2011).
244. Kosynkin, D. V. *et al.* Longitudinal unzipping of carbon nanotubes to form graphene nanoribbons. *Nature* **458,** 872–876 (2009).
245. Stylianakis, M. M. *et al.* Photochemical Synthesis of Solution-Processable Graphene Derivatives with Tunable Bandgaps for Organic Solar Cells. *Adv. Opt. Mater.* **3,** 658–666 (2015).
246. Stratakis, E., Savva, K., Konios, D., Petridis, C. & Kymakis, E. Improving the efficiency of organic photovoltaics by tuning the work function of graphene oxide hole transporting layers. *Nanoscale* **6,** 6925–6931 (2014).
247. Yin, Z. *et al.* Graphene-Based materials for solar cell applications. *Adv. Energy Mater.* **4,** 1–19 (2014).
248. Kakavelakis, G., Konios, D., Stratakis, E. & Kymakis, E. Enhancement of the efficiency and stability of organic photovoltaic devices via the addition of a

lithium-neutralized graphene oxide electron-transporting layer. *Chem. Mater.* **26,** 5988–5993 (2014).

249. Bonaccorso, F., Sun, Z., Hasan, T. & Ferrari, A. C. Graphene photonics and optoelectronics. *Nat. Photonics* **4,** 611–622 (2010).
250. Bae, S. *et al.* Roll-to-roll production of 30-inch graphene films for transparent electrodes. *Nat. Nanotechnol.* **5,** 574–578 (2010).
251. Park, S. *et al.* Hydrazine-reduction of graphite- and graphene oxide. *Carbon N. Y.* **49,** 3019–3023 (2011).
252. Kumar, P. *et al.* Novel Radiation-Induced Properties of Graphene and Related Materials. *Chem. Synth. Appl. graphene carbon Mater.* 159–189 (2016). doi:10.1002/9783527648160.ch8
253. Kymakis, E., Petridis, C., Anthopoulos, T. D. & Stratakis, E. Laser - Assisted Reduction of Graphene Oxide for Flexible , Large - Area Optoelectronics. 1–11 (2013).
254. Bonaccorso, F. *et al.* Production and processing of graphene and 2d crystals. *Mater. Today* **15,** 564–589 (2012).
255. Konios, D., Stylianakis, M. M., Stratakis, E. & Kymakis, E. Dispersion behaviour of graphene oxide and reduced graphene oxide. *J. Colloid Interface Sci.* **430,** 108–112 (2014).
256. Xu, Y. *et al.* Polymer photovoltaic devices with transparent graphene electrodes produced by spin-casting. *Carbon N. Y.* **48,** 3308–3311 (2010).
257. Kymakis, E., Stratakis, E., Stylianakis, M. M., Koudoumas, E. & Fotakis, C. Spin coated graphene films as the transparent electrode in organic photovoltaic devices. *Thin Solid Films* **520,** 1238–1241 (2011).
258. Wu, H. *et al.* Electrospun metal nanofiber webs as high-performance transparent electrode. *Nano Lett.* **10,** 4242–4248 (2010).
259. Spinelli, P. & Polman, A. Transparent Conducting Silver Nanowire Networks. (2012).
260. Zou, J., Yip, H. L., Hau, S. K. & Jen, A. K. Y. Metal grid/conducting polymer hybrid transparent electrode for inverted polymer solar cells. *Appl. Phys. Lett.* **96,** (2010).
261. Bai, J., Zhong, X., Jiang, S., Huang, Y. & Duan, X. Graphene nanomesh. *Nat. Nanotechnol.* **5,** 190–194 (2010).
262. Mondai, P., Shah, S. R. & Marks, L. D. Nanoscale characterization of

cementitious materials. *ACI Mater. J.* **105,** 174–179 (2008).

263. Zeng, Z. *et al.* Fabrication of graphene nanomesh by using an anodic aluminum oxide membrane as a template. *Adv. Mater.* **24,** 4138–4142 (2012).
264. Al, W. E. T. In Situ Fabrication of Porous Graphene Electrodes for High-Performance. 2422–2430 (2013).
265. Zhu, Y. *et al.* Carbon-Based Supercapacitors. **332,** 1537–1542 (2011).
266. Zhang, Q. *et al.* Solution-processable graphene mesh transparent electrodes for organic solar cells. *Nano Res.* **6,** 478–484 (2013).
267. Yusoff, A. R. B. M., Lee, S. J., Shneider, F. K., Da Silva, W. J. & Jang, J. High-performance semitransparent tandem solar cell of 8.02% conversion efficiency with solution-processed graphene mesh and laminated Ag nanowire top electrodes. *Adv. Energy Mater.* **4,** 1–10 (2014).
268. Kumar, P., Subrahmanyam, K. S. & Rao, C. N. R. Graphene Patterning and Lithography Employing Laser/Electron-Beam Reduced Graphene Oxide and Hydrogenated Graphene. *Mater. Express* **1,** 252–256 (2011).
269. El-Kady, M. F. & Kaner, R. B. Scalable fabrication of high-power graphene micro-supercapacitors for flexible and on-chip energy storage. *Nat. Commun.* **4,** (2013).
270. Tian, H. *et al.* Cost-E ff ective, Transfer-Free, Flexible Resistive Random Access Memory Using Laser-Scribed Reduced Graphene Oxide Patterning Technology. (2014).
271. Vorobyev, A. Y. & Guo, C. Direct femtosecond laser surface nano/microstructuring and its applications. *Laser Photonics Rev.* **7,** 385–407 (2013).
272. Zentrum, L. & Hannover, D.-. Applied Phy esA=o"°°o ©. **115,** 109–115 (1996).
273. El-kady, M. F., Kaner, R. B., Angeles, L., States, U. & Science, M. Direct Laser Writing of Graphene. *ACS Nano* 0–4 (2014). doi:10.1021/nn504946k
274. Zhang, Y. L., Chen, Q. D., Xia, H. & Sun, H. B. Designable 3D nanofabrication by femtosecond laser direct writing. *Nano Today* **5,** 435–448 (2010).
275. Moon, I. K., Lee, J., Ruoff, R. S. & Lee, H. Reduced graphene oxide by chemical graphitization. *Nat. Commun.* **1,** (2010).
276. Das, S. *et al.* Effect of HNO3 functionalization on large scale graphene for

enhanced tri-iodide reduction in dye-sensitized solar cells. *J. Mater. Chem.* **22,** 20490 (2012).

277. He, Z. *et al.* Simultaneous enhancement of open-circuit voltage, short-circuit current density, and fill factor in polymer solar cells. *Adv. Mater.* **23,** 4636–4643 (2011).
278. Pang, S., Tsao, H. N., Feng, X. & Mullen, K. Patterned graphene electrodes from solution-processed graphite oxide films for organic field-effect transistors. *Adv. Mater.* **21,** 3488–3491 (2009).
279. Jiang, H. B. *et al.* Bioinspired fabrication of superhydrophobic graphene films by two-beam laser interference. *Adv. Funct. Mater.* **24,** 4595–4602 (2014).
280. Eaton, S. *et al.* Heat accumulation effects in femtosecond laser-written waveguides with variable repetition rate. *Opt. Express* **13,** 4708–4716 (2005).
281. Osellame, R. *et al.* Femtosecond writing of active optical waveguides with astigmatically shaped beams. *J. Opt. Soc. Am. B* **20,** 1559 (2003).
282. Li, Y.-C. *et al.* Graphene oxide-based micropatterns via high-throughput multiphoton-induced reduction and ablation. *Opt. Express* **22,** 19726 (2014).
283. Park, J. B. *et al.* Fast growth of graphene patterns by laser direct writing. *Appl. Phys. Lett.* **98,** 16–19 (2011).
284. Bie, Y. Q. *et al.* Site-specific transfer-printing of individual graphene microscale patterns to arbitrary surfaces. *Adv. Mater.* **23,** 3938–3943 (2011).
285. He, Q. *et al.* Micropatterns of Reduced Graphene Oxide Films : Fabrication and Sensing Applications. **4,** 3201–3208 (2010).
286. Stephan, O. *et al.* Doping Graphitic and Carbon Nanotube Structures with Boron and Nitrogen. *Science (80-.).* **266,** 1683–1685 (1994).
287. Schuffenhauer, C. *et al.* Synthesis of Fullerene-Like Tantalum Disulfide Nanoparticles by a Gas-Phase Reaction and Laser Ablation. *Small* **1,** 1100–1109 (2005).
288. Rosenfeld Hacohen, Y., Popovitz-Biro, R., Grunbaum, E., Prior, Y. & Tenne, R. Vapor–Liquid–Solid (VLS) Growth of NiCl2 Nanotubes via Reactive Gas Laser Ablation. *Adv. Mater.* **14,** 1075 (2002).
289. Panchakarla, L. S. *et al.* Nanotubes from Misfit Layered Compounds: A New Family of Materials with Low Dimensionality. *J. Phys. Chem. Lett.* **5,** 3724–3736 (2014).
290. G. Seifert, *,†, T. Köhler, † and & Tenne‡, R. Stability of Metal Chalcogenide

Nanotubes. (2002). doi:10.1021/JP0131323

291. Tenne, R., Rosentsveig, R. & Zak, A. Inorganic nanotubes and fullerene-like nanoparticles: Synthesis, mechanical properties, and applications. *Phys. status solidi* **210,** 2253–2258 (2013).
292. Rapoport, L., Fleischer, N. & Tenne, R. Applications of WS2(MoS2) inorganic nanotubes and fullerene-like nanoparticles for solid lubrication and for structural nanocomposites. *J. Mater. Chem.* **15,** 1782 (2005).
293. Naffakh, M., Díez-Pascual, A. M., Marco, C., Ellis, G. J. & Gómez-Fatou, M. A. Opportunities and challenges in the use of inorganic fullerene-like nanoparticles to produce advanced polymer nanocomposites. *Prog. Polym. Sci.* **38,** 1163–1231 (2013).
294. Viskadouros, G. *et al.* Enhanced Field Emission of WS_2 Nanotubes. *Small* **10,** 2398–2403 (2014).
295. Chhetri, M. *et al.* Beneficial effect of Re doping on the electrochemical HER activity of MoS_2 fullerenes. *Dalt. Trans.* **44,** 16399–16404 (2015).
296. Woo, S. H. *et al.* Fullerene-like Re-Doped MoS_2 Nanoparticles as an Intercalation Host with Fast Kinetics for Sodium Ion Batteries. *Isr. J. Chem.* **55,** 599–603 (2015).
297. Appel, J. H. *et al.* Low Cytotoxicity and Genotoxicity of Two-Dimensional MoS_2 and WS_2. *ACS Biomater. Sci. Eng.* **2,** 361–367 (2016).
298. Pardo, M., Shuster-Meiseles, T., Levin-Zaidman, S., Rudich, A. & Rudich, Y. Low Cytotoxicity of Inorganic Nanotubes and Fullerene-Like Nanostructures in Human Bronchial Epithelial Cells: Relation to Inflammatory Gene Induction and Antioxidant Response. *Environ. Sci. Technol.* **48,** 3457–3466 (2014).
299. Rashkow, J. T., Talukdar, Y., Lalwani, G. & Sitharaman, B. Interactions of 1D- and 2D-layered inorganic nanoparticles with fibroblasts and human mesenchymal stem cells. *Nanomedicine* **10,** 1693–1706 (2015).
300. Goldman, E. B. *et al.* Biocompatibility of Tungsten Disulfide Inorganic Nanotubes and Fullerene-Like Nanoparticles with Salivary Gland Cells. *Tissue Eng. Part A* **21,** 1013–1023 (2015).
301. A. Rothschild, †, J. Sloan, ‡ and & R. Tenne*, †. Growth of WS2 Nanotubes Phases. (2000). doi:10.1021/JA994118V
302. Yan Qiu Zhu *et al.* Production of WS2 Nanotubes. (2000). doi:10.1021/CM991189K

303. Remškar, M., Viršek, M. & Mrzel, A. The MoS2 nanotube hybrids. *Appl. Phys. Lett.* **95,** 133122 (2009).
304. Kroto, H., Wasserman, E., Srolovitz, D. J. & Tenne, R. Space, Stars, C60, and Soot. *Science (80-.).* **242,** 1139–1145 (1988).
305. A. Zak, Y. Feldman, V. Alperovich, R. Rosentsveig, and & Tenne*, R. Growth Mechanism of MoS2 Fullerene-like Nanoparticles by Gas-Phase Synthesis. (2000). doi:10.1021/JA002181A
306. Albu-Yaron, A. *et al.* MoS2 Hybrid Nanostructures: From Octahedral to Quasi-Spherical Shells within Individual Nanoparticles. *Angew. Chemie Int. Ed.* **50,** 1810–1814 (2011).
307. Alexandrou, I. *et al.* Structural investigation of MoS $_2$ core–shell nanoparticles formed by an arc discharge in water. *Nanotechnology* **14,** 913–917 (2003).
308. Chhowalla, M. & Amaratunga, G. A. J. Thin films of fullerene-like MoS_2 nanoparticles with ultra-lowfriction and wear. *Nature* **407,** 164–167 (2000).
309. Brontvein, O., Jayaram, V., Reddy, K. P. J., Gordon, J. M. & Tenne, R. Two-step Synthesis of MoS $_2$ Nanotubes using Shock Waves with Lead as Growth Promoter. *Zeitschrift für Anorg. und Allg. Chemie* **640,** 1152–1158 (2014).
310. Yan Qiu Zhu, † *et al.* Shock-Wave Resistance of WS2 Nanotubes. (2003). doi:10.1021/JA021208I
311. Brontvein, O. *et al.* Synthesis and Characterization of Pb@GaS Core–Shell Fullerene-Like Nanoparticles and Nanotubes. *Nano* **12,** 1750030 (2017).
312. Sygletou, M., Petridis, C., Kymakis, E. & Stratakis, E. Advanced Photonic Processes for Photovoltaic and Energy Storage Systems. *Adv. Mater.* **29,** 1700335 (2017).